Lawrence Berkeley National Laboratory

Title
STUDIES ON HIGH SPEED ELECTROFORMING

Permalink
https://escholarship.org/uc/item/0t41v8x9

Author
Barkey, D.P.

Publication Date
1987-08-01

Lawrence Berkeley Laboratory

UNIVERSITY OF CALIFORNIA

Materials & Chemical Sciences Division

Studies on High Speed Electroforming

D.P. Barkey
(Ph.D. Thesis)

August 1987

DISCLAIMER

Studies on High-Speed Electroforming

Dale Paul Barkey

Lawrence Berkeley Laboratory
University of California
and
Department of Chemical Engineering
University of California, Berkeley
Berkeley, California 94720

August 1987

Studies on High-Speed Electroforming

Dale Paul Barkey

Department of Chemical Engineering
and Lawrence Berkeley Laboratory
University of California, Berkeley

Abstract

Studies on high-speed electroforming were undertaken to evaluate the potential for electroforming at rates comparable to those of mechanical forming. A rotating cylindrical cathode was used to provide intense turbulent convective transport. Transport in the cylindrical cell equipped with radial baffles was characterized by direct measurement of limiting currents of high rate copper deposition. Copper electroforms of thicknesses of several hundred micrometers were produced by deposition at rates of up to 7.5 A/cm^2 corresponding to 160μm per minute.

A quantitative theory of morphological stability, accounting for transport, kinetic and ohmic effects, was formulated for copper deposition at high rates. Surfaces of deposits produced in the electroforming experiments were charaterized by surface profilometry, and digitallized profiles were analyzed by Fourier transform for comparison with predictions of the stability theory. Decrease in roughness protrusion spacing with both increasing current density and increasing fraction of limiting current is correctly predicted. Differences between expected and observed roughness characteristics are attributed to constraints on

protrusion size and spacing imposed by nucleation of growths sites.

The Fourier transform technique was also used to compare the growth of features inside and outside the hydrodynamic boundary layer. In agreement with a mechanism previously proposed by Ibl, the two regimes showed different dependences on conditions of deposition.

Acknowledgements

I am grateful for the guidance and example provided by Professor Charles Tobias and Dr. Rolf Muller, and for their willingness to share their time and knowledge. The atmosphere of intellectual effort that they have created here has had a profound influence on me.

I would like to thank all of the members of the research group for the encouragement and stimulation I received from them. In particular I want to thank Gina Whitney and John Dukovic for their help in formulating the ideas presented in this thesis and Rick Gyory for his invaluable contributions in producing the thesis.

I also wish to thank Hank Brendel, Lee Johnson, Erlene Fong, Herb Riebe and Jim Severns for everything they taught me and for their contributions to my work.

I want to thank Deborah Sisson for sharing my life through both the happiest and the most difficult times. I am grateful for the opportunity to have studied and lived in Berkeley. I cannot name all of the influences I found here, but I want to mention the members of FacHRES and of course Tom.

Contents

List of Figures

List of Tables

Chapter 1. Introduction

1.1. Purpose

The theoretical and experimental studies reported here were undertaken to assess the potential for electroforming at rates comparable to rates of forming metallic shapes by mechanical means. Electroforming, a process technology for the production of metal objects by electrolytic deposition, is slow because the rate of deposition is limited by the rate at which metal ions can reach the surface. Even below this limiting current, excessive surface roughness usually develops as the mass-transfer limited rate is approached. In these studies, the variation of deposit characteristics with conditions of deposition at high rates was examined with particular emphasis on the development of surface texture. A quantitative analysis of the dependence of surface texture development on deposition conditions was carried out to evaluate the potential for electroforming at accelerated rates.

1.2. Structure of Thesis

In chapter one, a brief survey of electroforming practice is presented. The limitations to the rate of electroforming are considered, and previous attempts to accelerate electrodeposition are reviewed.

The theory of surface texture development during copper electrodeposition is treated in chapter two. Previous experimental and theoretical studies are summarized. Recent attempts to formulate a morphological stability theory

applicable to metal electrodeposition are reviewed, and an extended theory is presented. The validity of the theory for deposition processes involving nucleation and flow phenomena is examined.

The high-speed electroforming apparatus and the instruments used in quantitatively evaluating the electroforms are described in chapter three. The materials and procedures used in the limiting current and deposition experiments are reported.

Chapter four is concerned with the measurement of mass transfer limited currents of metal deposition on a cylindrical rotating electrode (RCE) in a cell equipped with radial baffles. A study of limiting currents was undertaken to characterize the RCE cell used in the deposition studies. The literature on the RCE is reviewed, and a discussion of the particular problems encountered in the measurement of limiting currents of metal deposition at high rates is given. The results for deposition over a range of conditions and for several cell geometries are correlated.

In chapter five, the high speed electroforming experiments are described, and the results are interpreted in terms of the theory presented in chapter two.

1.3. Survey of Electroforming Practice

Electroforming is a process technology for the production of metal objects by electrolytic deposition. The metal deposit forms a negative replica of the cathode, which acts as a mold. Manufacture of complex shapes at ambient tem-

peratures with high fidelity of surface shape and texture reproduction make electroforming an attractive alternative to mechanical or melt forming for a range of special applications. However, low rates of deposition imposed by mass-transfer limitations have prevented its wider use.

Comprehensive reviews of electroforming were published by Safranek in 1964 (1) and by Spiro in 1972 (2). In 1980, Kaznachi published an extensive review on the manufacture of small tools and pieces by electroforming (3). Brief reviews have been published by Weiler (4), Squitero (5) and DiBari (6).

The metal most widely used for electroforming is Nickel (7,8). Applications include molds and dies (9,10,11), foundry patterns (12), and tools (13). Recent developments in electrolyte composition have improved the speed and quaility of nickel electroforming (14). The need for strength, particularly for molds to be used at high temperature, has led to the development of nickel alloy plating baths containing cobalt (15,16) or manganese (17,18). Bulk glassy metal alloys have been electroformed by codeposition of nickel and phosphoruus (19).

Copper is also widely used for electroforming, particularly for electronic applications that do not require strength. The commercial manufacture of printed circuits (20), tube circuits (21) and flexible circuits (22) are examples. The highest rates of commercial electroforming, with current densities of about two amperes per square centimeter, are reported for flexible circuits (23). Copper electroforming onto molds prepared by microlithography has been applied in the production of electronic components (24,25,26,27). Electroforming of extremely smooth substrates for electronic device fabrication by

deposition of copper on glass has been proposed (28). Copper electroforms are also used in printing (29).

Gold is electroformed for both decorative and industrial applications (30). The former include jewelry, artwork, medallions and plaques. Among the latter are grids and aperture diaphragms for electron microscopy. Both pure gold (31) and alloys (32,33) are formed. Silver is also electroformed (34).

Reviews of electroforming of iron have been published by Harty, McGeough and Tulloch (35) and by Lai and McGeough (36). The latter proposed electroforming iron and iron-nickel foil. An examination of the prospects for electroforming iron sheet was given by Silman (37), and an experimental study of high-speed electroforming of iron foil was reported by Subramanian and King (38). High speed electroforming would be particularly attractive for the manufacture of foils because this geometry permits the use of channel flow to enhance convective mass transfer. The advantage of electroforming in comparison with rolling is greatest for thin foils.

Metals from which experimental electroforms have been produced include aluminum (39,40), lead (41), platinum metals (42), alloys of cobalt with nickel and tungsten (43) and refractory metals (44).

Several types of composite materials have also been electroformed. Deposition of a nickel matrix onto fibers of tungsten, boron and boron nitride coated boron filaments results in a high-strength reinforced composite (45). Copper, nickel and aluminum matrices have been formed on tungsten, boron and silicon

reinforcers (46). Electroforms containing cubic boron nitride (47) and diamond (48) have found commercial application as abrasives. Laminated foils of alternating copper and nickel layers have been studied for possible electronic applications. (49).

Electroforming is typically applied in cases where an object cannot be formed by other means because of geometric, temperature or surface finish constraints. An example is the manufacture of waveguides, where an enclosed channel of rectangular cross section must be formed to close dimensional tolerance, often with a bent path (50,51,52). Rotogravure cylinders, which eject ink through a pattern of fine holes, are electroformed in copper or nickel (53). Hollow articles containing reentrant angles can be electroformed using molds that are collapsible or removable by melting or dissolution (54,55). Examples of hollow electroformed articles are pressure vessels and hollow core screens (56). Fine-mesh screens for batteries are commonly electroformed (57,58).

A variety of objects containing integral channels are produced by plating over grooves filled with a material that is then removed by dissolution or melting (59,60,61,62). Objects formed in this manner include combustion chambers, solar concentrators, water cooled components for nuclear power, wind tunnel models, waveguides and erosion protection shapes. A number of applications exist in the aerospace industries (63,64).

Among the oldest applications of electroforming is the manufacture of printing and embossing plates, where the accurate reproduction of surface texture is critical. The ability to reproduce surface detail on a sub-micrometer

scale has made electroforming the standard method for manufacturing stampers for phonograph records and videodisks (65,66,67,68) Accurate reproduction of smooth surfaces permits the manufacture of optical components (69,70). The difficult process of machining a non-spherical mirror need be carried out only once. Hundreds of mirrors can then be produced from a single master by electroforming. This type of precision electroforming is also used for the manufacture of dental base plates, linings, retaining points and ridges (71).

The range of applications is illustrated by a few unusual examples. 80 angstrom diameter wires were electroformed in gold (72). A micrometer scale of 50 micrometers overall length was electroformed in nickel (73). At the other extreme of size scale, seamless crucibles of 10 meter length and 3 meter diameter were electroformed in copper (74).

In the century and a half of electroforming practice, a wide variety of successful industrial applications have arisen. They are limited, however, to relatively small scales of production. Accelarated rates of electroforming would improve the efficiency of existing processes and could lead to entirely new large-scale technologies.

1.4 Limitations on the Rate of Deposition

Current densities in practical copper electroforming processes rarely exceed 80 milliamperes per square centimeter, corresponding to a deposit growth rate of two micrometers per minute. A consequence of low rates imposed by mass-transfer limitations is that electroforming can be justified only if no other

fabrication technique is possible for a given application. Any kinetic limitation is far beyond the mass-transfer limited rate. Copper, for example, has been deposited at up to 250 amperes per square centimeter during short pulses which do not deplete the diffusion boundary layer (75). High rates of deposition during pulsed laser heating of the substrate have also been demonstrated (76). For electroforming applications, high rate deposition is useful only if it can be sustained long enough to produce a thick deposit. This steady-state, sustainable rate is limited by mass transfer.

It is well known that deposition near the mass transfer limited current results in rough deposits of no value for electroforming. This roughness development was attributed by Ibl to the instability of the deposit surface under diffusion limiting conditions (77). Attempts by many investigators to accelerate metal deposition have focused on mass transfer enhancement.

Roha reviewed the literature on methods for increasing deposition rates by disrupting or thinning the mass transfer boudary layer (78). He reported six ˙methods: Spray jets, high-speed channel flow, mechanical wiping, sonic and ultrasonic vibration, electromagnetic stirring and agitation by a dispersed phase. The highest rates have been reported for high-speed channel flow and mechanical wiping. Roha's experimental studies showed that the limiting current to a rotating disk can also be multiplied several fold by addition of a dense suspension of inert particles.

Hart has reviewed high speed plating with an emphasis on applications (79,80). A more comprehensive review of commercial high-speed metal

deposition is that of Safranek (81). Electroforming applications include flexible copper circuitry (23) and nickel printing plates (82). In the latter application, the current densities reported are less than one ampere per square centimeter. The copper circuits are formed at up to two amperes per square centimeter, or 50 micrometers per minute. Pilot scale channel and moving belt cells have been used to plate iron-zinc alloys at up to 2.5 A/cm^2 (83) and zinc at up to 3.5 A/cm^2 at 90% current eficiency (84). Gold is commercially electroplated at rates of up to 0.8 A/cm^2 (85). However, because plating requires only a thin deposit, a higher rate of roughness development, and hence a closer approach to the limiting current, can be tolerated in plating than in forming processes.

Safrenek studied high-speed metal deposition for a number of metals (86). He reported the electroforming of coherent copper foils, 50 micrometers thick, at current densities of up to 3.1 A/cm^2. Safrenek used high-speed channel flow, but did not attempt a rigorous analysis of the transport conditions in his cell. He maintained that a flow velocity, or velocity of cathode movement, of one to two meters per second is sufficient to produce electroforms at high rates, regardless of cell geometry. Chin deposited chromium at up to 70 A/cm^2 using high-speed channel flow (87). When consideration is made for the reported current efficiency and the valence of the chromium ion, this corresponds to a rate of deposition comparable to Safrenek's. A review of the use of high-speed channel flow for metal deposition with some consideration of mass transfer was presented by El-Shazly, White and Brooman (88).

The highest rate of coherent copper deposition appears to have been acheived by Eisen using mechanical wiping of the deposit with an abrasive sheet (89,90). He reported a deposit growth rate for copper of 125 micrometers per minute, corresponding to deposition at five amperes per square centimeter. A commercial plating machine operating on the same principle has been used to plate copper at about half this rate (92). An example of electroforming with agitation by a dispersed phase was reported by Thangepan and coworkers (91). Copper waveguides were electroformed in an inert fluidized bed at up to 100 amperes per square centimeter. The fluidized suspension produced a doubling of the limiting current density.

The most systematic and rigorous study of high rate copper deposition is that of Degrez and Winand (93). Limiting currents in a high speed flow channel were measured and found to be in agreement with a previous correlation. Copper deposition studies were then conducted with control of the mass transfer conditions. A roughening of deposits at high rates was attributed to the onset of 3-D nucleation. The term apparently refers to the appearance of surface protrusions, and no definition in terms of crystallization phenomena is given. The onset of 3-D nucleation was correlated with a dimensionless current density variable, which for the range of conditions reported is simply a measure of the combined kinetic and concentration overpotential. Correlation of roughness with this parameter is questionable since the concentration and kinetic overpotentials are measures of quite different phenomena with different and sometimes opposing influences on current distribution.

The literature on high-speed metal electrodeposition indicates that a substantial improvement in practical rates can be acheived through the use of turbulent convective transport. Most studies to date, however, have not examined in a systematic way the factors influencing the deposit quality as rates are increased. While previous investigations have demonstrated the potential for high-speed deposition, they do not provide a basis for the sound design of high-speed deposition processes.

Chapter 2. Development of Deposit Surface Texture

2.1. Introduction

Electrodeposition of metals to thicknesses suitible for electroforming inevitably results in roughening of the deposit surface. Since practical electrodeposits are polycrystalline, it is to be expected that surface texture should develop as the crystal faces grow at different rates, or individual crystallites are initiated at sites distributed on the surface. This crystallographic texture is amplified during deposition, resulting in macroscopic surface roughness. Surface roughness is a waste of material and in extreme cases leads to porous or noncoherent deposits. It arises because the process of electrodeposition is unstable to the development of protrusions that grow more rapidly than the surrounding surface.

The distribution of current density on an ideally smooth electrode is uniform for certain cases, for example a cylindrical cathode with a concentric cylindrical anode. For most shapes, the local current density varies from point to point on the cathode. If this variation is gradual, a smooth deposit of variable thickness is formed. The variation of current distribution on this scale is referred to as the current macrodistribution. More extreme and random variation of the current density over short distances, the current microdistribution, produces roughness (see figure 2-1). For a uniform current microdistribution, the gradients of potential and concentration do not vary over short distances. If, however, the surface is not ideally smooth, but contains protrusions, both the
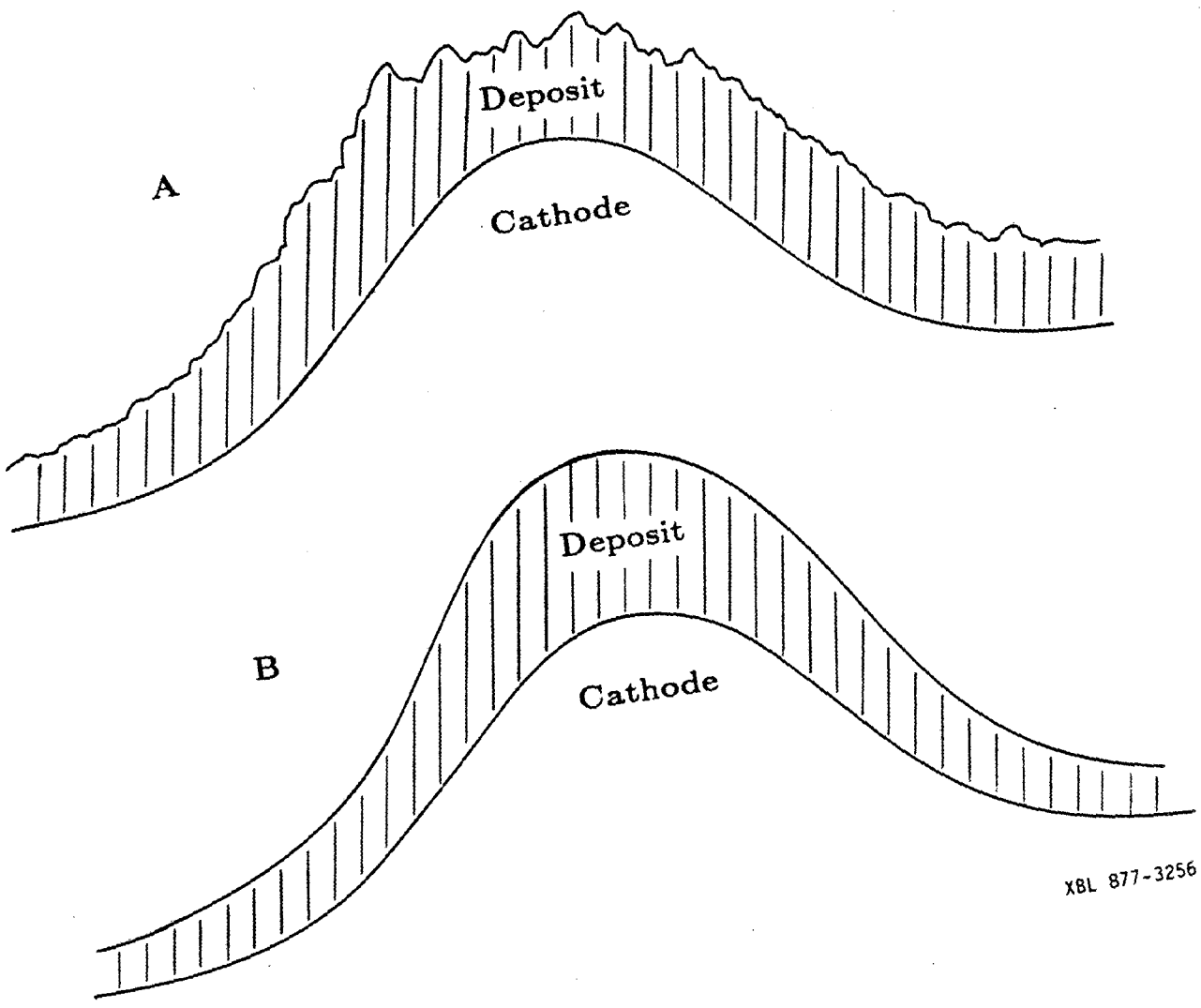
Figure 2-1: Current Micro and Macro Distribution. A) Non-uniform current microdistribution, B) non-uniform current macrodistribution.

potential and concentration fields promote preferential deposition at the protrusions. The resulting non-uniform distribution of current favors their amplification. Reviews of current distribution on rough surfaces have been presented by Kardos and Foulke (94) and by de Levie (95).

Instability of the surface to perturbations in shape is most extreme for the cases of primary current distribution and diffusion controlled current distribution. The mechanism of diffusion controlled deposition of metal powders has been treated by Ibl (77) and by Ibl, Javet and Stahel (96). At the limiting current, the surface concentration is everywhere zero, and the current distribution is controlled by transport of metal ion in the electrolyte. Mass transport favors peaks of the surface, and any protrusions that arise are rapidly amplified.

Practical electroforming is carried out in a regime where the ohmic, transport and kinetic overpotentials must all be taken into account. In this discussion, the influences of these factors are examined for the case of an idealized surface of sinusoidal roughness. The sinusoidal profile was chosen to simplify the analysis of current distribution on a rough surface. The current distribution on a sinusoidal electrode has been treated analytically by Wagner (97) and Fedkiw (98). The sinusoidal electrode has been employed in numerical simulations by Prentice and Tobias, and the calculated profiles were confirmed by experimental determination of current distribution in copper deposition (99). Current distribution to a sinusoidal electrode has also been applied in the perturbation analysis of electrode shape stability by McGeough and Rasmussen (100-102), Aogaki et al. (103-107) and Landau (108).

The discussion that follows is in four sections. Previous theoretical treatments of roughness development are surveyed. The current density distribution at sinusoidal electrodes under various conditions of deposition is then analyzed as an idealized simulation of surface roughness development. In the third section, previous formulations of the stability problem for metal electrodeposition are reviewed, and an extended formulation is presented. Consideration is then given to the form of surface perturbatons that can be expected to arise during metal deposition.

2.2. Morphology of Metal Electrodeposits

Kindler has extensively reviewed the literature on copper electrodeposit morphology. (109). His review dealt with both crystallographic and mass transfer influences. It has been demonstrated that at current densities well below the limiting current density, copper deposit morphology is strongly affected by crystallographic factors. At low current densities, deposits grow by addition of layers to growing crystallites (110). The morphology (111) and exchange current density (112) of copper deposition on single crystals depend on the crystal face, which suggests that deposit morphology is influenced by the kinetics of crystallization. Crystallization phenomena in high-rate deposition are considered in section 2-4.

Many early studies of deposit morphology were invalid due to failure to control and/or report the conditions of mass transfer. It is now accepted that mass transfer controlled deposition is the cause of a wide class of dendritic and

powdery deposit morphologies.

Barton and Bockris formulated a theory of dendritic growth based on diffusion controlled deposition (113). The theory accounts for dendritic growth by a mechanism of spherical diffusion to the dendrite tip. Spherical diffusion conditions, which arise when a protrusion penetrates the diffusion layer, result in a high current density at the tip (see figure 2-2). The activity of the metal, and hence the deposition potential, is higher for a curved surface than for a flat one, an effect referred to below as capillarity. The competing influences of capillarity and mass transport result in an optimal tip radius, with a maximum in the growth rate. Hamilton showed that under this dendritic growth condition a parabolic tip retains its shape (114). Diggle, Despic and Bockris extended the theory to the Tafel region (115).

According to this model a protrusion on the surface grows at a rate inversely proportional to the distance of the protrusion tip from the edge of the diffusion boundary layer. During this period of surface amplification, the current density at the tip increases exponentially with time. When the current density reaches a magnitude equal to that at a dendrite tip spherical diffusion conditions set in, and dendritic growth begins. During dendritic growth, the protrusion advances at a constant rate given by the Barton-Bockris theory. Oren and Landau found dendritic growth of zinc to be consistent with this model (116).

Popov and coworkers have published several papers on the Barton-Bockris model and have applied it to copper deposition at the limiting current (117-

δ
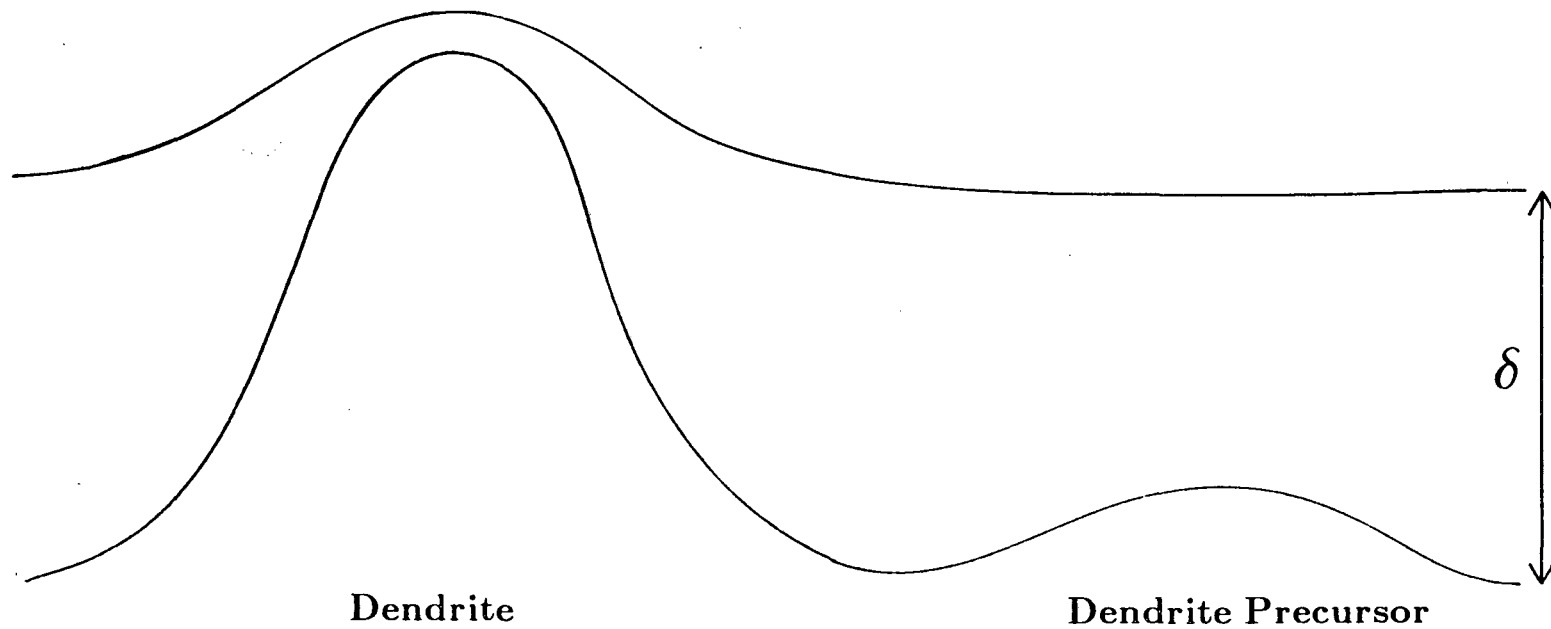
Dendrite

Dendrite Precursor

Figure 2-2: Dendrite growing under spherical diffusion conditions and dendrite precurser growing by surface amplification in a mass transfer boundary layer of thickness δ.

120). They sought to confirm the model by measuring the induction time for dendritic growth and the critical overpotential for instantaneous initiation of dendrites. They claimed agreement with theory for dendritic growth of copper, but the result is questionable because the mass transfer conditions for their apparatus were not well reported.

Landau has pointed out the deficiencies in the Barton-Bockris model (108). The induction time is found by extrapolation of the dendritic growth rate back to initiation, a stage of growth for which the model is not appropriate. The critical overpotential is defined in terms of this induction time. There are problems in extending the model to treat surface roughness generally. This type of analysis treats individual dendrites and protrusions in isolation fron the surrounding surface and from other protrusions. It gives information on dendrite tip radii but not on dendrite or protrusion spacing. In addition, the shape preserving parabolic tip is not necessarily stable to branching or roughening (121). The determination of protrusion spacing, and of surface texture generally, at various fractions of the limiting current density requires a stability analysis of the deposit growth front.

2.3 Current Distribution at Sinusoidal Electrodes

A non-uniform current microdistribution results in the development of surface roughness. A theoretical examination of deposition on sinusoidal profiles of various amplitudes and spatial periods illustrates the influence of deposition conditions on roughness development. Analytical, numerical and experimental

treatments of the sinusoidal electrode are available in the literature. The application of these results to roughness development requires a correct accounting of the effects of scale. These effects are discussed here as they depend on the relevant dimensionless parameters.

The primary current distribution on low amplitude sinusoidal profiles has been treated by Wagner (97) and by Fedkiw (98). Wagner found a particular solution for the primary current distribution. In the limit of small ratio of amplitude to spatial period, the solution for the potential matches the boundary condition of uniform potential at the electrode surface. The surface profile is described by

$$z_s = A\sin(\omega x) \tag{2-1}$$

where z_s is the surface height, x the position on the surface, A the amplitude of the sinusoid and ω its spatial frequency. Wagner's solution is

$$\frac{i - i_A}{i_A} = \omega A\sin(\omega x) \tag{2-2}$$

where i is the current density and i_A is the average current density. This current distribution is illustrated in figure 2-3.

The spatial frequency, ω, is related to the spatial period or wavelength, λ, by

$$\lambda = \frac{2\pi}{\omega} \tag{2-3}$$

The aspect ratio, A/λ, is a measure of the sharpness of the profile.

Deposit

Cathode

$z_s = A\sin(\omega x)$

z_s

z

X
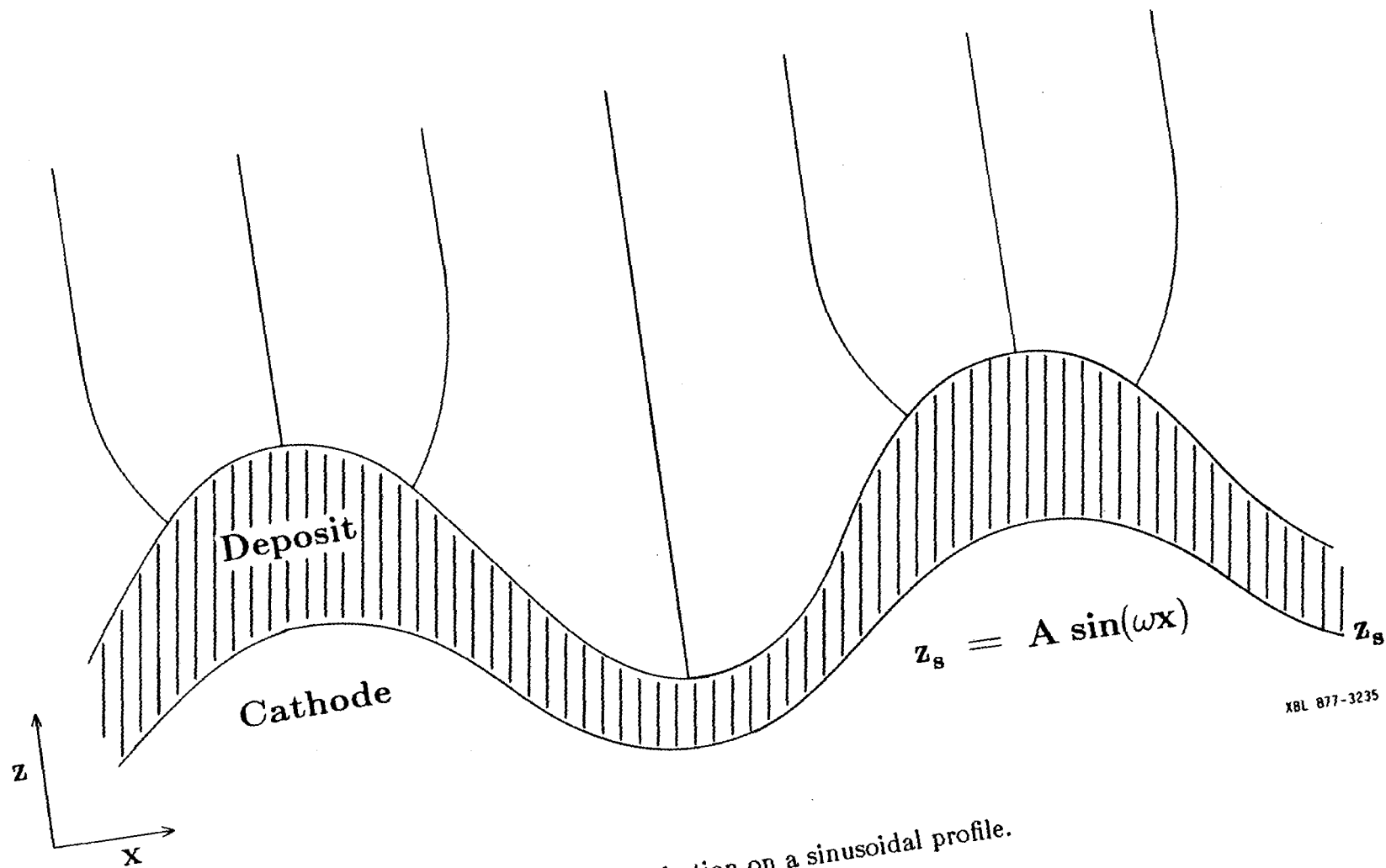
Figure 2-3: Current distribution on a sinusoidal profile.

XBL 877-3235

The current distribution given by equation 2-2 results in a rate of growth of the amplitude

$$\frac{\partial \ln A}{\partial t} = \frac{\nu}{nF}\omega \qquad (2\text{-}4)$$

where ν is the molar volume, n the ion charge and F the Faraday constant. The solution also applies to mass-transfer controlled deposition when the concentration falls to zero everywhere on the electrode surface. Fedkiw found a series solution, valid for any aspect ratio, which reduces to Wagner's equation in the limit of small amplitude.

The amplitude growth rate determined by Fedkiw is proportional to a power series in the aspect ratio. The rate of increase of the profile amplitude is inversely proportional to the profile spatial period. The rate of shape change, or rate of change in the aspect ratio, is therefore inversely proportional to the square of the spatial period. Evidently, the scale of a profile influences its rate of shape change even for the primary current distibution.

This result is relevant to geometric levelling. If the current density is uniform over a surface containing protrusions, the amplitude of neighboring protrusions is reduced as they grow into one another (figure 2-4), a consequence of the fact that the current density normal to an inclined surface has a horizontal component. the rate of geometric levelling depends on the scale of features being levelled, both because small features are more uniformly plated and because a given deposition rate erases smaller features faster.
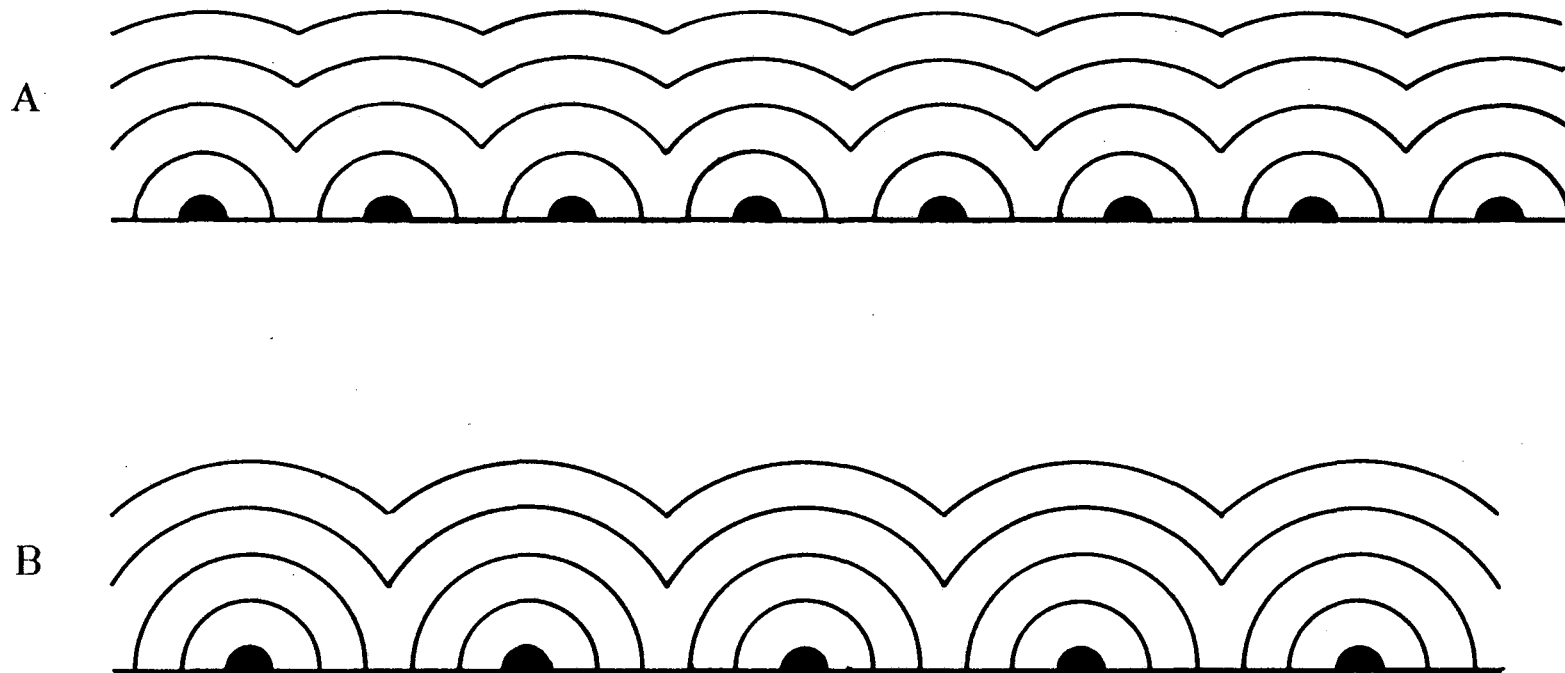
Figure 2-4: Geometric levelling. The hemispherical protrusions grow into one another resulting in a reduction of profile amplitude. Amplitude of closely spaced features (A) is reduced more rapidly than that of widely spaced features (B).

Both Wagner and Fedkiw point out that the solution can only be applied to mass-transfer controlled deposition if the amplitude and spatial period of the surface are small in comparison with the mass transfer boundary layer thickness. For longer spatial periods, the mass transfer boundary layer follows the profile, and mass-transfer resistance is evenly distributed. This simple model therefore predicts that the form of roughness induced by mass transfer resistance should be the same as that induced by the primary current distribution for closely spaced protrusions or roughness of small spatial period. On a scale larger than the mass transfer boundary layer thickness, mass transfer resistance should not produce roughness.

Practical electroforming is carried out under conditions of mixed ohmic, kinetic and mass-transport control. Effects of scale can be estimated with dimensionless parameters that characterize the relative importance of these influences. Three cases are considered below. They are primary current distribution modified by kinetic overpotential, primary current distribution modified by concentration overpotential and diffusion controlled deposition modified by kinetic overpotential.

Non-uniformity of the primary current distribution is reduced by kinetic overpotential, provided the kinetic polarization curve has a positive slope. The departure from the primary distribution is characterized by the Wagner number, Wa.

$$Wa = \frac{\dfrac{\partial \eta_a}{\partial i}}{\dfrac{\partial \eta_r}{\partial i}} \qquad (2\text{-}5)$$

where η_a is the kinetic overpotential and η_r the ohmic overpotential. A large Wagner number indicates a uniform current distribution. The Wagner number contains a characteristic length, which for this discussion could be either the amplitude or the spatial period of the sinusoid. The Wagner number for Tafel kinetics is

$$Wa = \frac{RT\,\kappa}{i\,L\,nF\,\alpha} \qquad (2\text{-}6)$$

where R is the gas constant, T the temperature, alpha the charge transfer coefficient, κ the electrolyte conductivity and L a characteristic length. Uniform current distribution is indicated by a Wagner number greater than about ten which occurs for values of L smaller than a reference length, L_r.

$$L_r = \frac{RT\,\kappa}{10\,i\,L\,nF\,\alpha} \qquad (2\text{-}7)$$

For copper deposition from a 1.0 M $CuSO_4$/ 1.0 M H_2SO_4 solution at 50° C at the high rate of one ampere per square centimeter, α is equal to 0.25, κ is 0.37 reciprocal ohm per centimeter and L_r is about 100 micrometers. Since an increase in current density reduces the Wagner number, it is expected that the current distribution should become more non-uniform with increasing current density. The non-uniformity should also extend to features of smaller scale as the current density is increased. For copper deposition at several amperes per

square centimeter, the distribution of current should become non-uniform for features of a few micrometers, the scale usually associated with mass-transfer induced roughening.

The primary current distribution may also be modified by the concenration overpotential. Prentice and Tobias carried out numerical simulations, confirmed by experiment, of current distribution for copper deposition which accounted for the effect of concentration overpotential on the primary current distribution (99). It was assumed that the concentration gradient was confined to a thin, uniform layer at the cathode. The current distribution was determined by dividing the electrolyte into two regions: the bulk, where the ohmic resistance predominates, and the concentration boundary layer. First, a solution of the primary current distribution was found. The local concentration overpotential was then determined from the current density and the two potentials were matched by iteration.

A dimensionless parameter, analogous to the Wagner number, was defined by Prentice and Tobias.

$$\mathrm{Wc} = \frac{\dfrac{\partial \eta_c}{\partial i}}{\dfrac{\partial \eta_r}{\partial i}} \tag{2-8}$$

$$\mathrm{Wc} = \frac{\mathrm{RT}\,\kappa}{\mathrm{nF}\,\mathrm{L}\,i_L\left(1 - \dfrac{i}{i_L}\right)} \tag{2-9}$$

where η_c is the concentration overpotential. A large value of this parameter,

which occurs near the limiting current, indicates a uniform current distribution over features larger than the mass transfer boundary layer thickness.

If the concentration overpotential is much larger than the ohmic drop in the mass transfer boundary layer, the current microdistribution is controlled by mass transfer and discharge kinetics. The tendency for the kinetic overpotential to smooth out the mass-transfer controlled current disribution can be estimated by another variant of the Wagner number.

$$\mathrm{Wd} \;=\; \frac{\dfrac{\partial \eta_a}{\partial i}}{\dfrac{\partial \eta_c}{\partial i}} \tag{2-10}$$

For Tafel kinetics and a well supported electrolyte, equation 2-10 takes the form,

$$\mathrm{Wd} \;=\; \frac{(1 - \dfrac{i}{i_L})}{\alpha \dfrac{i}{i_L}} \tag{2-11}$$

A fraction of limiting current above which deposition is non-uniform can be estimated by setting Wd equal to 10. For copper deposition from a sulfate electrolyte this fraction is about fifteen percent.

The total overpotential is constant over short distances if ohmic effects are not important. The current density, and hence the kinetic overpotential, can be raised at a given point on the surface only if the concentration overpotential is lowered there. This happens at points favored by mass transport. Since the

slope of the concentration overpotential versus current density curve increases rapidly near the limiting current, small redistributions in current in this regime require large changes in concentration overpotential. In this situation, mass transport is controlling. A steep kinetic overpotential versus current density curve, reflected in a large value of Wd, counteracts the tendency to mass transfer control.

The above discusion of current distribution on sinusoidal profiles suggests the following expectations for roughness development in metal deposition.

1) An increase in current density, at constant fraction of limiting current, should result in a less uniform current distribution. The spatial period of this non-uniformity has a lower limit indicated by the Wagner number. At conventional current densities, this lower limit is too high for the distribution to produce roughening. For copper deposition at rates greater than one ampere per square centimeter, the non-uniformity extends to spatial periods smaller than 100 micrometers, a scale associated with surface roughness. Deposition at current densities above this rate should therefore produce roughening even if the fraction of limiting current is kept low.

2) Approach to limiting current should smooth out the current distribution over features larger than the mass transfer boundary layer thickness, provided the geometry permits the mass transfer boundary layer to follow the surface contour.

3) Approach to the limiting current should produce a non-uniform current

distribution on features of spatial period smaller than the mass transfer boundary layer thickness. The degree of non-uniformity, or rate of roughening, should increase with increasing fraction of limiting current but be independent of absolute current density. Since roughening by mass-transport control does not have a lower size limit, the spatial period of mass transport induced roughness should be smaller than that of ohmic induced roughness.

2.4 Stability Theory

Several theories of morphological stability for metal electrodeposition have been advanced. In general the procedure begins with steady state deposition to some regular surface. A perturbation is imposed on the surface shape, and the growth rate of the perturbation is derived from the equations governing the current distribution. A positive growth rate indicates instability. The perturbation takes the form of a harmonic function of position on the surface. For perturbations of infinitesimal height, the behavior of an arbitrary shape can be determined by describing the contour by a Fourier series and solving the stability problem for the individual terms.

Mullins and Sekerka treated two mathematically equivalent cases: diffusion controlled crystallization from a dilute solution and heat transfer controlled crystallization of a melt (121). The growth distribution on a sphere distorted by a harmonic perturbation was determined. The boundary conditions at the sphere included the effect of capillarity on the activity of the crystal surface. Since a curved surface has a higher free energy than a flat surface, the crystallization

potential is also higher. The stabilizing effect of capillarity is inversely proportional to the square of the spatial period and is overcome by the destabilizing influence of diffusion or conduction control for harmonics of sufficiently large spatial period.

In the limit of low amplitude, the growth rate perturbation takes the form of the same harmonic as the surface shape perturbation. For spatial periods much smaller than the overall dimension of the contour, the surface can be regarded as a plane, and the perturbation expanded as a two dimensional Fourier sine series. Sekerka extended the mathematical treatment (122), and Coriell and Hardy applied it to a cylindrical geometry (123).

In a series of three papers, McGeough and Rasmussen presented a perturbation analysis of the electroforming process (100-102). In the first paper they applied Wagner's solution of the primary current distribution at a sinusoidal profile to the components of a Fourier series representing an arbitrary shape of low amplitude (100). The growth rate distribution was determined by multiplying the local current density by an assumed current efficiency that declined in a linear manner with increasing current density. It was shown that application of a periodic reverse current produces a stable surface profile for certain values of the slope of the current efficiency versus current density curve.

The validity of this simulation is questionable since it includes neither mass transfer nor kinetic resistance. Although the good macro throwing power of the copper cyanide plating bath, particularly in periodic reverse current deposition, has been attributed to a decline in current efficiency with increasing current

density (2), the current efficiency should depend on fraction of limiting current as well.

In a second paper, McGeough and Rasmussen extended the analysis to DC deposition to determine the conditions for levelling (101). A third report extended the treatment to soluble or conforming anodes (102).

Aogaki and coworkers in a series of papers have described experimental results for steady-state galvanostatic deposition of silver and developed a stability analysis that includes concentration resistance and surface diffusion of adatoms. In the stability analysis, the solution for an advancing flat surface was found, and a perturbation of the concentration field was applied (103). The perturbation took the form of a two dimensional Fourier series with an exponential time dependence. A perturbation in the rate of advance of the surface of the same form was then assumed. Substitution of these conditions into the time-dependent diffusion equation gave an implicit expression for the concentration perturbation and the rate of growth perturbation. The time constant for exponential growth was found by solving the diffusion controlled current distribution subject to the boundary conditions imposed by the growing surface. These included capillarity but not kinetic polarization. Although the boundary condition for the concentration perturbation far from the cathode was applied inconsistently, this did not affect the result. Due to the effect of capillarity, the growth rate was negative for spatial periods smaller than about one tenth micron, while for larger spatial periods the surface was shown to be unstable.

In their second paper (104), Aogaki and coworkers described an analysis of galvanostatic deposition with simplifying assumptions and obtained for the rate of amplitude growth

$$\frac{\partial \ln A}{\partial t} = \sqrt{2}\, D\, \kappa\, \omega\, \nu \frac{RT\, G_c - \dfrac{2\, \nu\, \gamma\, \omega^2\, c_i}{nF}}{D\, (nF)^2\, c_i + \kappa\, RT} \qquad (2\text{-}12)$$

where

$$2\omega^2 = \omega_x{}^2 + \omega_y{}^2$$

G_c is the concentration gradient at the surface, D the diffusivity of the metal ion, γ the surface free energy, c_i the concentration of metal ion at the interface and ω_x and ω_y the spatial frequency in the x and y directions respectively. The second term in the numerator of equation 2-12 is due to the capillary potential shift, ϕ_s.

$$\phi_s = \frac{\nu\, \gamma}{nF}\left(\frac{1}{r_1} + \frac{1}{r_2}\right) \qquad (2\text{-}13)$$

where γ is the surface free energy and r_1 and r_2 are the radii of curvature of the surface profile. For a two dimensional sinusoidal profile of low amplitude, ϕ_s is given by

$$\phi_s = \frac{2\, \nu\, \gamma}{nF}\, \omega^2\, A \sin(\omega_x x)\sin(\omega_y y) \qquad (2\text{-}14)$$

In two subsequent papers, Aogaki and coworkers presented theoretical and experimental treatments of silver deposition (105,106). The results of the stability analysis were applied in a mathematical simulation of roughness

development during silver deposition. The simulation predicted the spatial period of deposit roughness, or protrusion spacing, based on the amplification of substrate roughness.

The substrate topography was represented as a Fourier series, and the amplitude growth rates derived from the stability theory were applied to the individual terms. Summation of the terms produced a predicted deposit profile. Instead of describing the real surface profile, thay assumed that the substrate roughness took the form of a Gaussian distribution of surface heights positioned randomly on the surface. The authors found that real silver deposits produced a protrusion spacing in agreement with the theoretical prediction.

Aogaki et al. later extended their treatment to include the effects of diffusion of adatoms to account for the absence, in real deposits, of very short spatial period roughness predicted by the stability treatment (107). Other explanations for this absence should be considered as well, such as the kinetic overpotential, an increase in the surface energy due to adsorbed impurities and limits set on protrusion size by nucleation density.

The most complete stability analysis was presented by Landau (108). The diffusion and kinetic controlled current distribution at a sinusoidal profile was found by a perturbation analysis. A maximum in the growth rate versus spatial period curve was used to predict the predominant spatial period of roughness that should arise during prolonged deposition. It was found that a critical over-potential for roughness development can be assigned, comprising concentration and kinetic terms.

In Landau's analysis, a sinusoidal perturbation was imposed on a flat surface under conditions of diffusion controlled deposition. The resulting current distribution, accounting for the kinetic overpotential and the potential shift due to capillarity, which determine the boundary conditions for the diffusion equation, was then determined. The assumption of a small amplitude allowed considerable simplification through the expansion of exponentials as power series and the neglect of nonlinear terms. The resulting growth rate, as a function of spatial period is

$$\frac{\partial \ln A}{\partial t} = (\frac{D}{\frac{1}{\nu} - c_i}G_c)(\omega_d - \frac{v}{D})(\frac{G_c - \frac{2\,\gamma\,\nu}{RT}c_i\,\omega_d^2}{G_c + \frac{c_i}{\alpha}\omega_d}) \qquad (2\text{-}15)$$

v is the rate of advance of the surface. ω_d is defined by,

$$\omega_d = \frac{v}{2D} + [(\frac{v}{2D})^2 + \omega^2]^{\frac{1}{2}} \qquad (2\text{-}16)$$

The surface energy term, with a factor of two, is appropriate for surfaces curved in two dimensions, although the diffusion equation for a one dimensional profile was used in the derivation. Negative growth rates indicate stability. This occurs due to the stabilizing effect of capillarity for spatial periods smaller than about one micrometer. There is a maximum at intermediate spatial periods.

Landau concluded that for a given exchange current density a critical overpotential for roughness initiation can be specified, and that a high exchange current density contributes to the development of roughness. In section 1.4, however, it was shown that the magnitude of the exchange current density

should not affect the current distribution in the Tafel region since it does not contribute to the slope of the polarization curve. Reduction of exchange current density has been proposed as a cause of levelling by adsorbed inhibitors. This mechanism is only effective if the reduction is non-uniform, as in the case of inhibition by mass-transfer controlled adsorption. A possible explanation for the efficacy of inhibitors that Landau does not take into consideration is an increase in the surface energy. According to equation 2-15, an increase in surface energy should extend the stable region to larger spatial periods. Higher nucleation density, induced by adsorbed inhibitors would also suppress the appearance of the less stable, long spatial period protrusions.

A stability analysis which accounts for ohmic overpotential, capillarity, kinetic overpotential and concentration overpotential can be formulated. The procedure is that of Landau, with the additional consideration of the electric field.

The problem is to solve simultaneously the equations governing the concentration and electric fields for a sinusoidal perturbation of the surface contour. The potential obeys Laplace's equation.

$$\nabla^2 \phi = 0 \qquad (2\text{-}17)$$

Mass transport is assumed to occur by diffusion only and is confined to a boudary layer of thickness, δ, measured from the average surface plane. Within the diffusion layer the concentration is governed by Laplace's equation.

$$\nabla^2 c = 0 \qquad\qquad (2\text{-}18)$$

The importance of the rate of advance of the surface can be estimated through a comparison of the time required for the surface to advance by one boundary layer thickness, τ_1, with the relaxation time for a concentration transient, τ_2.

$$\tau_1 = \frac{\delta}{v} \qquad\qquad (2\text{-}19)$$

$$\tau_2 = \frac{\delta^2}{D} \qquad\qquad (2\text{-}20)$$

For copper deposition at a few amperes per square centimeter, τ_1 is much smaller than τ_2, which justifies neglect of surface motion in the diffusion equation.

For diffusion to an advancing surface, a steady state profile may be established even in a semi-infinite stagnant electrolyte. This occurs when the rate of growth of the diffusion layer, which decreases inversely with the square root of time for a constant current, becomes equal to the rate of advance of the surface. This steady state profile was used by Landau. It is shown in appendix B that the time constant for approach to this steady state is too large to be neglected. In the present study it was assumed that convective transport outside of the Nernst layer keeps the concentration at the bulk value at some constant distance, δ, from the surface.

The equations and boundary conditions are illustrated in figure 2-5. The complete derivation is given in appendix A. The amplitude growth rate is

$$\frac{\partial \phi}{\partial z} = -\frac{i_A}{\kappa}$$

$$\frac{\partial \phi}{\partial x} = 0 \qquad \nabla^2 \phi = 0 \qquad \frac{\partial \phi}{\partial x} = 0$$

$$c = c_b$$

$$\frac{\partial c}{\partial x} = 0 \qquad \nabla^2 c = 0 \qquad \frac{\partial c}{\partial x} = 0$$

$$nFD \frac{\partial c}{\partial x} = \kappa \frac{\partial \phi}{\partial x} \qquad\qquad \phi = \phi_a + \phi_c + \phi_s$$

$$z_s = A \sin(\omega x)$$
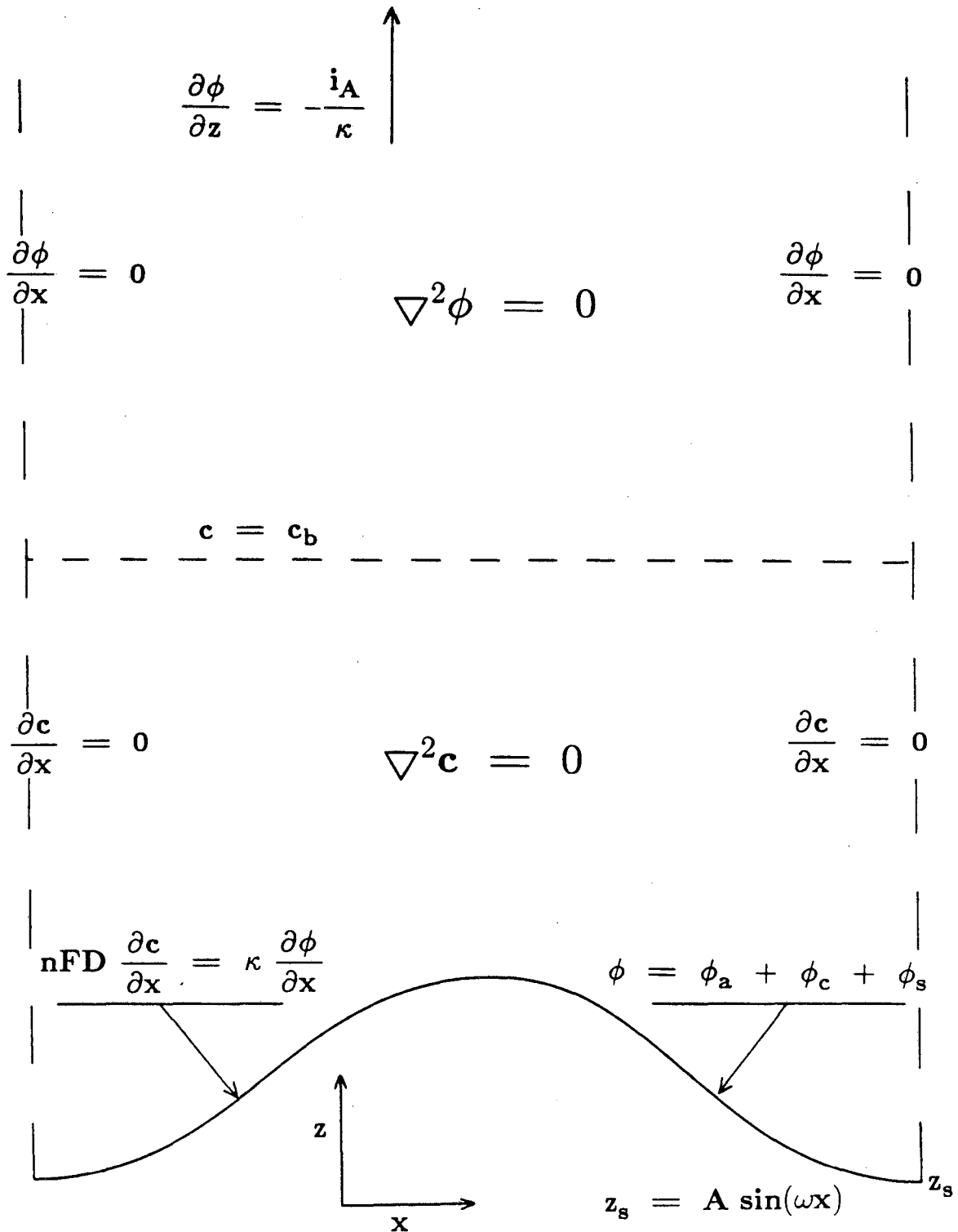
Figure 2-5: Equations and boundary conditions for current distribution on a sinusoidal profile.

$$\frac{\partial \ln A}{\partial t} = \frac{\nu}{nF} \kappa \, \omega \, \sqrt{2} \, \frac{\dfrac{RT \, i}{n^2 F^2 \, c_b \left(1 - \dfrac{i}{i_L}\right) D} - \dfrac{2 \, \nu \, \gamma \, \omega^2}{nF}}{1 + \dfrac{RT \, \kappa \, \omega}{nF \, i_L \left(1 - \dfrac{i}{i_L}\right)} + \dfrac{RT \, \kappa \, \omega}{i \, nF \, \alpha}} \qquad (2\text{-}21)$$

This can also be written

$$\frac{\partial \ln A}{\partial t} = \frac{\nu}{nF} \kappa \, \omega \, \sqrt{2} \, \frac{\dfrac{RT \, i}{n^2 F^2 c_b \left(1 - \dfrac{i}{i_L}\right) D} - \dfrac{2 \, \nu \, \gamma \, \omega^2}{nF}}{1 + Wc + Wa} \qquad (2\text{-}22)$$

The spatial frequency, ω , has been taken as the reciprocal of the characteristic dimension in equations 2-6 and 2-9. The appearance of Wc and Wa in these equations indicates that much information can be obtained by a simple calculation of these values. A large value of either number indicates a low rate of amplitude growth. For large values of Wc or Wa, neglecting the surface energy term, the conductivity and spatial period cancel out of the equation, indicating that the process is far from ohmic control. Far from limiting current, small values of Wc, Wa and the surface energy reduce the equation to the form of Wagner's solution for the primary distribution, with an inverse dependence of growth rate on spatial period.

Stability is indicated by a negative amplitude growth rate. The denominator of equation 2-22 is positive for all physically meaningful values of Wa and Wc. The numerator is negative under conditions when

$$\frac{RT\ i}{Dn^2F^2\ c_b\ (1\ -\ \frac{i}{i_L})} \ <\ \frac{2\ \nu\ \gamma\ \omega^2}{nF} \tag{2-23}$$

The Nernst diffusion layer thickness, δ, is defined as

$$\delta\ =\ \frac{i_L}{c_b\ nF\ D} \tag{2-24}$$

Solution of 2-24 for c_b and substitution in 2-23 gives

$$\frac{RT\ \frac{i}{i_L}\ \delta}{nF\ (1\ -\ \frac{i}{i_L})} \ <\ \frac{2\ \nu\ \gamma\ \omega^2}{nF} \tag{2-25}$$

With the definition of a dimensionless parameter

$$Ws\ =\ \frac{2\ \nu\ \gamma\ \omega^2}{\delta\ RT} \tag{2-26}$$

the stability criterion becomes

$$\frac{\frac{i}{i_L}}{1\ -\ \frac{i}{i_L}} \ <\ Ws \tag{2-27}$$

Equations 2-12 and 2-15 can be put in a form similar to that of equation 2-21 with the following substitutions.

$$G_c\ =\ \frac{i}{nFD} \tag{2-28}$$

$$c_i\ =\ c_b\ (1 - \frac{i}{i_L}) \tag{2-29}$$

$$\frac{1}{\dfrac{1}{\nu} - c_i} \approx \nu \tag{2-30}$$

Equations 2-12 and 2-15 become respectively

$$\frac{\partial \ln A}{\partial t} = \frac{\nu}{nF} \kappa \omega \sqrt{2} \frac{\dfrac{RT\,i}{n^2F^2Dc_b(1 - \dfrac{i}{i_L})} - \dfrac{2\,\nu\,\gamma\,\omega^2}{nF}}{1 + \dfrac{\kappa\,RT}{Dn^2F^2c_b(1 - \dfrac{i}{i_L})}} \tag{2-31}$$

$$\frac{\partial \ln A}{\partial t} = \frac{\nu}{nF} \omega \frac{\dfrac{RT\,i}{Dn^2F^2c_b(1 - \dfrac{i}{i_L})} - \dfrac{2\,\nu\,\gamma\,\omega^2}{nF}}{\dfrac{RT}{Dn^2F^2c_b(1 - \dfrac{i}{i_L})} + \dfrac{\omega\,RT}{\alpha\,nF\,i}} \tag{2-32}$$

The stability criterion defined by all three equations is the same. Stability is unaffected by the activation and ohmic overpotentials and is controlled by the fraction of limiting current, the mass transfer boundary layer thickness and the surface energy. The transition from stable to unstable growth occurs at a spatial period of one micrometer or less, the scale of brightening as opposed to levelling. It follows that the effectiveness of brightening agents may be a result of their influence on surface energy.

There are differences in the magnitude of the predicted growth rates and, significantly, in their dependence on perturbation spatial period. Aogaki's formulation predicts no variation of the average spatial period of roughness with current density or fraction of limiting current because it does not include the

kinetic overpotential which enters both of the scaling parameters Wa and Wc. Landau's formulation predicts a decrease in average spatial period with both increasing current density and increasing fraction of limiting current. In both cases the second term in the denominator, which contains ω, becomes small relative to the first, and the growth rate becomes proportional to ω. The formulation derived here also indicates a decrease in spatial period with increasing current density. However, it predicts an increase in average spatial period with increasing fraction of limiting current since this increases the magnitude of the second term in the denominator which contains ω. All of the equations predict increasing amplitude of roughness with increasing current and with increasing fraction of limiting current up to a limiting value. The stability theory derived here is consistent with the observations made at the end of section 2.3 with the exception of the predicted increase of spatial period with increasing fraction of limiting current.

Landau's equation lacks the first term in the denominator of equation 2-21 which corresponds to the ohmic contribution. Aogaki's equation lacks the third term which represents the kinetic overpotential. All three equations reduce to Wagner's solution in the appropriate limits.

Factors other than growth stability are expected to influence the spatial period of roughness observed, and the stability criterion only places limits on the possible range. Some perturbations that arise will be suppressed by the surface force. Most perturbations will grow, and the rate at which perturbations of a given geometry are initiated may be as important a determinant of surface

topography as the rate at which they grow once initiated. The following section is concerned with the possible influences of nucleation and flow phenomena on the initiation and growth of surface perturbations.

2.5 Nucleation and Flow Phenomena

Differences in growth rates between crystal faces are the most common initial sources of perturbation leading to roughness in a deposition process. At high current densities, copper deposit roughness has a rounded appearance, and faceting is not obvious. Kindler, however, showed that rounded protrusions may have their origin in the development of large single crystals which are subsequently covered over by surface "fine structure" (109). Studies of copper deposition at low current densities show clear faceting of copper deposits (110).

Even if faceted crystallites do not grow, the density and location of nucleation should have an effect on the development of roughness. Kindler found that copper deposition at high current densities produces a higher number density of nucleation than deposition at low current densities. This has also been observed in pulse plating, where the pulse current density may be very high. If the high nucleation rate is due to high kinetic overpotential, or crystallization far from equilibrium, high current density deposition should produce denser nucleation, and the surface features that develop should be more closely spaced. Dense nucleation in pulse plating, however, may be a consequence of factors unique to pulsed current deposition, such as inhibition of the process during the off-time

period.

Another reason to expect shorter spatial period of roughness at high current density is suggested by Ibl's comments on pulse plating (124). He speculated that pulse plating generates a mass transfer boundary layer with two regions. Inside the steady state diffusion layer is a thin pulsating diffusion layer which follows the topography of the surface (see figure 2-6). Larger features are uniformly inhibited by the pulsating layer and hence are not amplified. A detailed mathematical treatment of the pulsating diffusion layer has been presented by Cheh (125), Pesco and Cheh (126) and Viswanathan et al. (127). Since the mass transfer boundary layer for high current density must be thinner than for low current density to maintain a given fraction of limiting current, it should follow progressively smaller surface features as the current density is increased.

There is evidence that growing crystallites inhibit the nucleation of new crystallites in their vicinity. (128,129,130). If the mechanism of nucleation exclusion is reduction of the local supersaturation, thinning of the diffusion layer should produce a higher number density of nucleation.

The development of roughness in metal deposition is sometimes attributed to "3-D nucleation". Ogata and coworkers, for example, regarded the onset of 3-D nucleation at a critical overpotential as the cause of roughness in copper deposition (131). Their definition of 3-D nucleation, however, does not refer to crystallization phenomena, but simply to the appearance of visible surface protrusions. Since they don't report the fraction of limiting current for their
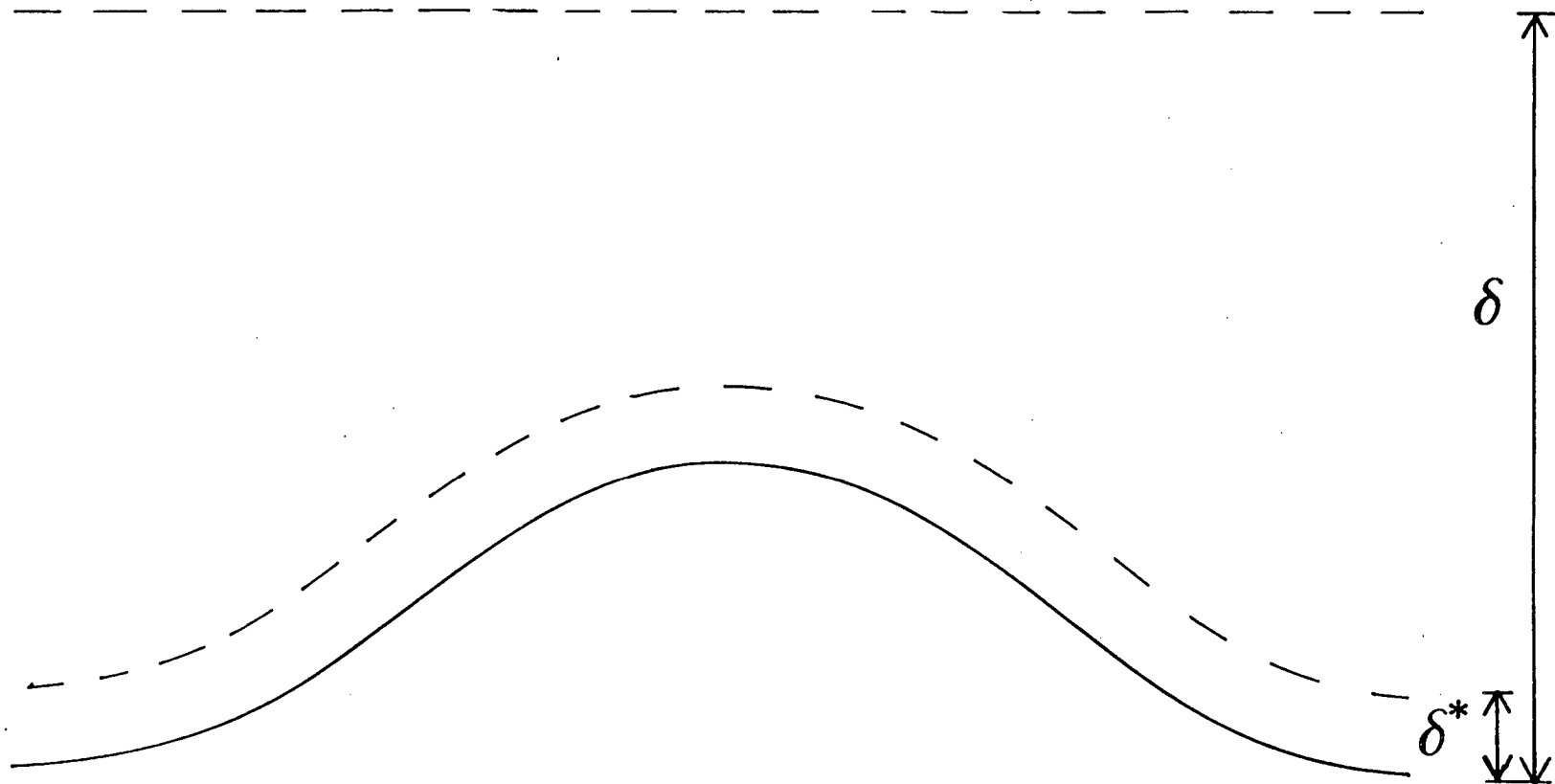
Figure 2-6: Mass transfer boundary layer of thickness δ is non-uniform over the profile, while thinner layer, of thickness δ^*, follows the profile. After N. Ibl (122).

experiments, the critical overpotential may simply be a measure of the approach to limiting current density.

The use of cathode movement or fluid flow to enhance mass-transfer at the cathode introduces local stirring effects at the surface which may interact with developing surface features. The Reynolds number for flow past an obstacle is

$$Re = \frac{Vd}{\nu} \qquad (2\text{-}19)$$

where V is the flow velocity, d is the object dimension and ν is the kinematic viscosity of the electrolyte. For the system used in this study, Re is roughly equal to the protrusion height in micrometers. Flow separation can therefore be expected for features larger than one micrometer. The vortices generated by flow separation can be expected to increase mass transfer resistance immediately downstream of the protrusion and to decrease it where the flow reattaches. Since the spatial period of this variation is limited by eddy size, flow phenomena may selectively amplify features of larger spatial period. Increased flow velocity would generate smaller eddies, and hence amplify finer surface features.

Alkire and coworkers investigated transport of dissolution products from small cavities (132). This may be analogous to deposition between closely spaced protrusions. Transport resistance was found to be significant for Peclet numbers less than one. Since the Schmidt numbers of the electrolytes used in this study were of the order of 2000, this type of inhibition under typical conditions of stirring or flow is unlikely to occur.

# Chapter 3: Experimental Apparatus and Materials

3.1 The Rotating Cylinder Electrode

The deposition and limiting current studies were carried out with a rotating cylinder electrode (RCE) centered in a cylindrical cell equiped with radial baffles. The RCE was 15 cm in overall length (figure 3-1). The active area of the electrode was a stainless steel cylinder of length 1.8 cm and diameter 4.4 cm. A one degree taper, with the narrow end at the bottom of the electrode, permitted removal of intact electroforms. Stainless steel, a material often used as a substrate for electroforming, was chosen as the electrode material. It can be polished to a high degree, retains its surface finish well and is inert to nitric acid, which was used to clean the electrodes and to strip copper deposits between limiting current measurements. Not only is stainless steel a hard and strong material, but because of a passive film on it removal of electroforms can be easily accomplished without damage to the substrate.

The active electrode area was bounded by PTFE sleeves (figure 3-2). The sleeves protruded 3 mm from the electrode surface and formed a right angle with it. They were added to suppress edge effects on the current distribution.

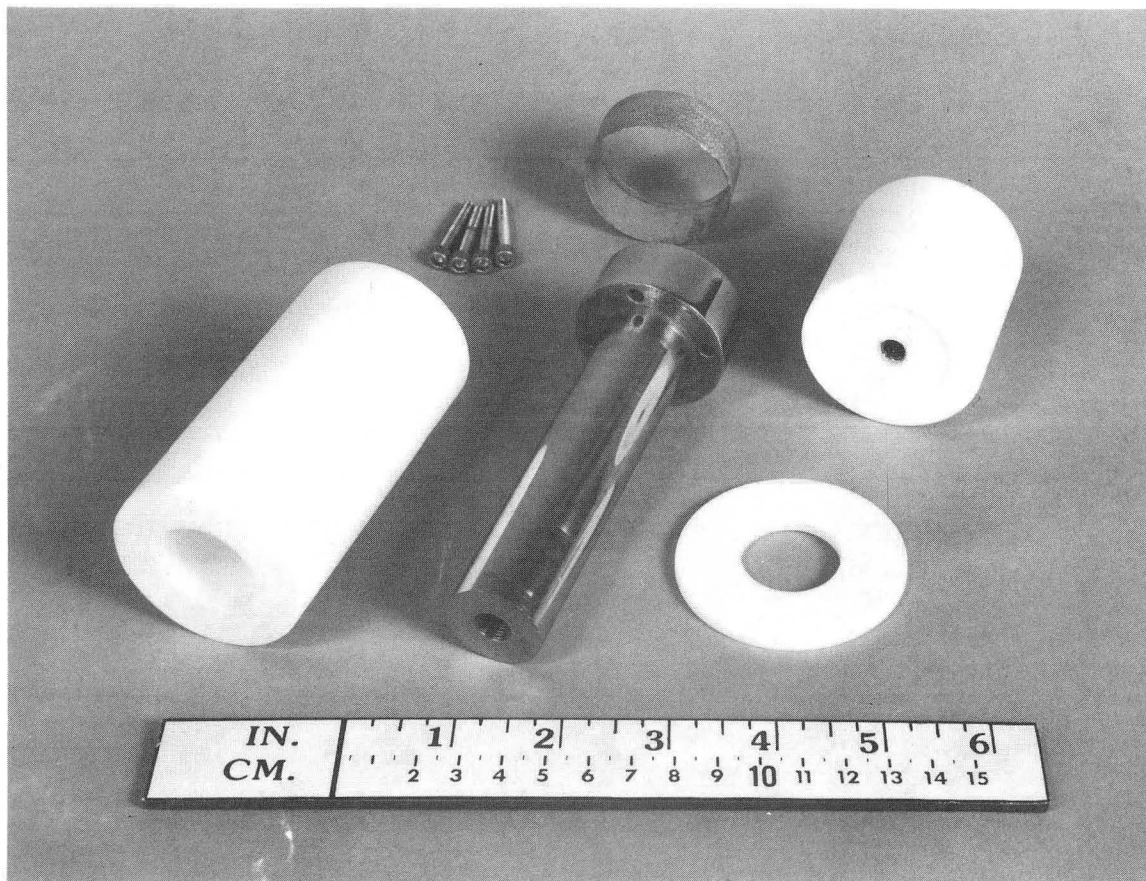## 3.2 The Electrolysis Cell

The RCE was immersed in a cylindrical pyrex reaction vessel of 3 liter volume (figure 3-3). The top of the cell was covered with PTFE sheet, but was not sealed. The active portion of the electrode was submerged about 6 cm
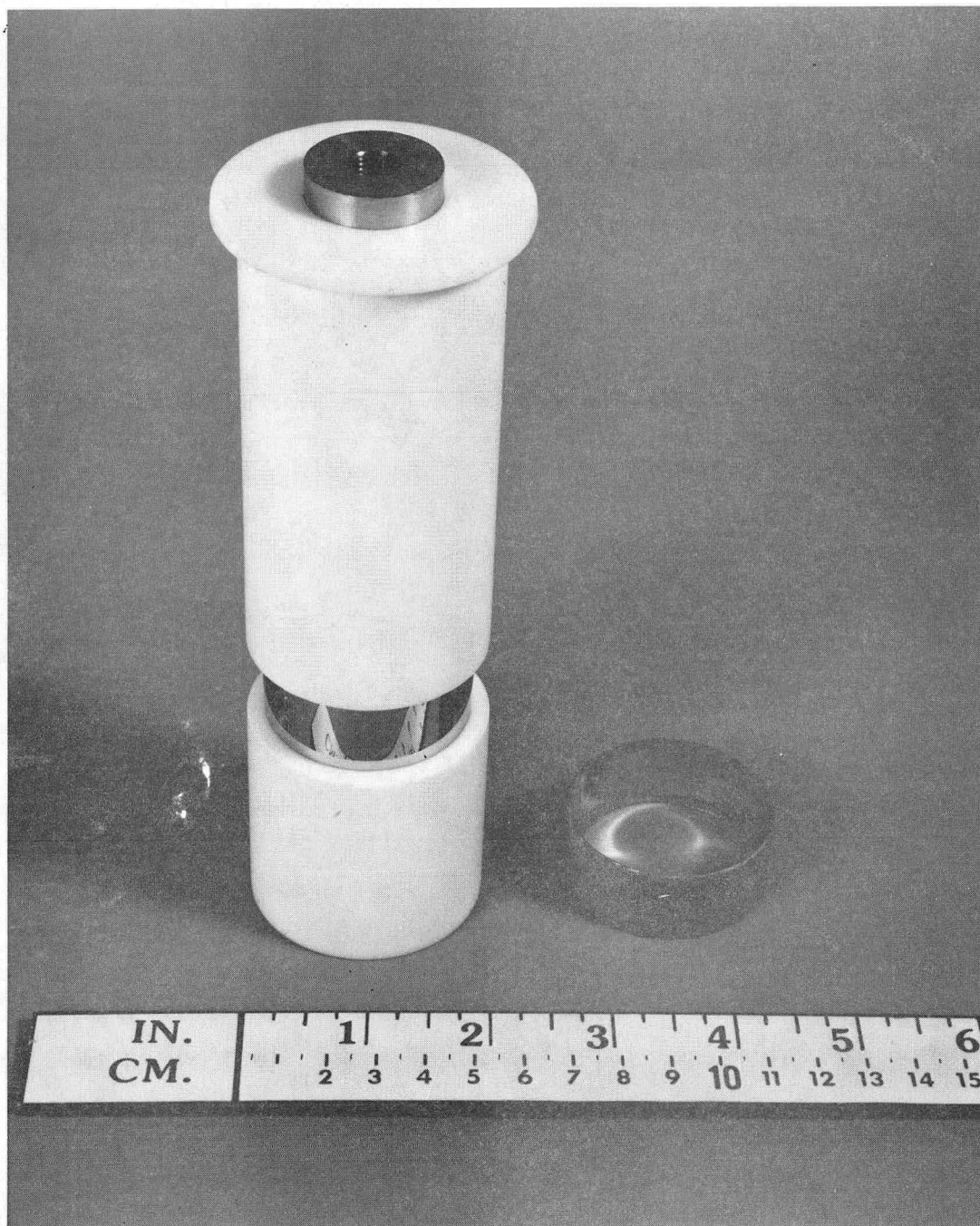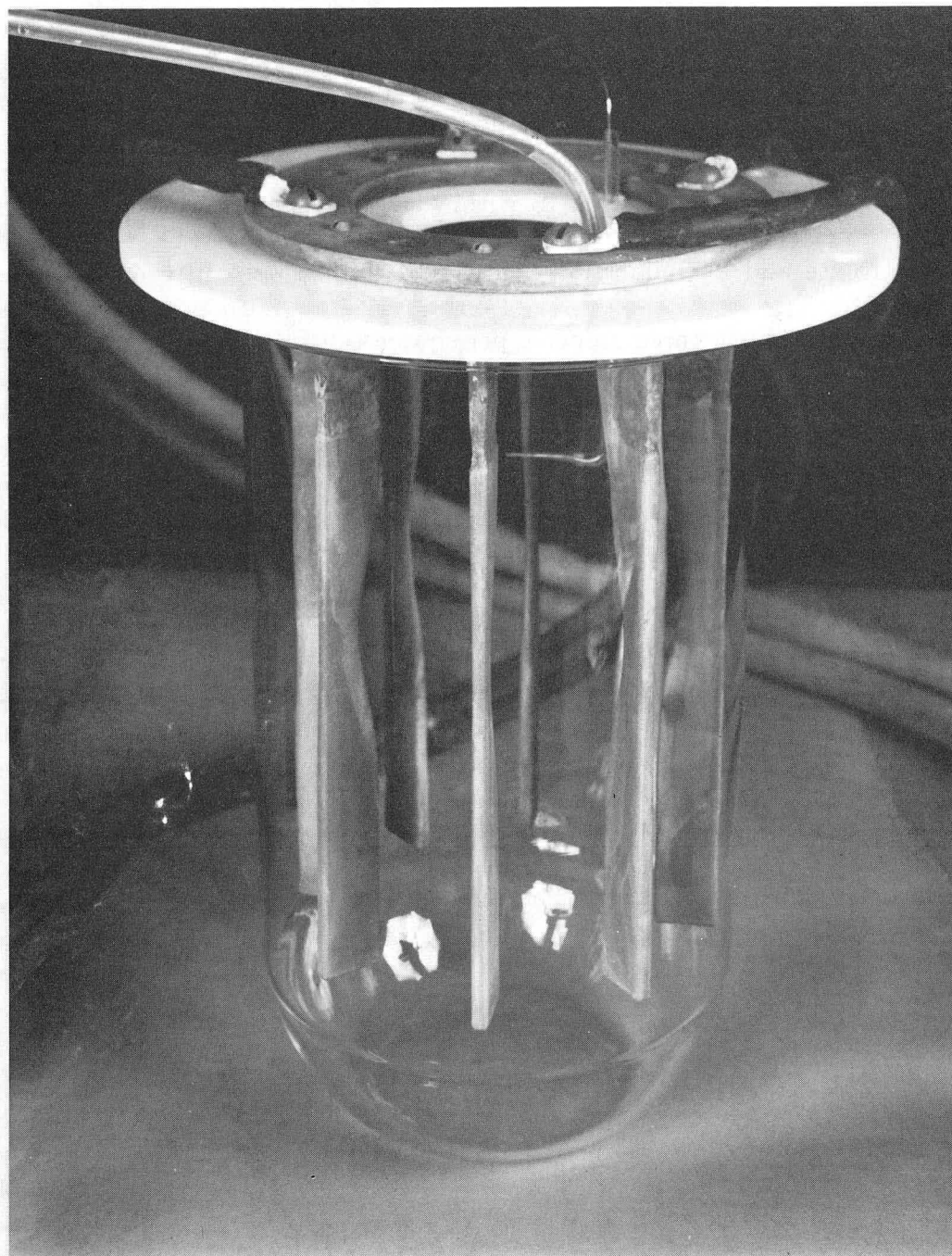
Figure 3-1: Rotating cylinder electrode.

XBB 877-5877

Figure 3-2: Rotating cylinder electrode parts.

XBB 876-5403

Figure 3-3: Electrolysis cell.

below the free electrolyte surface. With the RCE in place, a PTFE disk, attached near the top of the RCE, covered the opening in the cell top.

The cell rested in a constant temperature bath equipped with a heating element and a coil of copper tubing which acted as a heat exchanger (figure 3-4). The temperature was controlled to within two degrees using a thermocouple in the electrolyte and an immersion heater and cooling coils in the constant temperature bath. Above three amperes per square centimeter, the temperature was controlled to within five degrees. The constant temperature bath and cell rested on a table that was raised and lowered with a jack (figure 3-5). The table was lowered to permit replacement of the RCE. The RCE was immersed in the cell by raising the table.

A circular array of eight copper anodes, each 20 cm long, 2 cm wide and .5 cm thick, was supported at the top by a copper ring. The anodes were machined from 99.9999% pure copper. The ring was attached to the top of the PTFE sheet covering the cell. The anodes were attached to the ring by brass screws, which also acted as electrical contacts. The top of the anodes was pressed flush against the PTFE sheet to prevent contact of electrolyte with the brass screws or support ring. Deposition experiments were all conducted with the anodes arrayed as radial baffles, both to supress the entrainment of air by the vortex and to enhance mass transfer (figure 3-6).

The reference electrode was a Luggin capillary inserted into the cell through the top. The opening faced the cathode at an oblique angle, opposing the direction of rotation so as to prevent air from being drawn into the
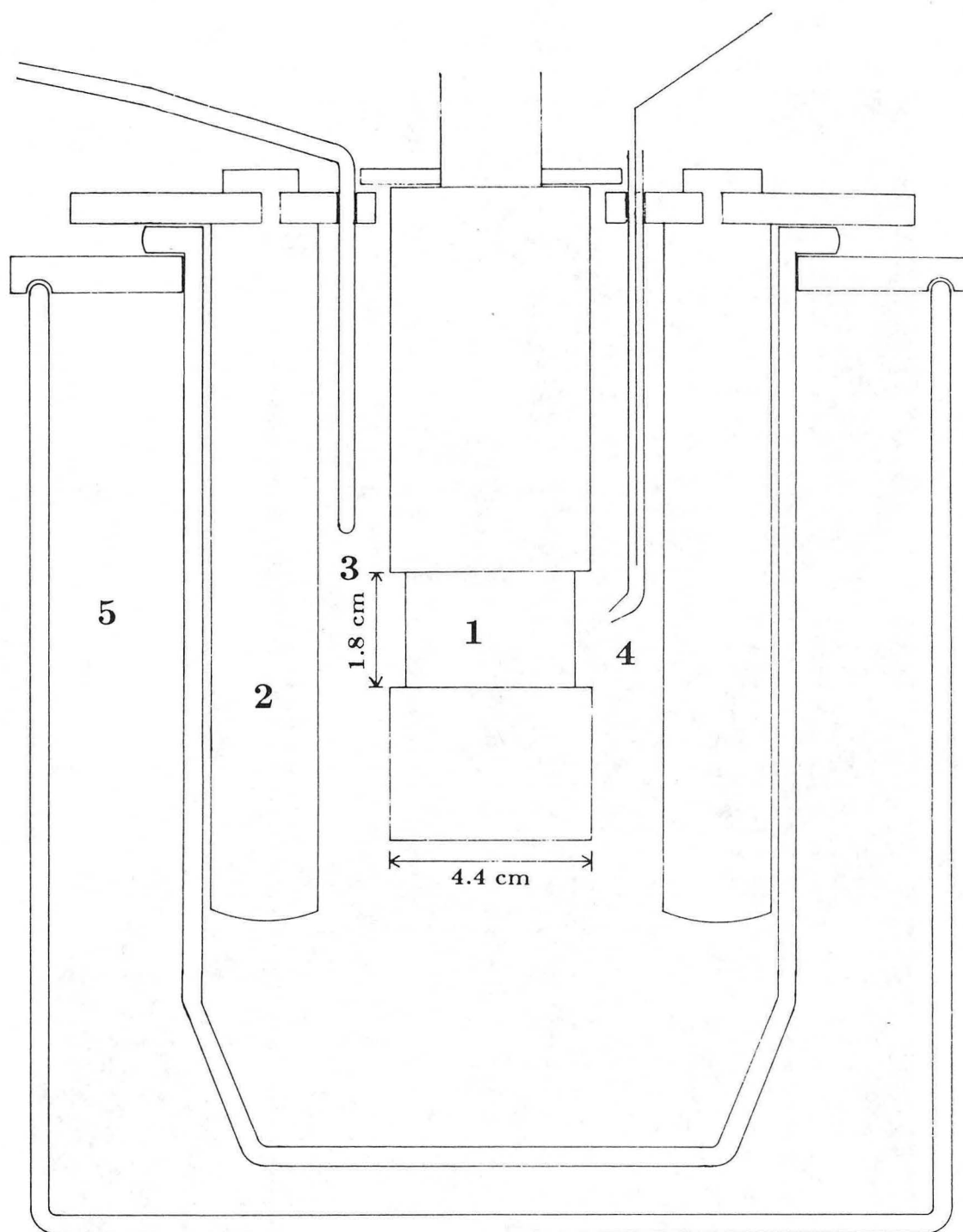
XBL 877-3238

Figure 3-4: Electrolysis Cell. 1) Cathode, 2) Anode, 3) thermoprobe,
4) Reference Probe, 5) Constant Temperature Bath.
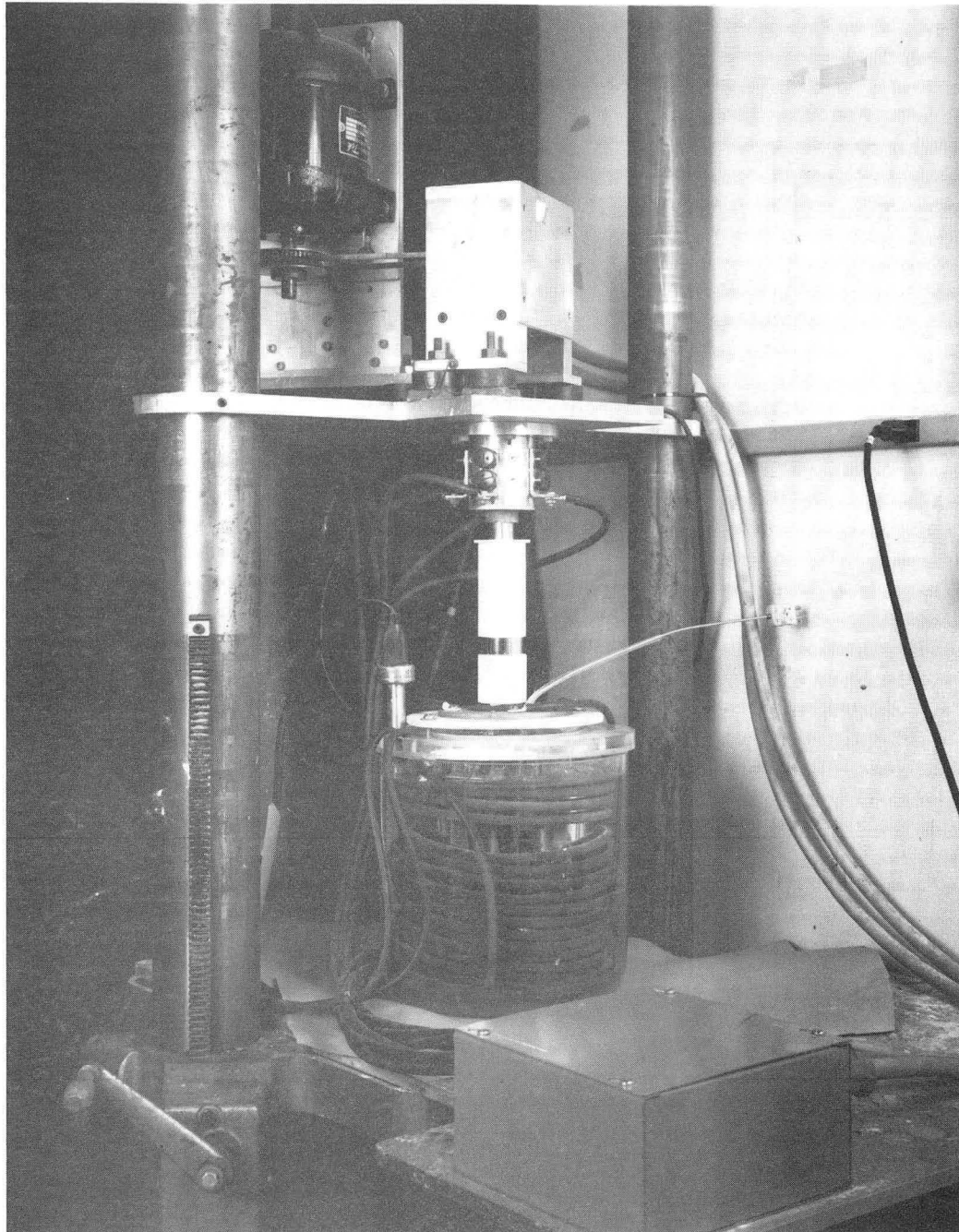
CBB 877-5942

Figure 3-5 Electroforming Apparatus
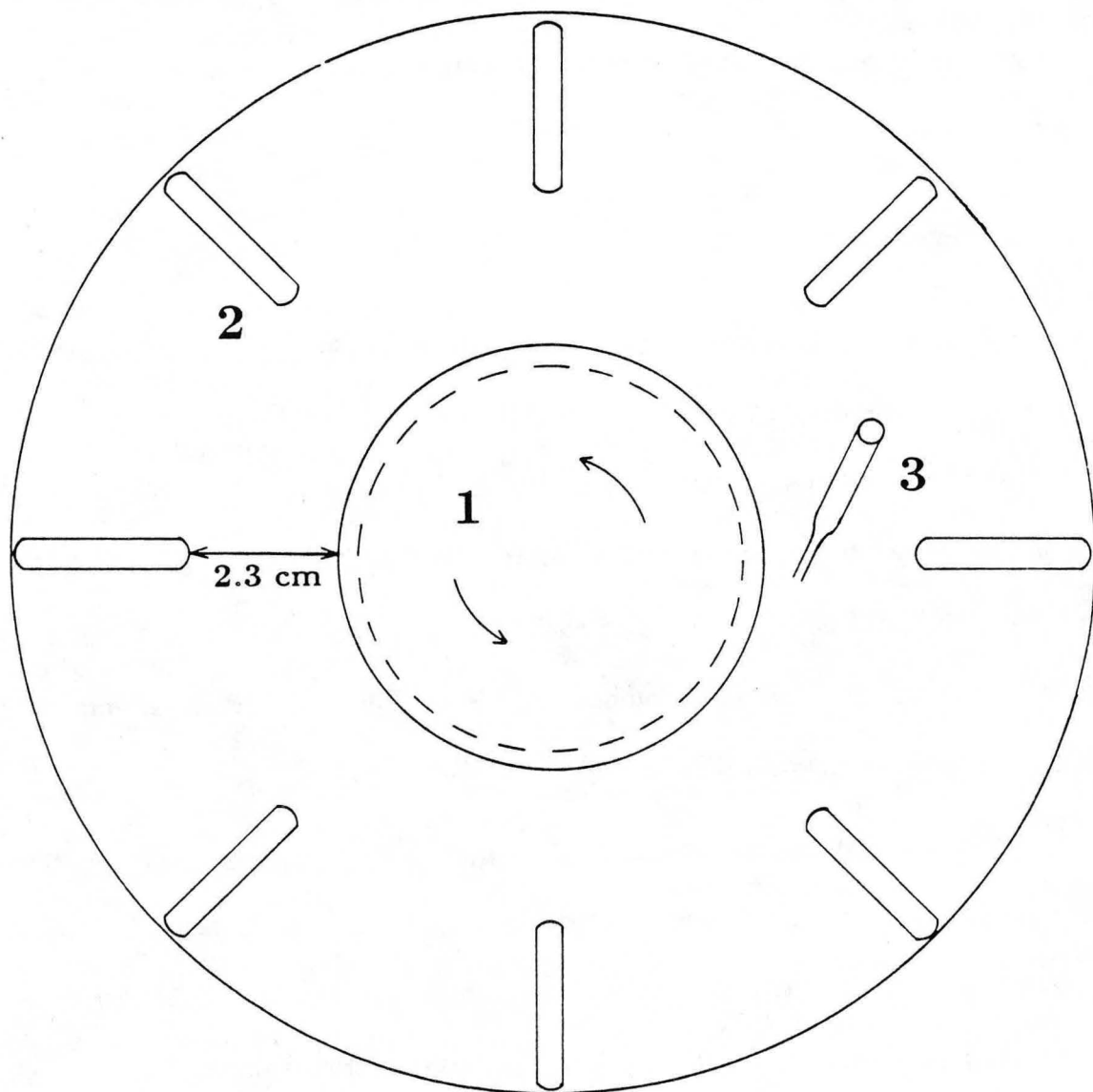
Figure 3-6 Top view of electrolysis cell. 1) Cathode, 2) Anode, 3) Reference Probe.

XBL 877-3237

capillary. The capillary tip was placed about two millimeters from the electrode surface for the high-rate limiting current measurements, while for low currents the placement was increased to two centimeters from the cathode to minimize interference with the flow.

3.3 External Components

The cell and external components are shown in figure 3-7. The RCE was driven by a 1/4 horsepower motor (Servo-Tek model STE-231) with a variable controller (Servo-Tek model 450). The motor drove a spindle, held in place by high speed bearings, through an insulating joint. The RCE was attached to the spindle by a threaded fitting. Electrical contact to the spindle was through an array of eight 80/20 silver/graphite compound brushes (Fabricast Brush Assembly PN 092003) mounted between the bearings.

Cell current was provided by a 50 volt, 200 ampere programmable power supply (Electronic Measurement Corporation TCR 50T200 Power Supply). The current output of the power supply was controlled by an EG&G Princeton Applied Research Corporation model 175 Universal Programmer. The current was stable to 0.1% in galvanostatic operation.

During galvanostatic operation, conditions in the cell were recorded with a Molytek model 2700 digital multipoint recorder. Temperature was measured with a chromel-alumel thermocouple. Current was measured through a resister in series with the cell. Cell voltage and reference potential were also recorded. For fast current sweep experiments, the reference potential and cell curent were
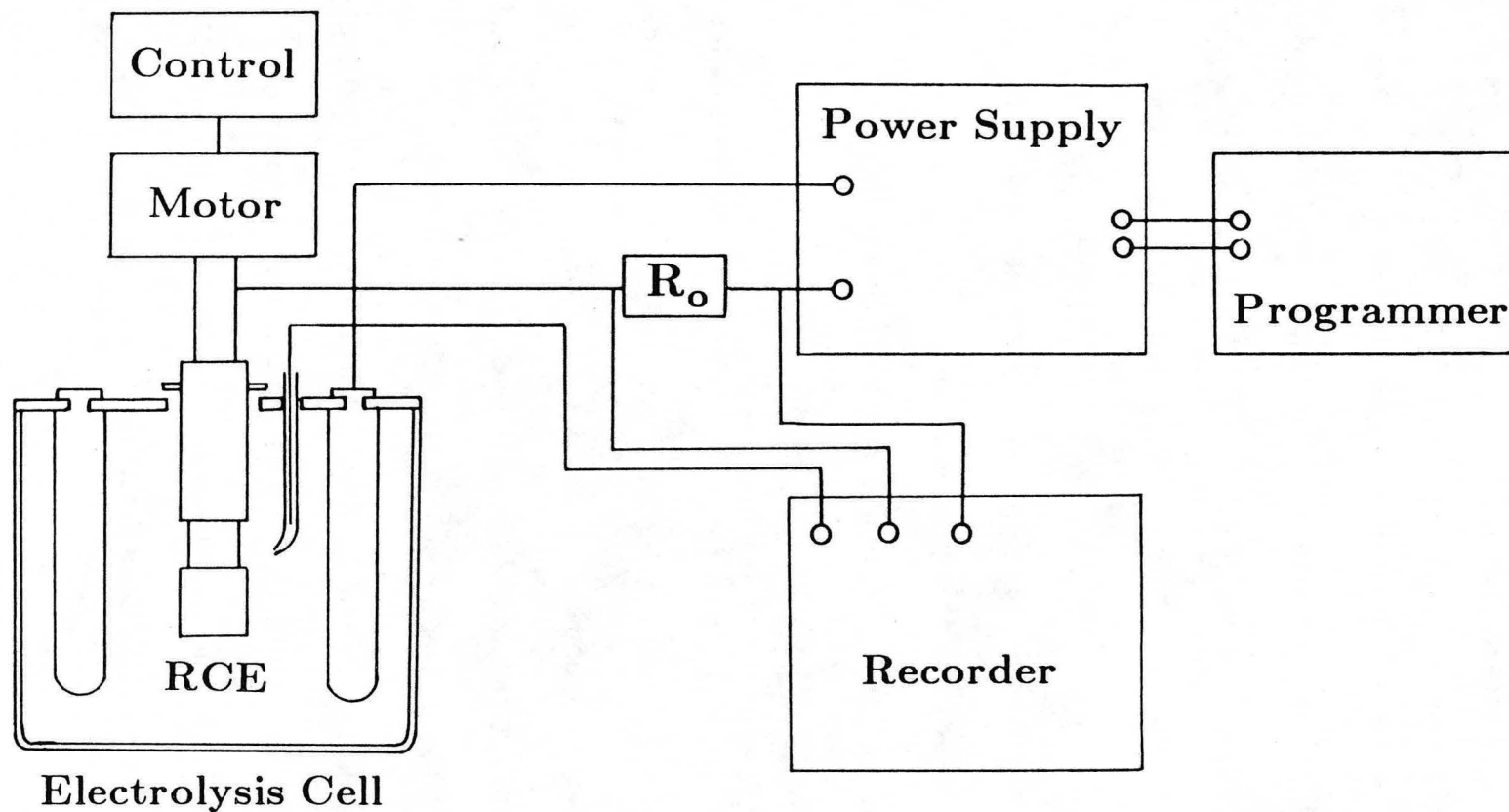
Figure 3-7 Electroforming Apparatus and External Components

XBL 877-3254

recorded with a Hewlett Packard model 7044B X-Y recorder.

3.4 Surface Characterization

Deposit surface topography was characterized by computer implemented analysis of digital surface profiles. The profiles were obtained with a Clevite Skidless Surfanalyzer 150, equipped with a five micrometer radius diamond stylus. The signal from the Surfanalyzer was processed through an analog to digital converter and recorded in digital form on a DEC LSI-11 73 computer. The deposits were held in a specially constructed mount for acquisition of profiles (figure 3-8). Surface profiles along four evenly spaced lines parallel to the electrode axis and four profiles along the circumference were recorded for each deposit.

The rate of sampling of the surfanalyzer signal by the computer could be varied through the data acquisition program. Digital profiles of three different point densities are shown in figure 3-9. The profiles used in the statistical analysis of surface roughness were each one centimeter in length and contained 2048 points taken at five micrometer intervals.

Deposit surfaces were also examined with an AMR 1000 scanning electron microscope. Views of the surface at various inclinations were photographed with the SEM. Optical photographs at low magnification were also taken to characterize the overall deposit structure.
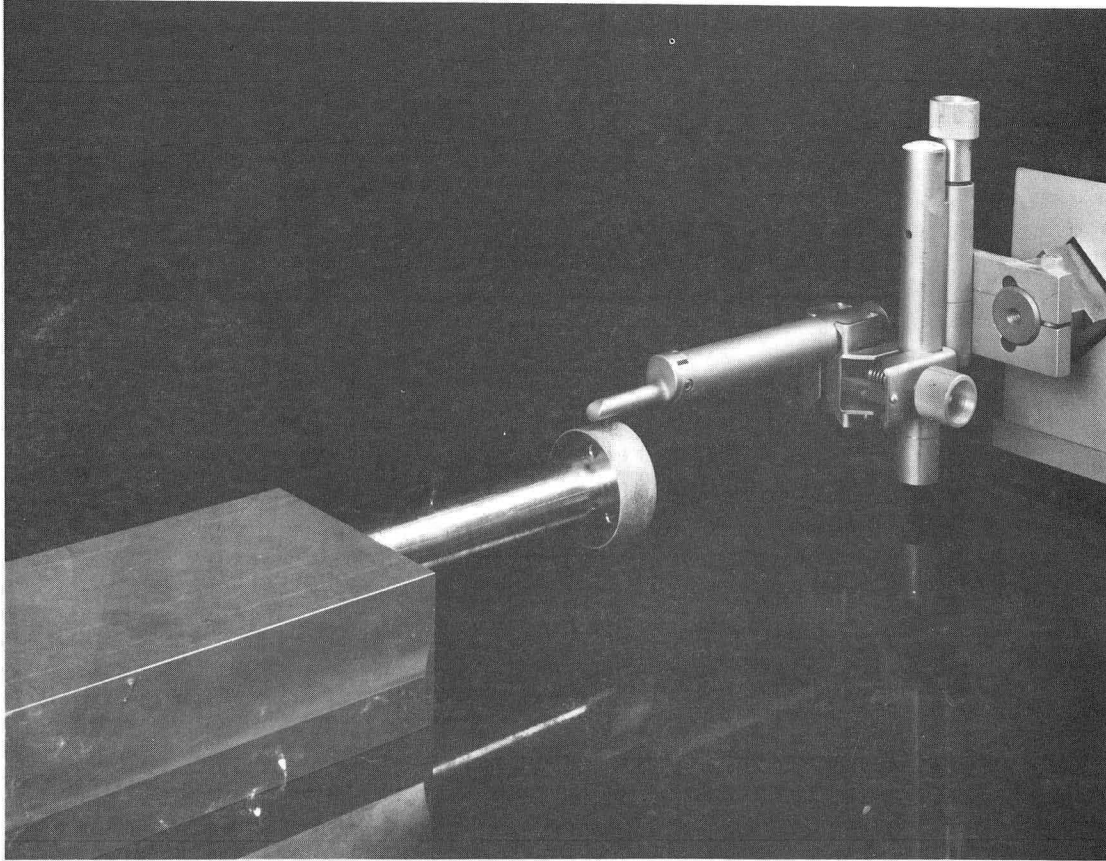
CBB 876-5407

Figure 3-8 Profilometer

Surface Profiles

A   0.4 mm   10 μ

B   4.0 mm   10μ

C   40.0 mm   50 μ
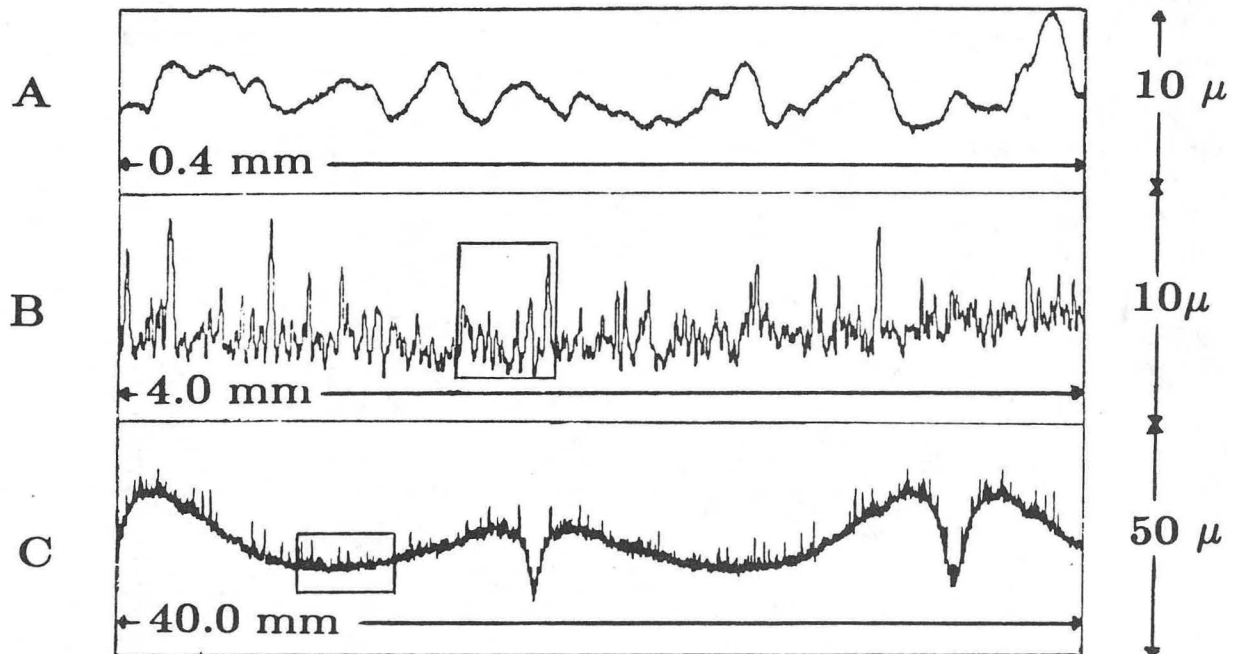
XBL 877-3272

Figure 3-9 Digital Profiles of Deposit Surfaces

3.5 Determination of Deposit Properties

Deposit mechanical properties were characterized by three measures: density, microhardness and tensile strength. The microhardness was measured with a Buehler Micromet Microhardness Tester. The tensile strength of sample coupons was determined with an Instron model 1125 Universal Testing Instrument. Samples were cut from the electroforms with a jeweler's saw. Deposit density was measured by weighing the deposits in air and in water.

3.6 Electrolyte and Substrate Preparation

All electrolytes were prepared with reagent grade $CuSO_4$–$5H_2O$ (Mallinckrodt Analytical Reagent), reagent grade H_2SO_4 (Baker Analysed Reagent) and distilled, deionized water. The copper concentration was determined by iodometric titration and the acid concentration by titration with NaOH solution.

In most of the deposition and limiting current studies the cathode substrate was stainless steel. The surface was prepared by sanding with 600 grit silicon carbide paper and polishing with one micrometer diamond compound. A few copper substrates were prepared by plating a 20 micrometer copper layer at low current density and electropolishing it in 85% phosphoric acid.

Stainless steel electrodes were cleaned with acetone, propanol and distilled, deionized water, then immersed in 70% nitric acid before a final rinse with distilled, deionized water. The PTFE and stainless steel cathode parts were disassembled and immersed for one week in 70% nitric acid between series of

experiments.

Electroforms were rinsed in distilled, deionized water immediately after forming. They were then removed from the cathode by rapping the upper edge with a copper bar. Samples for SEM were cut from the electroforms with a jeweler's saw after the surface profiles were recorded.

Chapter 4. Limiting Current Measurements

4.1 The Rotating Cylinder Electrode

4.1.1 Reasons for Choice of the RCE

The rotating cylinder electrode was chosen for these studies for two reasons. Turbulent flow conditions are established already at low rotation rates for the RCE, and high rates of mass transfer can be achieved without the complexities characteristic of channel flow systems. Mass transfer rates have also been reliably correlated with the Reynolds and Schmidt numbers for the case of a concentric cylindrical counter electrode (133). The second reason for choosing the RCE was the favorable current distribution. For a cylinder of infinite length, or one with insulating sleeves extending to a concentric cylindrical counter electrode, the primary current distribution is uniform. Even with sleeves that protrude only part of the way to the counter electrode, the primary current distribution is fairly uniform. The mass-transfer resistance is also uniform for the infinitely long cylinder. The protruding sleeves reduce this uniformity; for this reason the sleeve thickness was set at a compromise value in this study.

4.1.2 Previous Studies

Reviews of the RCE have been published by Gabe (134) and by Gabe and Walsh (135). The first extensive study of mass transfer to the RCE was reported by Eisenberg, Tobias and Wilke, (ETW) (133). For a wide range of

Reynolds and Schmidt numbers, their results were well correlated by

$$i_L \;=\; .079\frac{nFDc_b}{d}Re^{0.7}Sc^{0.356} \tag{4-1}$$

Robinson and Gabe measured limiting currents in agreement with equation 4-1 (136,137). A theoretical treatment by Kawase and Ulbrecht based on the Levich three-zone model was also in agreement (138). Several experimental studies of the laminar vortex regime, including the effects of imposed axial flow have been reported (139-140).

The ETW correlation is valid for smooth cylinders in the turbulent regime. Ibl has outlined the possible influences of surface roughness on limiting current (77). For small-scale roughness, the surface is effectively smooth. If the scale of roughness is comparable to or greater than the mass transfer boundary layer thickness it should increase the limiting current by offering a larger cross section for transport. If the scale of roughness is comparable to or greater than the thickness of the hydrodynamic boundary layer, it may increase the limiting current by stirring, although the effect depends on the geometry of the roughness. Large, closely spaced peaks could decrease the limiting current by inhibiting the recessed areas between them.

A critical Reynolds number for the onset of roughness induced stirring has been proposed by Kappesser, Cornet and Greif (142).

$$Re_c \;=\; (11.8\frac{d}{\epsilon})^{1.18} \tag{4-2}$$

where ϵ is the scale of roughness and d the electrode dimension. Below this critical value, the RCE is effectively smooth. For rough surfaces, it has been observed that the mass transfer coefficient increases in direct proportion to the Reynolds number (143-145) rather than in proportion to the 0.7 power of the Reynolds number as for smooth cylinders.

Gabe and Walsh have studied limiting currents on the RCE for both smooth and rough surfaces. For surfaces roughened by powdery metal deposition, they found that the limiting current increases in direct proportion to the Reynolds number (144,145). Gabe and Makanjuola measured limiting currents to RCE's with surfaces of known texture produced by knurling and by winding wire or gauze around the cylinder (146). Their purpose was to evaluate the performance of various surface textures as transport promoters for application of the RCE in electrosynthesis. The features produced were not comparable to the sharp, dendritic roughness produced by metal deposition at the limiting current, but were rounded with a relatively large radius of curvature. They found that textured surfaces can produce a several fold enhancement of limiting current, but to a much lesser degree, of limiting current density based on true surface area.

The effect of stirring on transport was separated from the increase due to the greater surface area of the textured surface by converting the measured limiting current to a real current density. Several of the electrodes, while having a texture on a scale greater than the mass transfer boundary layer thickness, showed no enhancement of the adjusted limiting current. Gabe and

Makanjuola concluded that the scale of roughness must be orders of magnitude greater than the mass transfer boudary layer thickness to produce such enhancement. It seems likely that the geometry of surface irregularity is important as well. The textures studied were composed of large, rounded features. The correlation for the onset of microstirring by a roughened surface, (eqn. 4-2), may be a more appropriate criterion for sharp, powdery roughness.

The effect of baffles in a cylindrical cell with an RCE has been the subject of at least one experimental investigation by Ravoo (147). Ravoo reported a correlation of the form:

$$\text{Sh} \ = \ 1.83 \, \text{Re}^{0.58} \, \text{Sc}^{0.33} \qquad (4\text{-}3)$$

Since baffle arrangements can assume a large variety of geometries, a correlation developed for a given cell cannot be generalized. However, despite this limitation the demonstration of mass transfer enhancement is of interest because of the potential application of the RCE in cells with baffles.

4.2. Measurement of Limiting Currents of Metal Deposition

Limiting currents of high-rate metal deposition on the RCE were measured to characterize the mass-transfer conditions in the electrolysis cell used for the deposition experiments. Measurement of the limiting currents was also of interest because no previous investigators had measured limiting currents of metal deposition in this high-rate regime directly. The rapid changes in surface texture produced by metal deposition near the limiting current, (148), make

such measurements difficult. In addition, the effectiveness of baffles as mass transport promoters could be evaluated.

Eisenberg, Tobias and Wilke measured limiting currents of $K[FeCN_6]$ reduction at a rotating cylinder electrode by determining the steady state polarization curve (133). For metal deposition at high rates this method is not suitible because of the development of surface roughness on the cathode near the limiting current. One technique for avoiding the problem of roughness development is to measure the limiting current of a trace ion that is codeposited with the metal forming the bulk of the deposit. Degrez and Winand found the limiting current for a channel cell by codepositing a small amount of silver with the bulk copper deposit (93). The silver partial current, which was the limiting current since the silver was present in dilute form, was determined by analysis of the deposit. The cathode was not roughened because the copper was deposited far from its limiting current.

It is not necessary to deposit the less noble metal to find the limiting current of the tracer. Ettel, Tilak and Gendron measured limiting currents for a channel cell with an acid sulfate copper electrolyte by depositing silver at a potential more positive than that of copper deposition (149). In this case the conditions were not strictly the same as for copper deposition since there was no mass transfer boundary layer for copper ion. In both methods it is important to account properly for the difference in diffusivities of the ions, since the limiting current density is generally not simply proportional to the diffusivity.

A common technique for measurement of limiting currents is to sweep the potential or current at a sufficiently low rate to reproduce the steady state polarization curve. Selman used this method to measure limiting currents of copper deposition at low rates on a rotating disk electrode (150). The mass transfer rate to a rotating disk is well established, and Selman was able to correlate diffusivities of the copper ion in sulfate solution. These diffusivities are applicable to transport across a mass transfer boundary layer in which the composition of the electrolyte changes with position.

4.3 Experimental

In this study, limiting currents of high rate metal deposition on an RCE were measured by a current sweep method. Rates of current density sweep varied from 1.5 A/cm^2–s to 6.0 A/cm^2–s. Variation of the sweep rate within this range did not affect the limiting currents observed.

An upper limit on the rate of sweep is set by the requirement that the deposition process remain close to the steady state. Too high a rate of sweep overshoots the limiting current because the surface concentration falls to zero before the steady-state mass-transfer boundary layer is established. Under this condition, a current higher than the steady state mass transfer limited current can be sustained for a short time. Approach to the steady state by depletion of the mass transfer boundary layer occurs with a time constant, τ (150).

$$\tau = \frac{\delta^2}{D} \qquad (4\text{-}4)$$

In this study, τ was in the range 10^{-3} to 10^{-1} seconds. Sweep rates were chosen such that at least ten time constants elapsed before the limiting current was attained.

To avoid the complications of roughness, sweep rates were chosen to keep the average thickness of metal deposited during a measurement smaller than the Nernst diffusion layer thickness, δ.

$$\delta = \frac{c_b nFD}{i_L} \qquad (4\text{-}5)$$

where i_L was estimated from the ETW correlation.

The Reynolds and Schmidt numbers were varied from 10^4 to 2×10^5 and from 8×10^2 to 8×10^3 respectiveley. Cupric sulfate concentrations were varied from .375M to 1.14M, sulfuric acid concentrations from 1.0M to 2.58M and the temperature from $15°$ to $65°$ C.

Correlation of experimental results required calculation of the physical and transport properties of the electrolytes. Viscosities and densities were determined from the correlations reported by Price and Davenport (151). Their correlations apply to copper electrowinning solutions in the composition and temperature ranges used in this study. Diffusivities and transference numbers, accounting for the dissociation of bisulfate, were estimated using, respectively, a correlation and a computer implemented routine developed by Selman (152). Properties of the electrolytes used are presented in table 4-1.

Table 4-1: Physical Properties of Electrolytes.

[$CuSO_4$] (M/l)	[H_2SO_4] (M/l)	Temperature (C)	Kinematic viscosity (cm^2/s)	Diffusivity (cm^2/s)	Cu^{++} Transference number
1.05	1.00	25.	0.0212	0.456×10^{-5}	0.123
1.05	1.00	50.	0.0131	0.808×10^{-5}	0.123
1.05	1.00	65.	0.0102	1.090×10^{-5}	0.123
0.96	1.03	25.	0.0205	0.456×10^{-5}	0.113
1.00	1.03	50.	0.0129	0.806×10^{-5}	0.116
0.97	1.99	50.	0.0137	0.720×10^{-5}	0.064
0.325	2.58	25.	0.0183	0.359×10^{-5}	0.018
0.325	2.58	15.	0.0227	0.278×10^{-5}	0.018
1.000	1.00	50.	0.0129	0.808×10^{-5}	0.119
0.0107	1.99	20.	0.0144	0.373×10^{-5}	0.001
0.0134	2.00	20.	0.0145	0.372×10^{-5}	0.001
0.0149	1.60	20.	0.0135	0.410×10^{-5}	0.002
0.0130	2.40	18.	0.0165	0.319×10^{-5}	0.001

4.4 Results

4.4.1 Interpretation of Polarization Curves

The polarization curves obtained did not display wide and flat limiting current plateaus. Even when the reference probe was placed within a millimeter of the cathode surface, the combined kinetic and ohmic overpotential was large in comparison with the width of the limiting current plateau. To accomodate the entire curve on the recorder output chart, a large scale on the overpotential axis was required, and the limiting current plateau was correspondingly small and difficult to distinguish. The rotation of the electrode also introduced fluctuation in the overpotential measured by the reference probe because of either slightly eccentric motion of the RCE or noise at the contact between the brushes and the cathode spindle. This fluctuation, combined with the relatively small deflection of the polarization curve at the limiting current, made interpretation of the polarization curves difficult.

Because the current kept on increasing gradually between the onset of rapid increase in concentration polarization and the onset of the consecutive reaction, the plateaus were tilted. The values measured therefore depended on which portion of the polarization curve was used to determine the limiting current. It was decided to use a point half way between the ends of the plateau. The method adopted to extract limiting current values from the tilted limiting current plateaus is illustrated in figure 4-1.
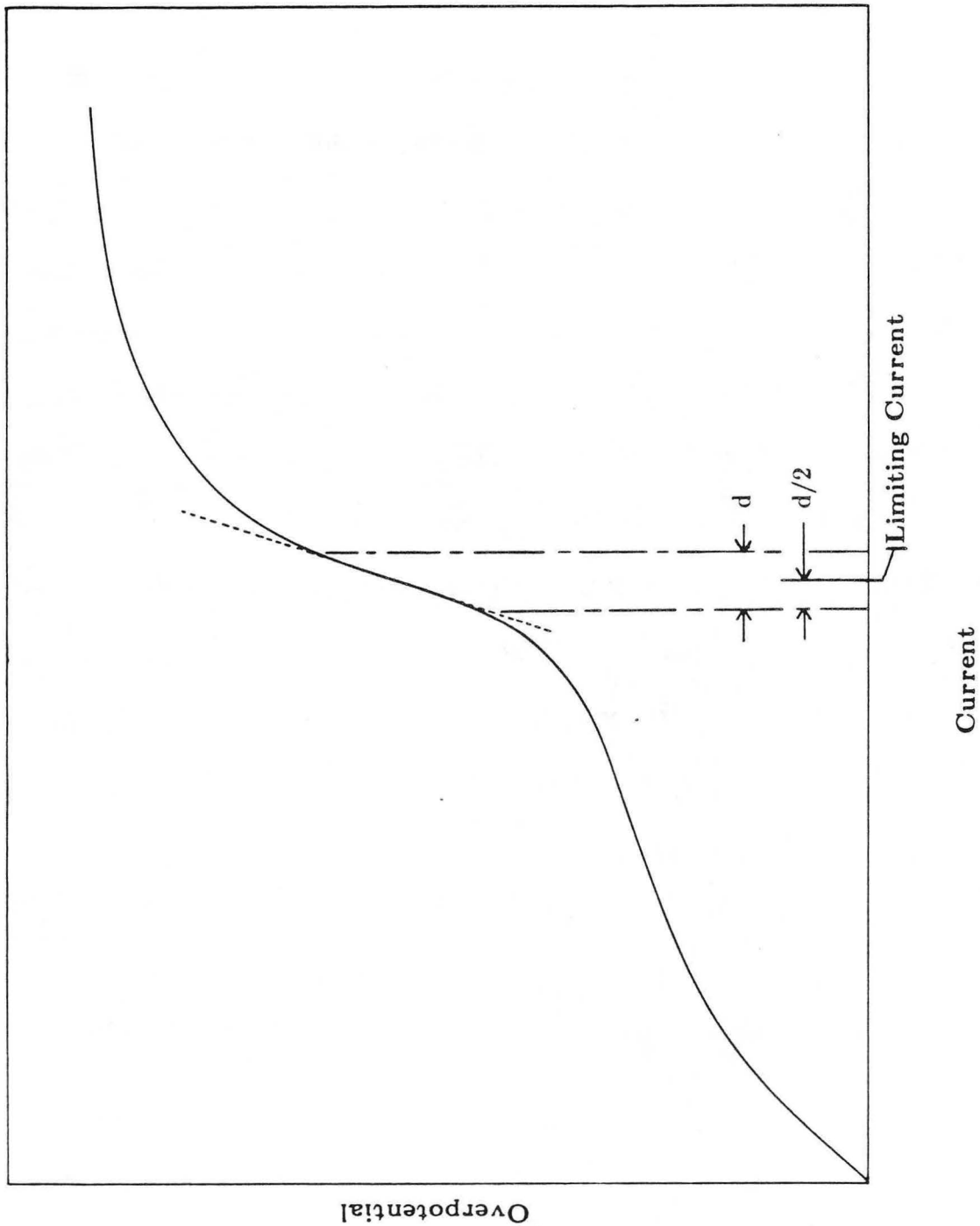
Figure 4-1 Interpretation of Polarization Curves

Inclination of the limiting current plateau indicates that the limiting current density is different on the surface, depending on axial position, and that the limiting condition is not reached simultaneously over the electrode surface. This is probably because the insulating sleeves interfere with the vortex flow in the corners where they meet the electrode.

4.4.2 Limiting Currents of High Rate Copper Deposition

The results of 116 limiting current measurements on a stainless steel substrate are shown in figure 4-2 and table 4-2. The measured limiting current densities are plotted against the values predicted by the ETW correlation. In figure 4-3, the results of measurements on electropolished copper substrates are shown. In both cases the measured values are about twice the values predicted by the correlation. Reproducibility on stainless steel was inferior due to the growth of large, widely separated copper islands. The growth of copper on the electropolished copper substrate during the measurements was much more dense and uniform (figure 4-4). Electropolishing the steel substrate did not improve reproducibility because the copper growth islands did not adhere to the polished cathode.

The factor of two discrepancy between the measured limiting currents and the values calculated from the ETW correlation cannot be attributed to roughening of the cathode by deposition because the measured limiting currents were proportional to the 0.7 power of the Reynolds number. The difference is without doubt due to the geometry of the electrolysis cell. The ETW
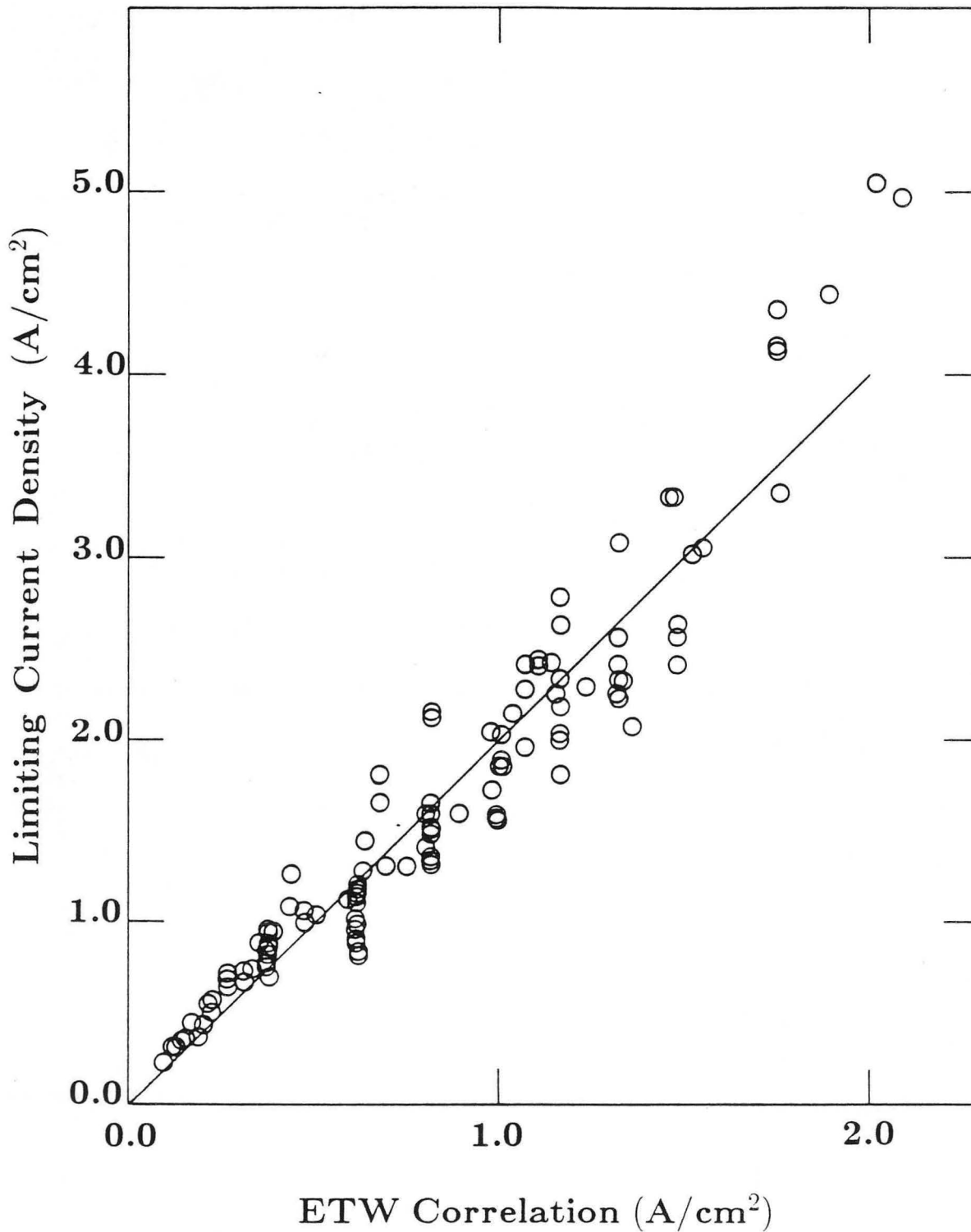
Figure 4-2 Limiting currents of high rate metal deposition on an RCE versus the correlation of Eisenberg, Tobias and Wilke. Line corresponds to ETW correlation multiplied by two.

XBL 877-3234

Table 4-2: Limiting current densities of copper deposition at the RCE in a cell with radial baffles. Limiting current densities calculated from the ETW correlation are also given.
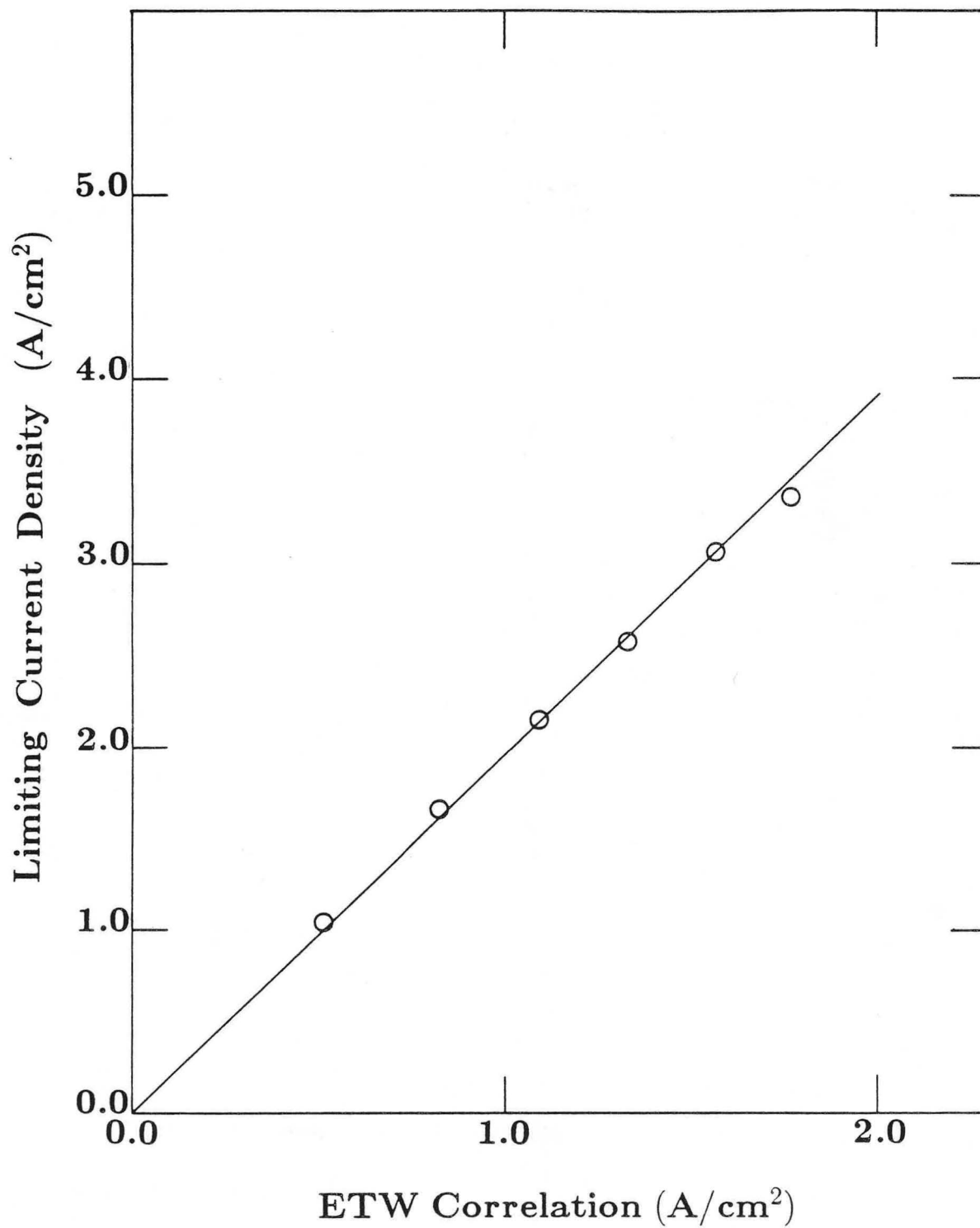
[CuSO$_4$] (M/l)	[H$_2$SO$_4$] (M/l)	Temperature (C)	Rotation Rate (RPM)	Limiting Current Density (A/cm^2)	ETW Correlation (A/cm^2)
1.05	1.00	25.	1560.	1.74	0.99
			1760.	2.04	1.07
			0750.	1.13	0.59
			0550.	1.07	0.48
			0950.	1.31	0.70
			1160.	1.41	0.80
			1360.	1.60	0.90
			1760.	1.96	1.07
			1960.	2.26	1.16
			2170.	2.29	1.24
			1760.	2.42	1.07
			0550.	0.99	0.48
			1060.	1.31	0.75
1.05	1.00	50.	0550.	1.60	0.81
			1160.	2.08	1.37
			1360.	3.02	1.53
1.05	1.00	65.	0750.	3.09	1.33
0.96	1.03	25.	0550.	1.09	0.44
			0950.	1.28	0.64
			1360.	1.59	0.82
			1760.	2.05	0.98
			2170.	2.43	1.14
			2570.	2.42	1.28
			2170.	2.81	1.34
			0950.	1.45	0.64
			0550.	1.27	0.44
1.00	1.03		1800.	4.15	1.76
			1800.	4.15	1.76
			1800.	4.38	1.76
			0600.	2.15	0.82
			0600.	2.15	0.82
			1000.	2.34	1.17
			1000.	2.64	1.17
			1000.	2.79	1.17
			1400.	3.32	1.48
			2200.	5.06	2.03
0.97	1.99	50.	0600.	1.81	0.68
			0600.	1.66	0.68
			1200.	2.42	1.11
			1200.	2.42	1.11
			1800.	3.17	1.47

Table 4-2 continued.

[CuSO$_4$] (M/l)	[H$_2$SO$_4$] (M/l)	Temperature (C)	Rotation Rate (RPM)	Limiting Current Density (A/cm^2)	ETW Correlation (A/cm^2)
			0600.	1.74	0.68
			1200.	2.42	1.11
			2200.	3.77	1.69
			1800.	3.17	1.47
			2600.	4.45	1.90
			3000.	4.98	2.10
0.325	2.58	25.	1800.	0.71	0.27
			1800.	0.69	0.27
			0600.	0.30	0.13
			0800.	0.36	0.15
			3000.	0.95	0.39
			1200.	0.44	0.21
			2600.	0.89	0.35
			1400.	0.57	0.23
			2200.	0.73	0.31
			2000.	0.73	0.29
			0600.	0.32	0.13
			1000.	0.36	0.18
			1400.	0.50	0.23
			1800.	0.60	0.27
			1800.	0.66	0.27
			2200.	0.66	0.31
0.325	2.58	15.	0600.	0.23	0.10
			1000.	0.35	0.14
			1400.	0.44	0.18
			1800.	0.55	0.21
			0200.	0.94	0.38
			0600.	1.32	0.82
			0800.	1.59	1.01
1.00	1.00	50.	0200.	0.76	0.38
			1000.	1.81	1.17
			0200.	0.91	0.38
			0400.	1.00	0.62
			0600.	1.43	0.82
			0200.	0.85	0.38
			0400.	0.83	0.62
			0400.	0.91	0.62
			0400.	0.91	0.62
			0400.	0.87	0.62
			0400.	0.89	0.62
			0400.	0.98	0.62

Table 4-2 continued.

| [CuSO$_4$] (M/l)	[H$_2$SO$_4$] (M/l)	Temperature (C)	Rotation Rate (RPM)	Limiting Current Density (A/cm^2)	ETW Correlation (A/cm^2)
1.00	1.00	50.	0400.	1.13	0.62
			0200.	0.70	0.38
			0600.	1.36	0.82
			0200.	0.76	0.38
			0200.	0.81	0.38
			0400.	1.13	0.62
			0600.	1.36	0.82
			0800.	1.59	1.01
			1000.	2.04	1.17
			1200.	2.26	1.33
			1400.	2.64	1.49
			0800.	1.89	1.01
			1200.	2.26	1.33
			1400.	2.42	1.49
			1200.	2.34	1.33
			1000.	2.00	1.17
			0800.	2.04	1.01
			0600.	1.51	0.82
			0400.	1.13	0.62
			1400.	2.57	1.49
			1200.	2.42	1.33
			1000.	2.82	1.17
			0800.	1.85	1.01
			0600.	1.51	0.82
			0400.	1.13	0.62
			0200.	0.87	0.38
			0300.	1.04	0.51
			0600.	1.66	0.82
			0900.	2.15	1.09
			1200.	2.56	1.33
			1500.	3.06	1.56
			1800.	3.36	1.77

Figure 4-3 Limiting Currents of high rate copper deposition on an RCE pre-plated with copper and electropolished. Line corresponds to ETW correlation multiplied by two.

A

B

XBB 877-6094

|——| 10 μm

|——| 100 μm
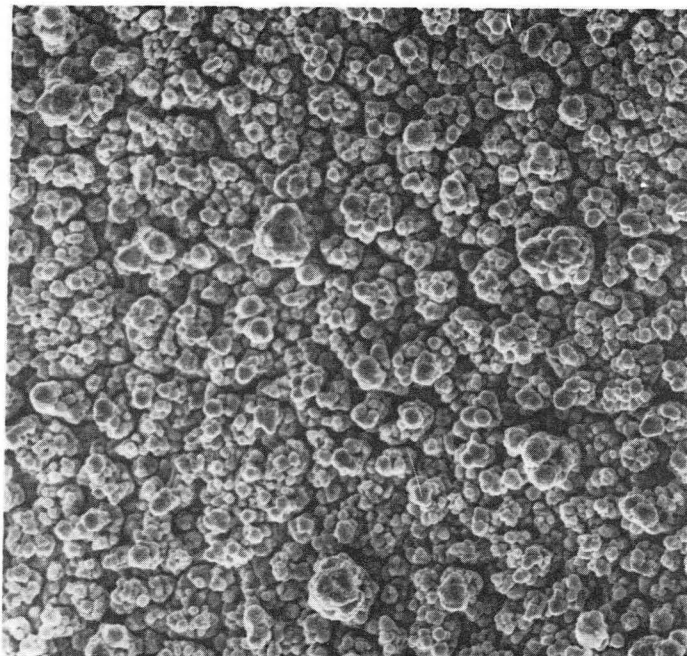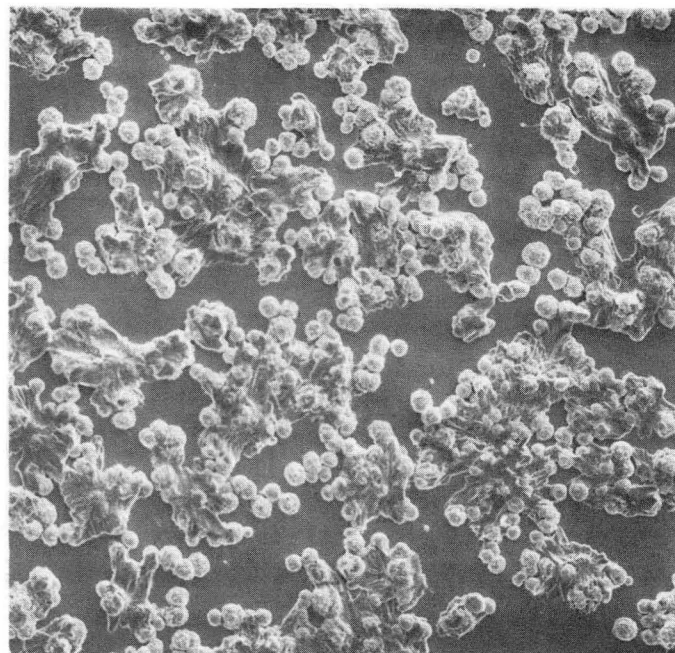
Figure 4-4 Electron micrographs of electrode surface after limiting current measurement. A) Electropolished copper cathode. B) Mechanically polished stainless steel electrode.

correlation applies to long cylinders in a cell with a concentric cylindrical counter electrode and no baffles or free liquid surface. To determine the influence of cell geometry on the limiting current, measurements of limiting currents with several cell geometries were undertaken.

4.4.3 Effect of Cell Geometry

Limiting currents of deposition from several electrolytes dilute in $CuSO_4$ and well supported with H_2SO_4 solution were measured at 20° C. Dilute solutions were used becuse low current densities relax the constraints on sweep rate that apply to high rate measurements and permit the use of a given substrate several times before the original surface must be restored. A smooth, bright copper substrate was prepared by plating the stainless steel with copper from a concentrated solution containing the levelling agent thiourea.

To determine the effects of the radial baffles, a cylindrical anode of ten centimeter diameter was fitted into the cell. To determine the effect of sleeve geometry, a set of sleeves was machined to fit flush with the electrode surface. The cell geometry which most closely approximates that used by Eisenberg, Tobias and Wilke is that of an RCE with flush sleeves and a concentric cylindrical counter electrode. Even with these modifications, however, the cell used here differs in having a free liquid surface, a short active length on the RCE and a gap of about 5 centimeters between the end of the RCE and the bottom of the cell.

The measured limiting currents with protruding sleeves and a concentric cylindrical anode were proportional to the 0.7 power of the Reynolds number and were in agreement with the ETW correlation. The measurments were repeated for the same electrolyte as above with protruding sleeves in the cell with baffles. Limiting currents with the baffles in place were greater by a factor of nearly two than those without the baffles. The limiting currents are shown in figure 4-5.

It is not surprising that baffles should produce a substantial increase in limiting curent. With careful optimization of cell geometry, their effectiveness as transport promotors could perhaps be increased further. The results obtained for dilute solution indicate that the unique cell geometry used here increases the limiting current to the RCE. The influence of the baffles may depend on the fluid properties in ways not reflected in the Reynolds number. Determination of the dependence of mass transfer enhancement on fluid viscosity and Schmidt number would require an extensive set of measurements for any given baffle arrangement. Such a study was beyond the scope of the present investigation.
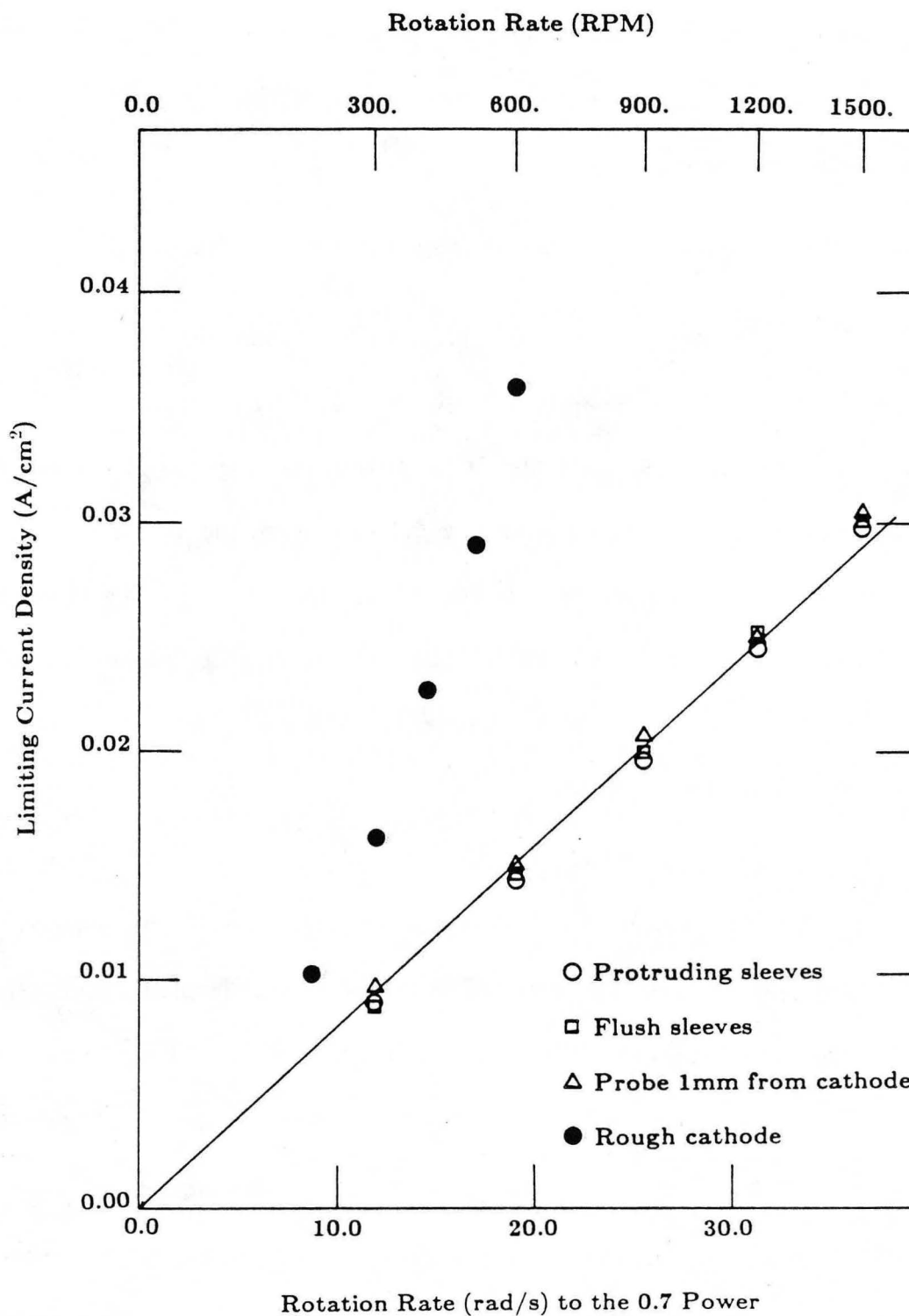
4.4.4 Effect of Reference Probe Placement and Sleeves

The measurements described in sections 4.4.3 were conducted with the reference probe placed two centimeters from the cathode surface. Measurements in the baffled cell were repeated with the probe within 1 mm of the surface and again with flush sleeves. Neither of these modifications significantly affected the limiting currents measured (figure 4-6). The reference probe was aligned to oppose
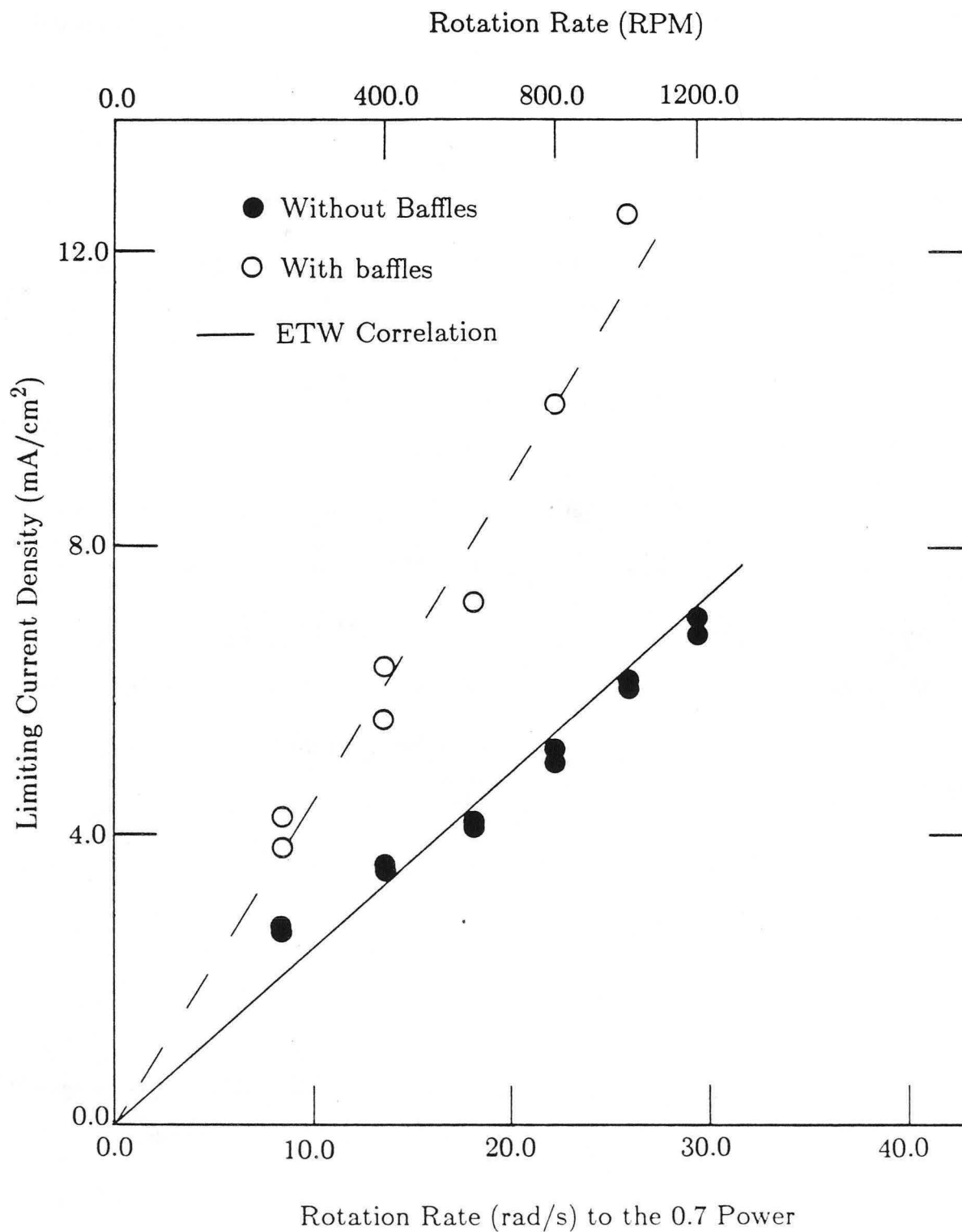
Figure 4-5: Limiting current density in the baffled RCE cell versus the Reynolds number to the 0.7 power. Electrolyte: 0.0107M [CuSO$_4$]/ 1.99M [H$_2$SO$_4$] at 20° C.

Rotation Rate (RPM)

Figure 4-6: Effects of probe placement and sleeves on limiting current density in the baffled RCE cell. Limiting current density is plotted against the 0.7 power of the Reynolds number. Electrolyte: 0.0130M [CuSO$_4$]/ 2.2M [H$_2$SO$_4$] at 18° C.

Rotation Rate (RPM)

XBL 878-3455

Figure 4-6: Effects of probe placement and sleeves on limiting current density in the baffled RCE cell. Limiting current density is plotted against the 0.7 power of the Reynolds number. Electrolyte: 0.0130M [CuSO$_4$]/ 2.2M [H$_2$SO$_4$] at 18° C.

the direction of rotation and therefore was probably close to alignment with the streamlines near the surface and could be expected to cause minimal disruption of the electrolyte motion.

4.4.5 Limiting Currents with a Dense Suspension of Inert Particles

Limiting currents from a dilute electrolyte with addition of 40 volume percent of 80 micrometer glass spheres were measured. The measurements were taken with the baffles in place and with protruding sleeves on the cathode. Again limiting currents varied with the 0.7 power of the Reynolds number (figure 4-7), but were higher by a factor of 1.3 than those for the electrolyte without spheres in the cell with baffles. The presence of glass spheres in a dense suspension is an effective transport promoter (153).

4.4.6 Effect of Cathode Texture

Limiting currents to a cathode roughened by prolonged deposition were measured to evaluate the applicability of the limiting current correlations to the conditions of the deposition studies. The substrate was formed by deposition from a 1.0M $CuSO_4$/1.0MH_2SO_4 solution at 50°, at i $=$ 1.0A/cm^2, corresponding to 40% of the limiting current to a thickness of 0.4 millimeters (figure 4-8). The surface of the electrode was then characterized by profilometry. The average overall roughness amplitude was 24 μm. The surface topography was not dendritic, but was composed of nearly hemispherical shapes a few hundred micrometers in diameter. The limiting currents on this substrate for deposition from a dilute solution were directly proportional to the Reynolds number. A

Rotation Rate (RPM)
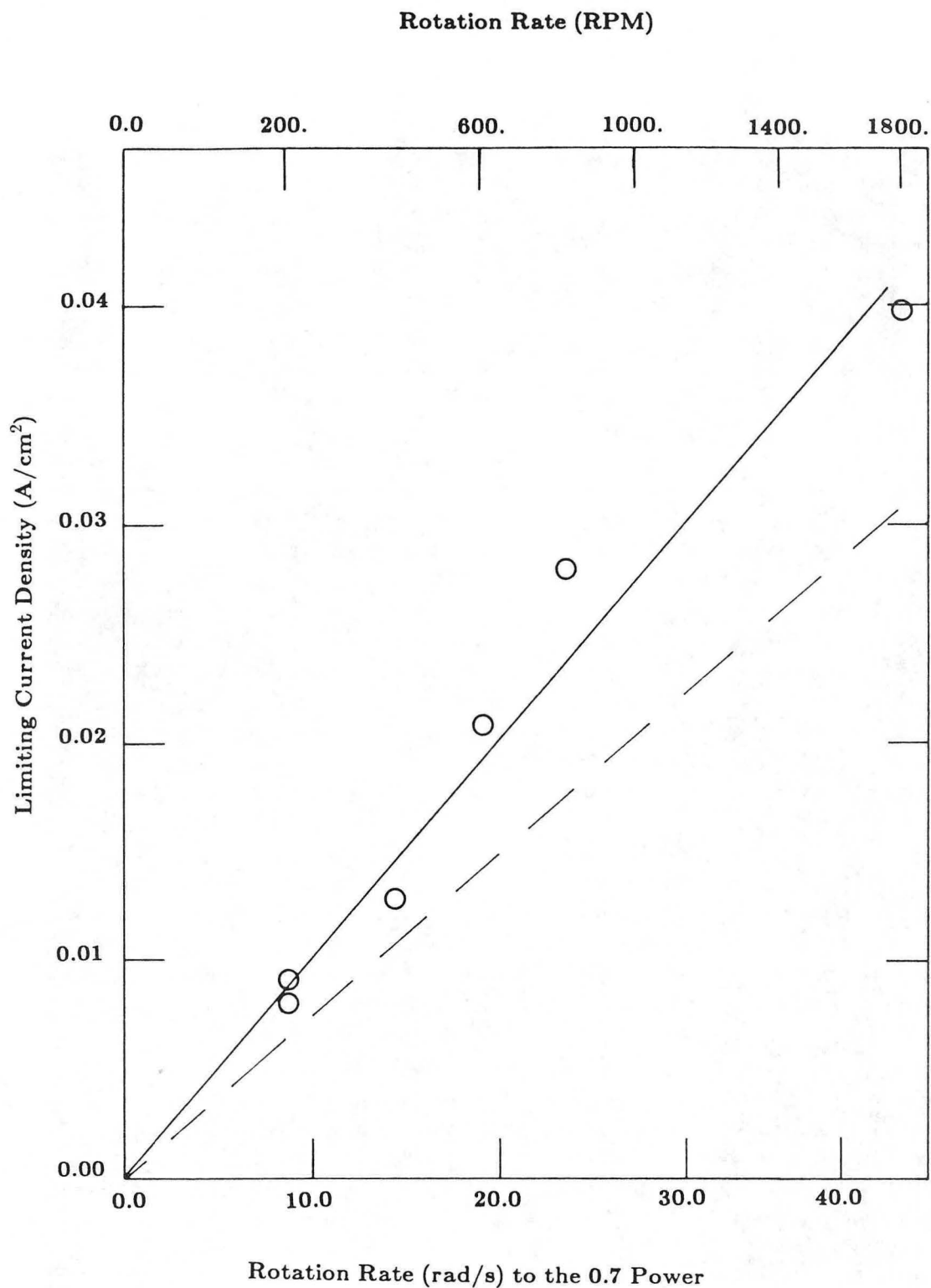
Figure 4-7: Limiting current density in a dense suspension of glass spheres (140 mesh and finer, 80 μm average diameter) in the baffled RCE cell versus the 0.7 power of the Reynolds number. Electrolyte: 0.0149M [CuSO$_4$]/ 1.6M [H$_2$SO$_4$] at 20° C.
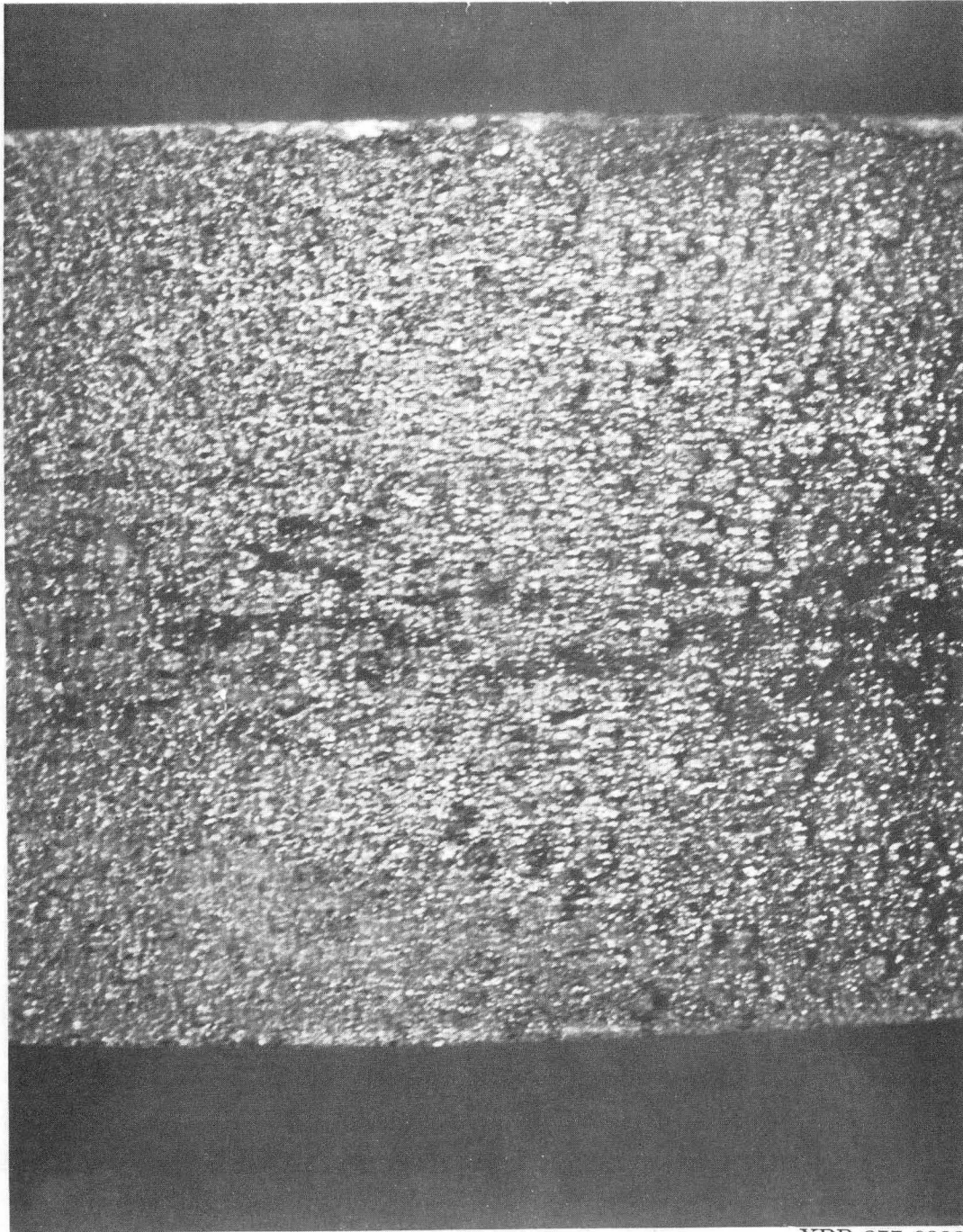
XBB 877-6093

Figure 4-8: Macrophotograph of the rough cathode surface used in limiting current measurements. Vertical dimension is 1.8 cm. Substrate prepared by copper deposition from a $1.0M[CuSO_4]/1.0M[H_2SO_4]$ solution at $50°$ C, at $i = 1.0A/cm^2$ and 40% of limiting current to 0.4 mm. Overall roughness amplitude is 24 μm.

current density enhancement of 2.5, comparable to the ratio of surface area of the roughened electrode to that of a smooth electrode was observed (figure 4-9).

Limiting currents presented in figures 4-5,6,7 and 9 are listed in table 4-3.

4.4.7 Conclusion

1) The limiting currents attained in the cell used in this study were in agreement with the Reynolds and Schmidt number dependence of the correlation of Eisenberg, Tobias and Wilke. Limiting current enhancment by a factor of two was caused by the presence of baffles in the electrolysis cell.

2) Deposition from a dense suspension of glass spheres in the baffled cell produced a further enhancement by a factor of 1.3.

3) Limiting currents to a rough surface were proportional to the Reynolds number in agreement with previous investigations.
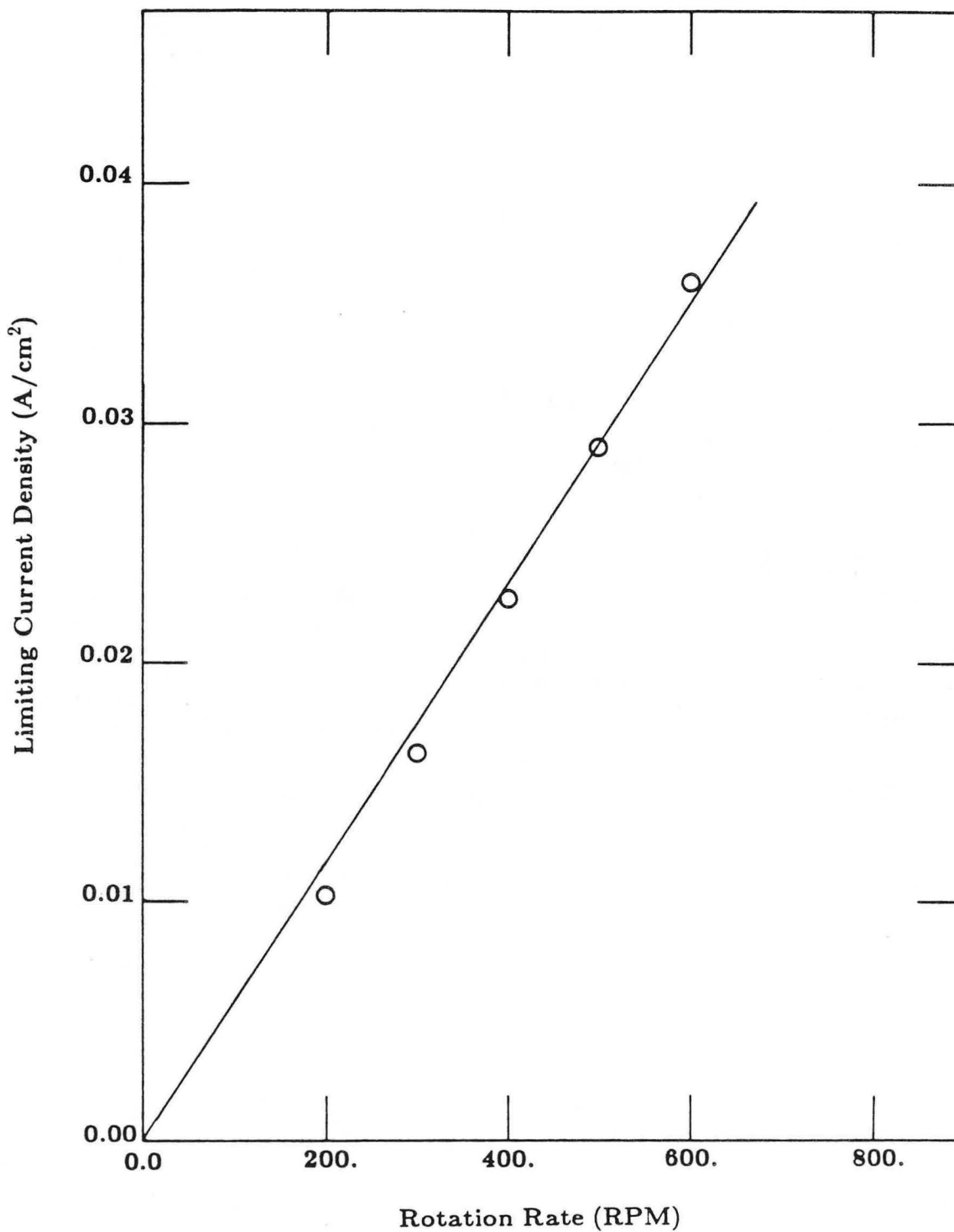
Figure 4-9: Limiting current density at a rough cylinder versus the Reynolds number. Electrolyte: $0.013M[CuSO_4]/2.4M[H_2SO_4]$ at $18°$ C. Surface Prepared by copper deposition from a $1.0M[CuSO_4]/1.0M[H_2SO_4]$ solution at $50°$ C, at $i = 1.0A/cm^2$ and 40% of limiting current to 0.4 mm. Overall roughness amplitude is 24 μm.

XBL 878-3456

Table 4-3: Limiting current densities for several cell geometries.

[CuSO$_4$] (M/l)	[H$_2$SO$_4$] (M/l)	Rotation Rate (RPM)	Limiting Current Density (mA/cm^2)	Condition
0.0107	1.99	0200.	2.83	Concentric Cylindrical Anode
		0200.	2.79	
		0400.	3.40	
		0400.	3.51	
		0600.	4.23	
		0600.	4.30	T = 20° C
		0800.	5.09	
		0800.	5.36	
		1000.	6.26	
		1000.	6.19	
		1200.	6.91	
		1200.	7.13	
		0200.	3.89	Baffles
		0200.	4.34	
		0400.	5.66	T = 20° C
		0400.	6.49	
		0600.	7.36	
		0800.	10.2	
		1000.	12.3	

Table 4-3 continued

[CuSO$_4$] (M/l)	[H$_2$SO$_4$] (M/l)	Rotation Rate (RPM)	Limiting Current Density (mA/cm^2)	Condition
0.0130	2.40	0300.	9.06	
		0600.	14.3	Baffles
		0900.	19.6	Protruding
		1200.	24.5	Sleeves
		1500.	29.8	
		0300.	9.05	
		0600.	14.7	Baffles
		0900.	20.0	
		1200.	25.3	Flush Sleeves
		1500.	30.2	
		0300.	9.81	
		0600.	15.1	Baffles
		0900.	20.7	Probe 1mm
		1200.	25.3	from Cathode
		1500.	30.2	
		0200.	10.2	Baffles
		0300.	16.2	Protruding
		0400.	22.6	Sleeves
		0500.	29.1	Rough Surface
		0600.	35.8	
0.0149	1.60	0200.	7.51	
		0200.	8.15	
		0400.	11.1	Baffles
		0600.	16.0	Protruding
		0800.	17.9	Sleeves
		1000.	23.4	With 40%
		1800.	34.8	Glass Spheres

Chapter 5: Electroforming Studies

5.1 Objective

The goal of the deposition experiments was to determine the effect of increasing the current density on surface texture development under controlled mass transfer conditions. Texture development was quantitatively compared with predictions of the stability analysis presented in chapter 2. To determine the dependence of texture development on deposition rate, the current density and fraction of limiting current were varied independently.

Deposit surface texture is a measure of the usefulness of a process for electroforming, and surface topography development during deposition profoundly affects bulk morphology. Porous or dendritic deposits, which are not useful for electroforming, pass through stages of texture development. Deposit texture in this case is a precursor to dendritic or porous morphology. Rough deposits in general have a smaller ratio of useful to total deposit mass; a smooth, compact deposit is clearly a requirement for most applications.

To provide independent measures of deposit quality, the current efficiency, density, microhardness and tensile strength were also determined. Previous reports of copper electrodeposit physical properties have been presented by Walker and Benn (154), Sard and Weil (155) and Lamb and Valentine (156,157).

5.2 Experimental Program

5.2.1 Overview

The independent variables in electroforming experiments were the current and the fraction of limiting current. The surface texture of the electroforms was quantitatively characterized by digital profilometry, which provided the amplitude and spacing of roughness elements. Some experimentation with electrolyte composition and substrate preparation was carried out first to determine the optimal conditions for the electroforming work. In section 5.2.2, these preliminary experiments are described. In section 5.2.3, the electroforming studies are reported.

5.2.2 Electrolyte Composition and Substrate Preparation

The electrolyte used in most of the electroforming experiments was a 1.0M $CuSO_4$ / 1.0M H_2SO_4 solution at 50° C. High concentration and temperature favor deposition at high current densities. Because the cell cooled to room temperature between experiments and the electrolyte was near saturation at 25° C, use of a more concentrated solution was not feasible.

Several deposits were formed from a 2.0M $CuSO_4$ solution with either no supporting electrolyte or with addition of only 0.02M H_2SO_4. The purpose was to attain very high rates of mass transfer by exploiting the high concentration and the effect of high tranference number for cupric ion in the absence of supporting electrolyte. In addition to the problem of precipitation of $CuSO_4$ at room temperature, the high resistivity of the solution made formation of thick deposits impractical.

Most of the electroforms were deposited on a mechanically polished stainless steel substrate. The steel was first sanded with 600 grit SiC paper and then polished with one micrometer diamond compound. The finished surface was smooth on a scale of less than one micrometer. A few electroforms were produced on electropolished stainless steel or copper. It was found, however, that for deposits as thick as those produced in this study, these variations in substrate had little influence on final surface topography.

5.2.3 Deposition Experiments

Independent variation of the current density and fraction of limiting current was achieved by passing a fixed current through the cell and setting the RCE rotation rate to produce the desired limiting current. The rotation rate required for a given limiting current was calculated from the correlation for limiting currents in the baffled cell, given in chapter four. The current density was varied from 0.8 to 4.0 A/cm^2, the fraction of limiting current from 0.2 to 0.8, and the charge passed from 500 to 1500 coulombs per cm^2, corresponding to deposit thicknesses of about 230 to 690 micrometers. Higher fractions of limiting current were not considered because the course and powdery deposits obtained under such conditions were judged not useful for electroforming.

5.3 Treatment of Digital Surface Profiles

The surface topography of each of the electroforms was characterized with four digital profiles taken along evenly spaced lines parallel to the axis of

rotation and centered on the RCE. Each profile was 1.048 cm in length and contained 2048 points spaced five micrometers apart. Because the electrodes were not straight to within the scale of sensitivity of the profilometer, and because the current macrodistribution was not entirely uniform, it was necessary to remove background curvature from the digital profiles. To reduce variation in statistical measures of surface roughness between the four profiles obtained from each specimen, features on a scale comparable to the total sample length were removed by a filtering procedure.

The profiles were filtered in a two step procedure. First a cubic equation was fitted to each profile by the least squares method to establish an avergage surface line. This average line was then subtracted from the profile. Next the Fourier transform of the flattened profile was used to filter out all features of spatial period greater than one quarter of the total profile length of 1.05 centimeters. The computer implemented programs for determining the transforms and filtering the profiles are given in Appendix C.

Three parameters describing the surface topography were then calculated from each filtered profile: the roughness amplitude, the fine-roughness amplitude and the roughness spatial period. The roughness amplitude was calculated by summing the absolute value of the departure of the surface height from the average surface line. This is a widely used measure of the roughness amplitude (158,159).

The spatial period of roughness was calculated from the Fourier transform of the surface profile. Fourier series representation of surface profiles has been

has been applied in optics (160) and in characterization of metal powders (161). In this study, the profile was described by a Fourier transform with both sine and cosine terms. The sum of the absolute values of the Fourier coefficients was then plotted against the corresponding wavelengths or spatial periods, and the curve was integrated to find the average value of the spatial period.

The fine-roughness amplitude is a measure of the roughness of features with spatial periods smaller than the hydrodynamic boundary layer thickness. It was assumed that the hydrodynamic boudary layer follows the contour of features of spatial period larger than its thickness (see figure 2-6). For small features the local boundary layer thickness should be different at peaks than at recesses, while for larger features it should be approximately uniform. Conditions of transport should have different effects on current distribution on surface shapes depending on which size range they are in.

The fine roughness was determined by using the Fourier transform to filter out the larger features. The hydrodynamic boundary layers in the electroforming experiments ranged from 60 to 300 micrometers in thickness. For each profile, the Fourier series was evaluated using only those terms corresponding to spatial periods greater than 80 micrometers. This synthesis was then subtracted point by point from the real profile to leave a contour as seen from a path following the larger features (figure 5-1).

A) Surface Profile

← 5 mm →
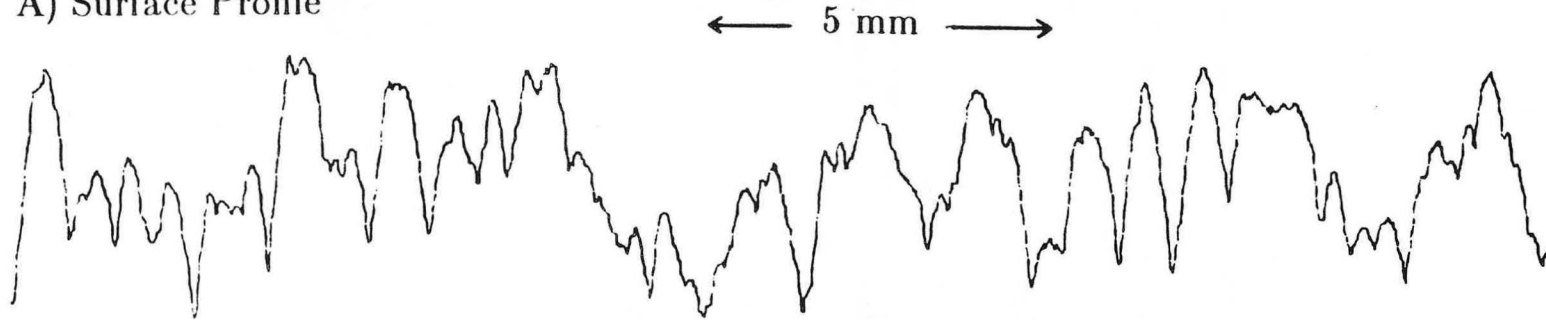
B) Fourier Synthesis

| 10 μm
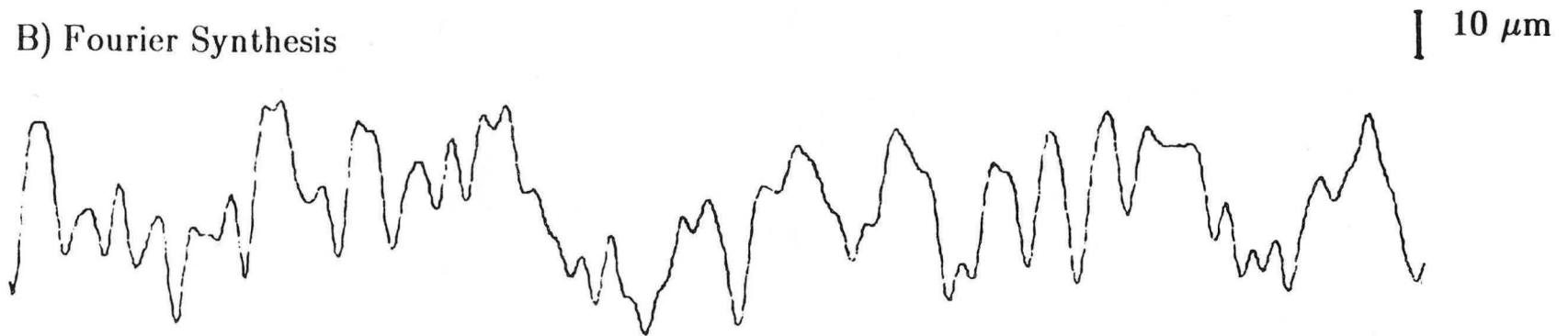
C) Fine Roughness Profile

80 μm

Figure 5-1: Determination of fine-roughness profile. The surface profile, A, is filtered with the Fourier synthesis, B, composed of terms of wavelength greater than 80 micrometers yielding the fine-roughness profile, C composed of terms of wavelength less than 80 micrometers.

XBL 877-3340

5.4 Results

5.4.1 Variation of Roughness with Fraction of Limiting Current

Roughness amplitude, fine-roughness amplitude and roughness spatial period all increased with increasing fraction of limiting current. The development of roughness with deposition time for two fractions of limiting current but the same current density can be seen qualitatively in the photographs in figures 5-2 and 5-3. The corresponding surface profiles are shown in figures 5-4 and 5-5.

Figure 5-2 shows the surfaces of three deposits, each formed at 0.8 A/ cm^2 and 20% of limiting current to 500, 1000 and 1500 coulombs per square centimeter or 230, 460 and 690 micrometers thickness. The surfaces are relatively smooth, although some roughness is apparent. Scanning electron micrographs of the deposit formed at 0.8 A/cm^2 and 20% of limiting current to 500 coulombs per square centimeter show the surface to be smooth with low amplitude, flattened hemispherical shapes (figure 5-6).

Variation of surface texture with axial position is visible in the photographs in figure 5-2. The deposits are roughest in a well defined area close to the sleeves. Curvature in the unfiltered surface profiles showed that the current density was larger by as much as 20% at the edges of the electrode than at the center because of ohmic effects (162)(see figure 3-9). In addition, the corners near the sleeves are probably subject to greater mass transport resistance than the center. These compounded effects resulted in deposition at a higher fraction of limiting current in the corners.
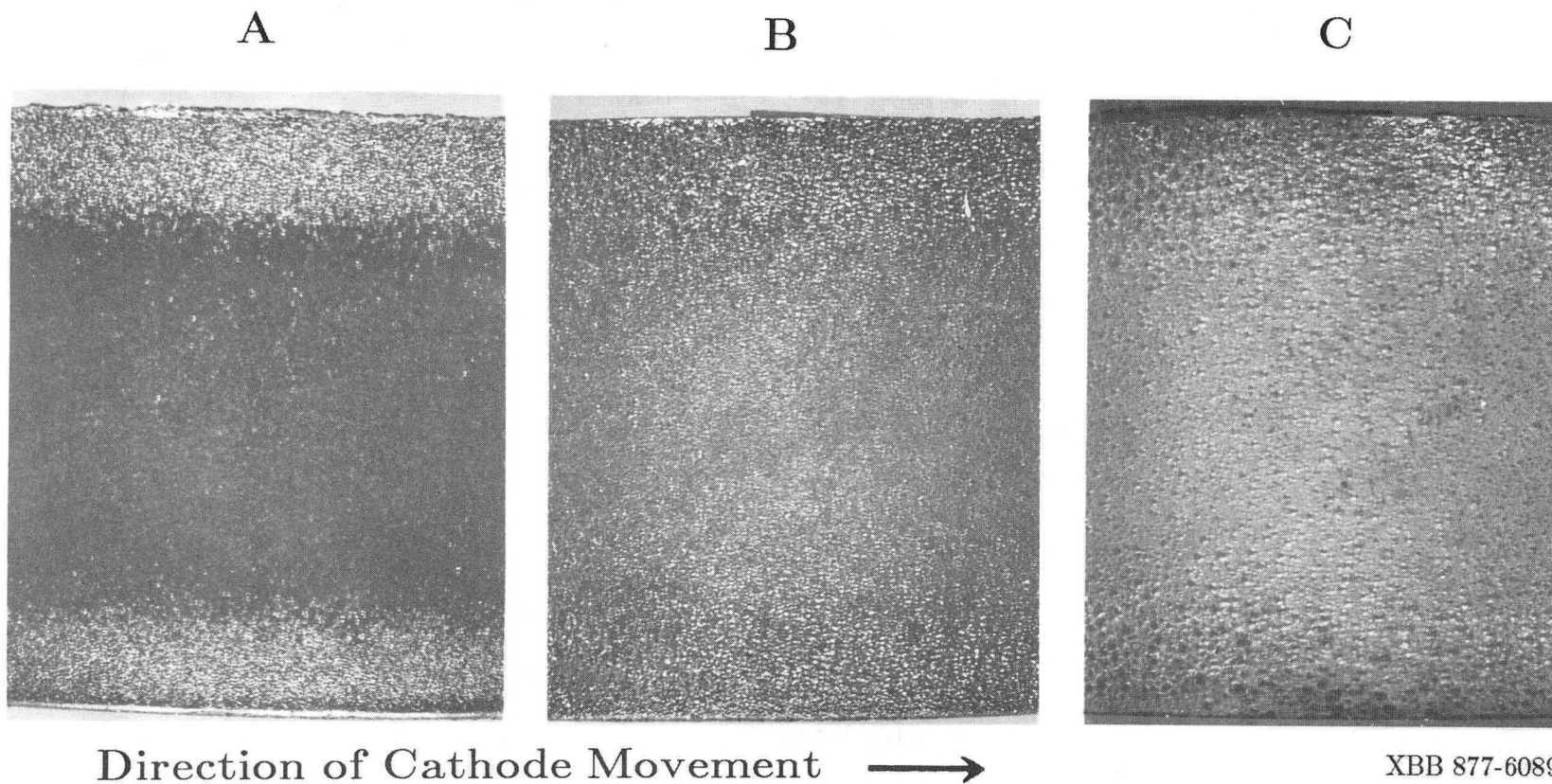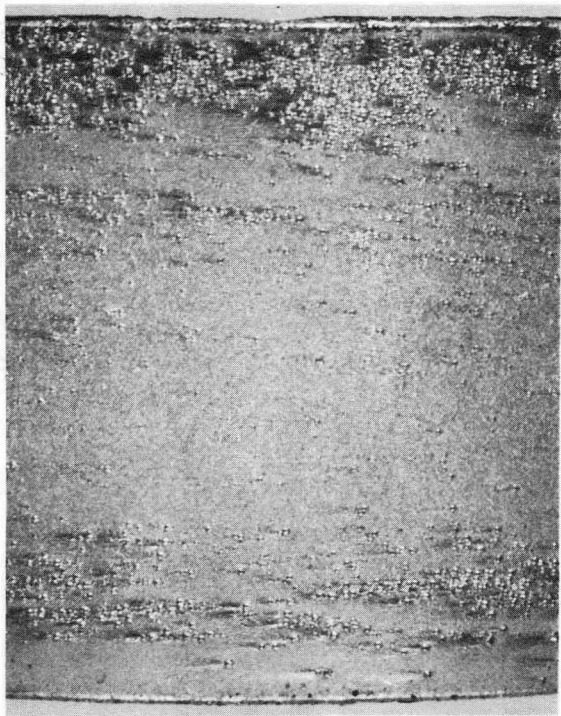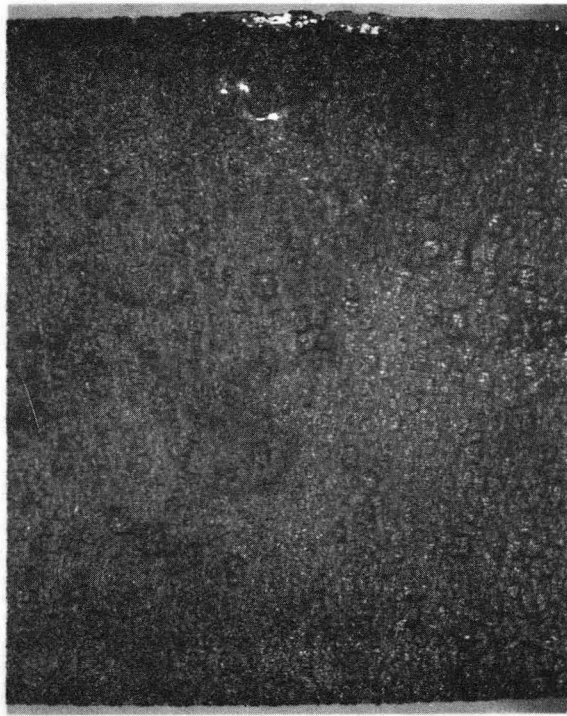
A   B   C

Direction of Cathode Movement ⟶   XBB 877-6089

Figure 5-2: Macrophotographs of electroforms produced at 0.8 A/cm^2 and 20% of limiting current. Electrolyte: 1.0 M CuSO$_4$/1.0 M H$_2$SO$_4$ at 50° C. A) 500 coulombs/cm^2, B) 1000 coulombs/cm^2, C) 1500 coulombs/cm^2. Vertical dimension is 1.8 cm.
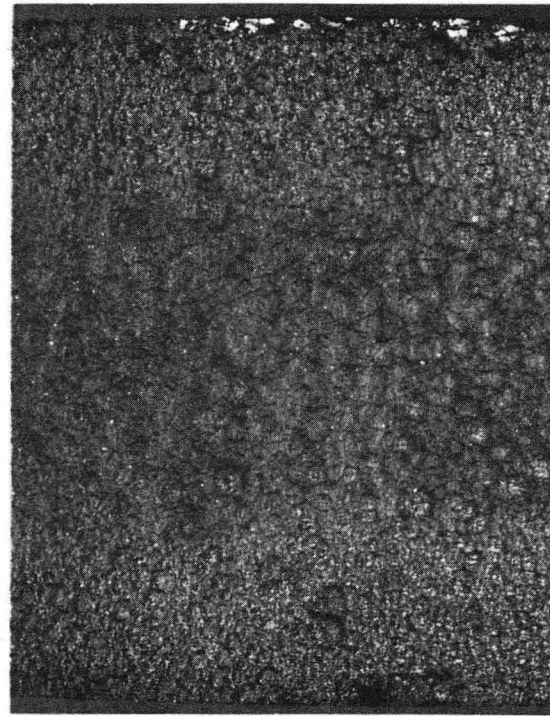
94

A   B   C

Direction of Cathode Movement ⟶

XBB 872-6092

Figure 5-3: Macrophotographs of electroforms produced at 0.8 A/cm^2 and 40% of limiting current. Electrolyte: 1.0 M CuSO$_4$/1.0 M H$_2$SO$_4$ at 50° C. A) 500 coulombs/cm^2, B) 1000 coulombs/cm^2, C) 1500 coulombs/cm^2. Vertical dimension is 1.8 cm.

Figure 5-4: Surface profiles of electroforms produced at 0.8 A/cm^2 and 20% of limiting current. Electrolyte: 1.0 M CuSO$_4$/1.0 M H$_2$SO$_4$ at 50° C.

Surface Profiles

Charge Passed (coulombs/ cm^2)

1500.

1000.

500.
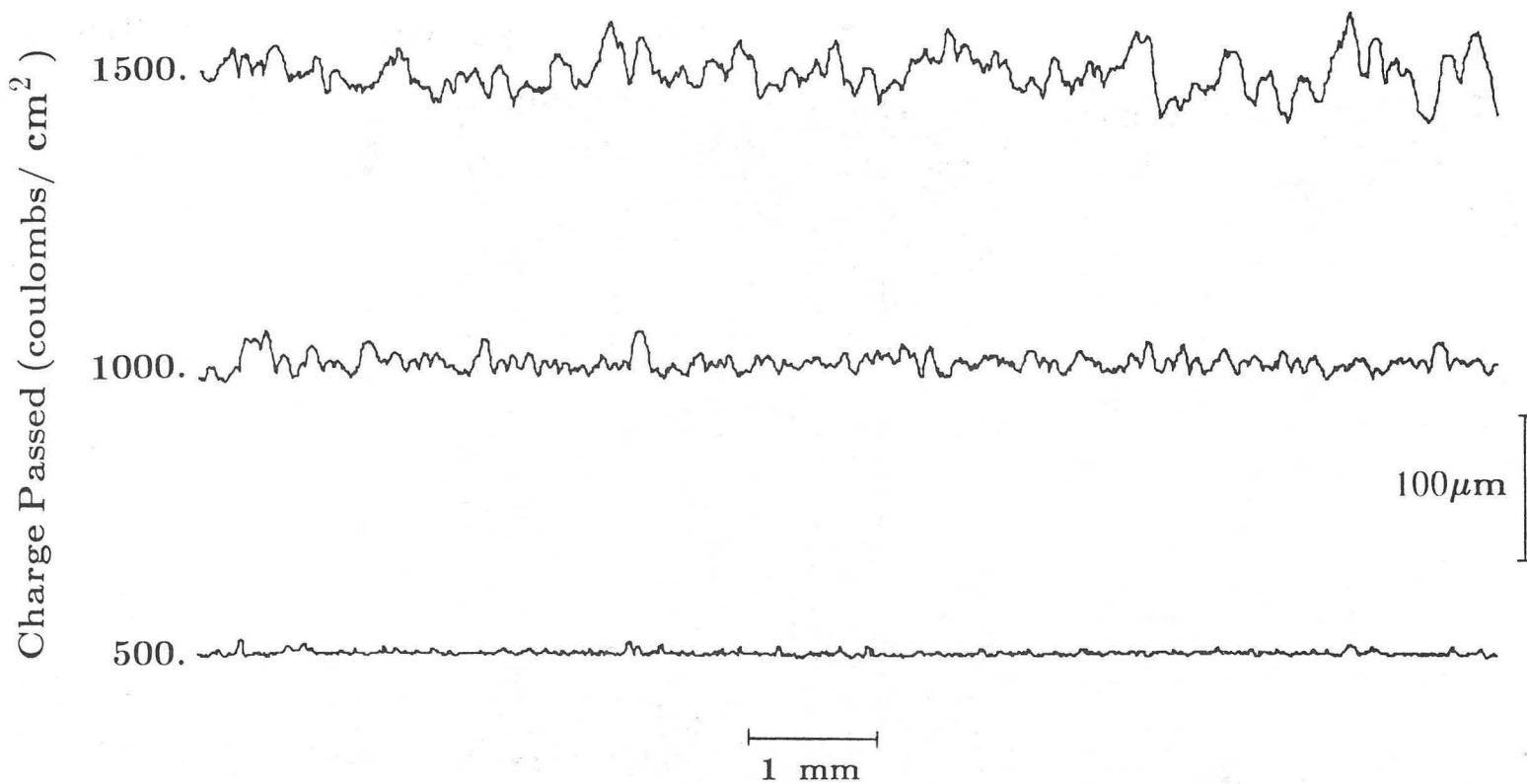
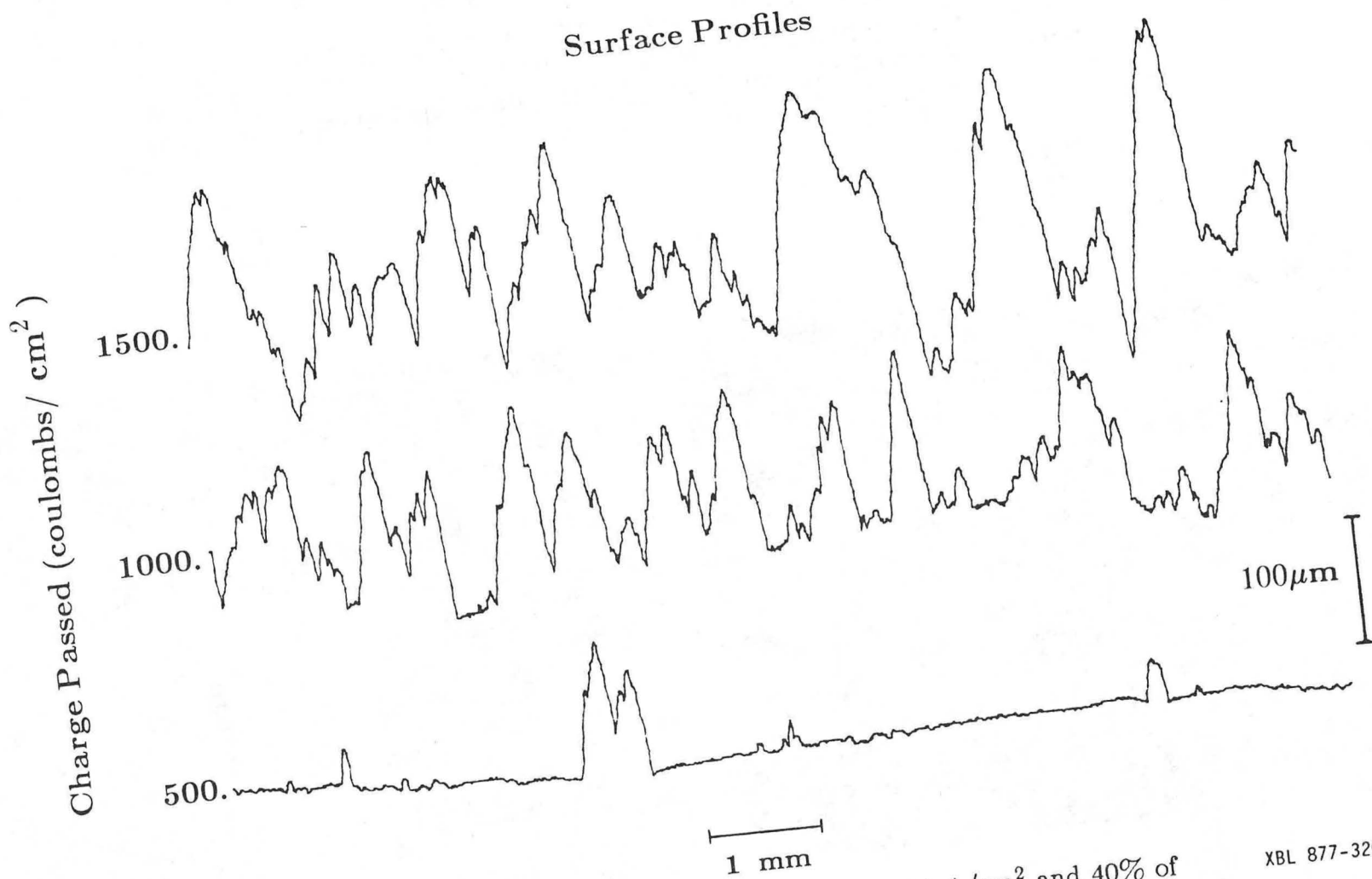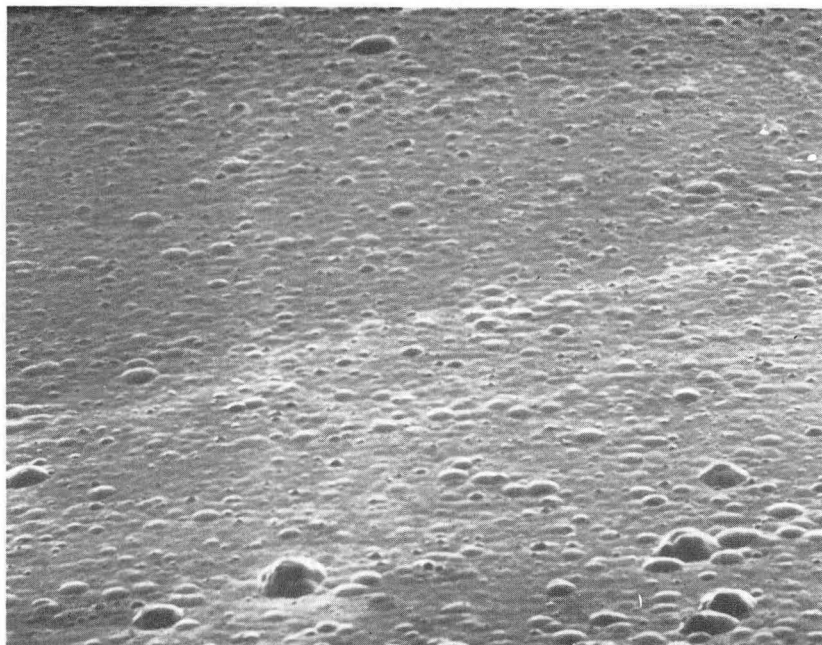100μm

1 mm

XBL 877-3267

97

Figure 5-5: Surface profiles of electroforms produced at 0.8 A/cm^2 and 40% of limiting current. Electrolyte: 1.0 M CuSO$_4$/1.0 M H$_2$SO$_4$ at 50° C.
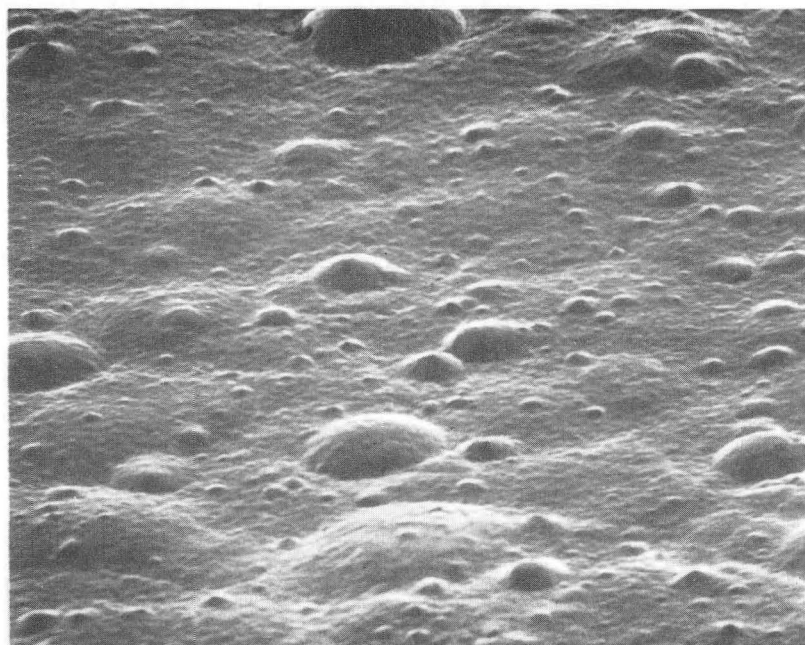
A   B

XBB 877-5628

200 μm   20 μm

Figure 5-6: Scanning electron micrographs of surface of electroform produced at 0.8 A/cm^2 and 20% of limiting current. Electrolyte: 1.0 M CuSO$_4$/1.0 M H$_2$SO$_4$ at 50° C. Charge Passed: 500 coulombs/cm^2. Tilt angle: 60 degrees.

Figure 5-3 presents a series of photographs of deposits formed at 0.8 A/ cm^2 and 40% of limiting current to thicknesses of 500, 1000 and 1500 coulombs per square centimeter respectively. Comparison with the deposits formed at 20% of limiting current shows a much higher rate of roughness development. The deposits in this case were uniformly rough and showed no axial variation. The absence of axial variation in texture may be a result of reduced influence of the sleeves at low rotation rate. To double the limiting current density the rotation rate must be increased by a factor of 2.7. The supply of power to the fluid by the sleeves was therefore much higher for the deposit formed at 20% than for that formed at 40% of limiting current.

A comparison of three deposits, each 500 coulombs/cm^2 in thickness, formed at 0.8 A/cm^2 and fractions of limiting current of 20%, 40% and 80% respectively shows the expected increase in roughness with approach to the limiting current (figures 5-7,5-8). The appearance of the deposits changes dramatically with each increment in fraction of limiting current.

The sample formed at 40% of limiting current shows a few widely spaced, large features against a relatively smooth background. This structure is similar to the copper morphologies observed by Kindler (109). The large features are evidently large, widely spaced nodules covered by fine structure. The deposit formed at 80% of limiting current was very rough and partially crumbled when it was removed from the substrate.

Both the overall roughness amplitude and the fine roughness amplitude increased with increase in fraction of limiting current (figures 5-9,5-10). The

A   B   C
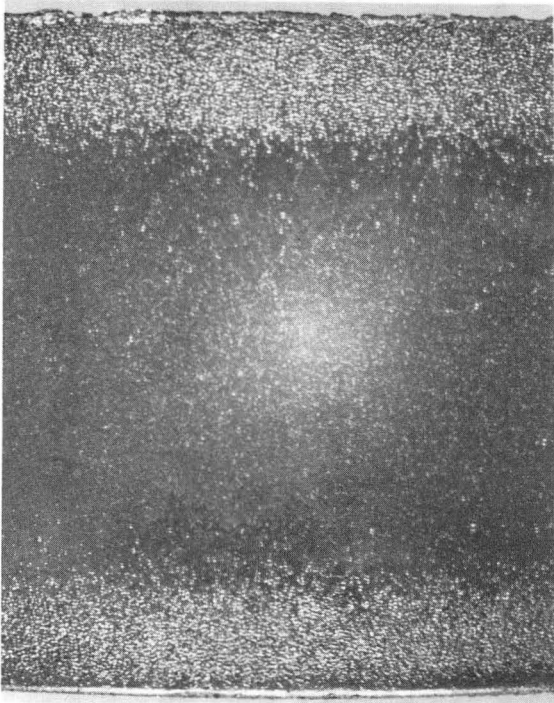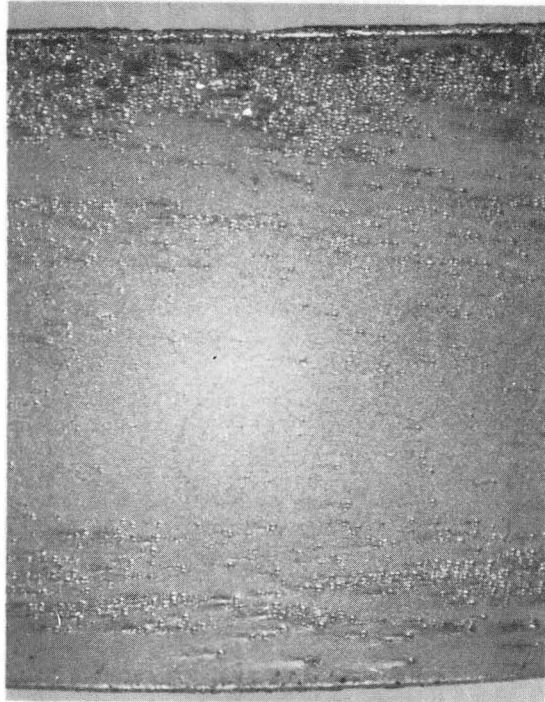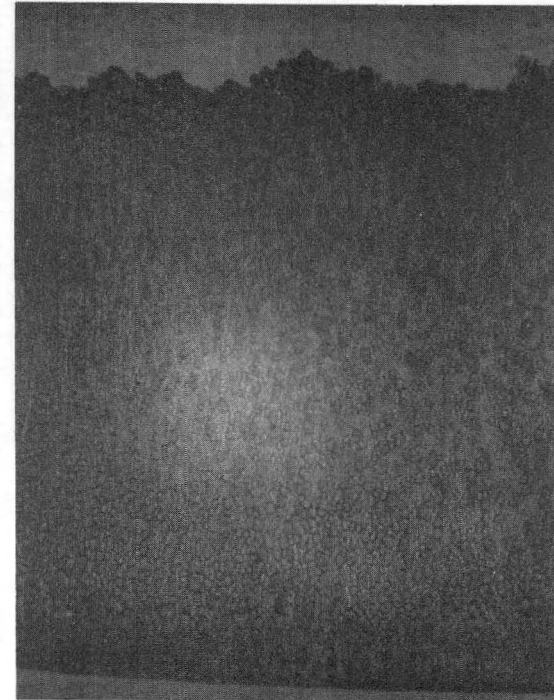
Direction of Cathode Movement ⟶

Figure 5-7: Macrophotographs of electroforms produced at 0.8 A/cm^2. Charge Passed: 500 coulombs/cm^2. Electrolyte: 1.0 M CuSO$_4$/1.0 M H$_2$SO$_4$ at 50° C. A) 20%, B) 40%, and C) 80% of limiting current. Vertical dimension is 1.8 cm.

Surface Profiles

Fraction of Limiting Current

0.8

0.4

0.2

100μm

|— 1 mm —|
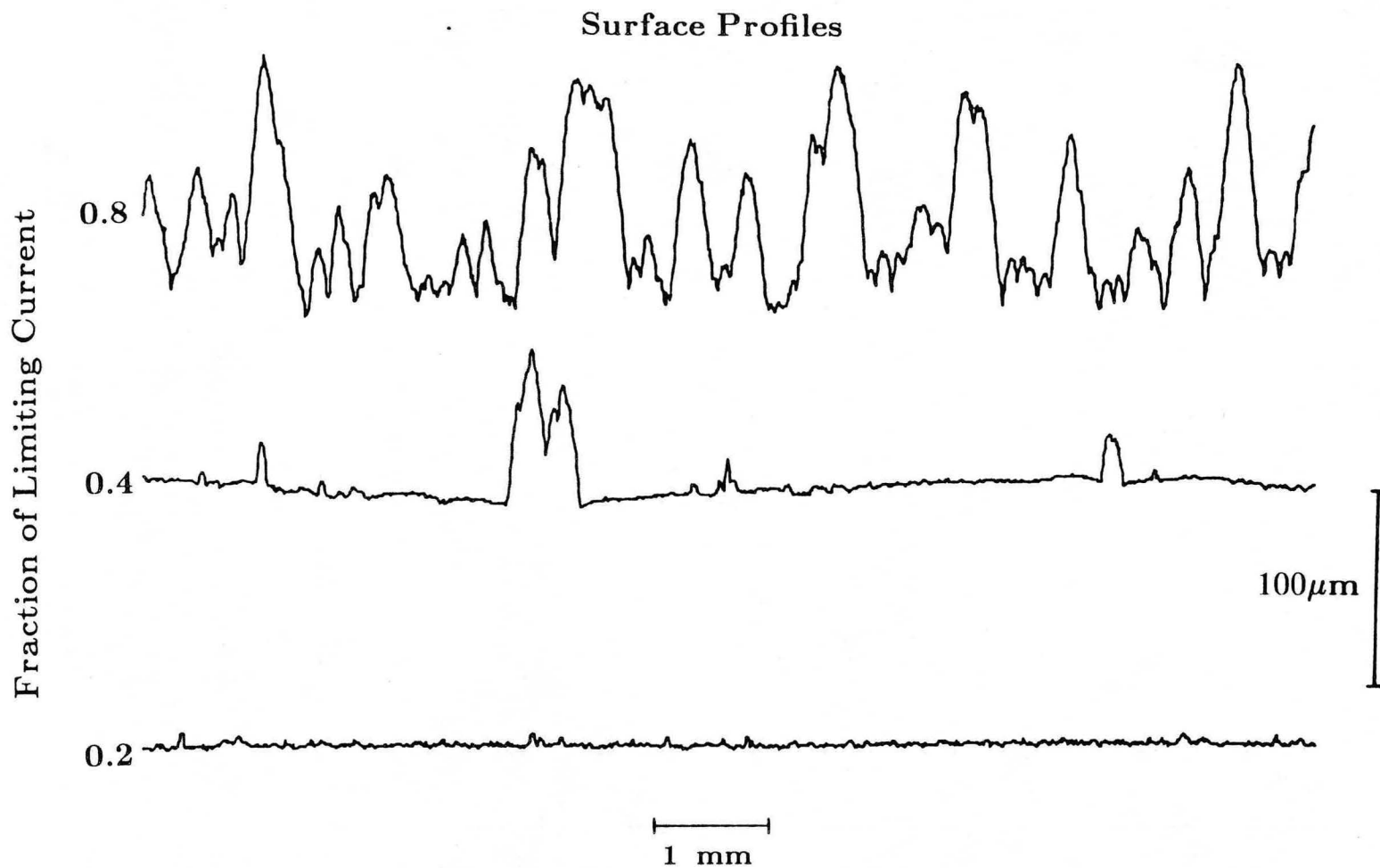
Figure 5-8: Surface profiles of electroforms produced at 0.8 A/cm^2 and 20%, 40% and 80% of limiting current. Charge Passed: 500 coulombs/cm^2. Electrolyte: 1.0 M CuSO$_4$/1.0 M H$_2$SO$_4$ at 50° C.
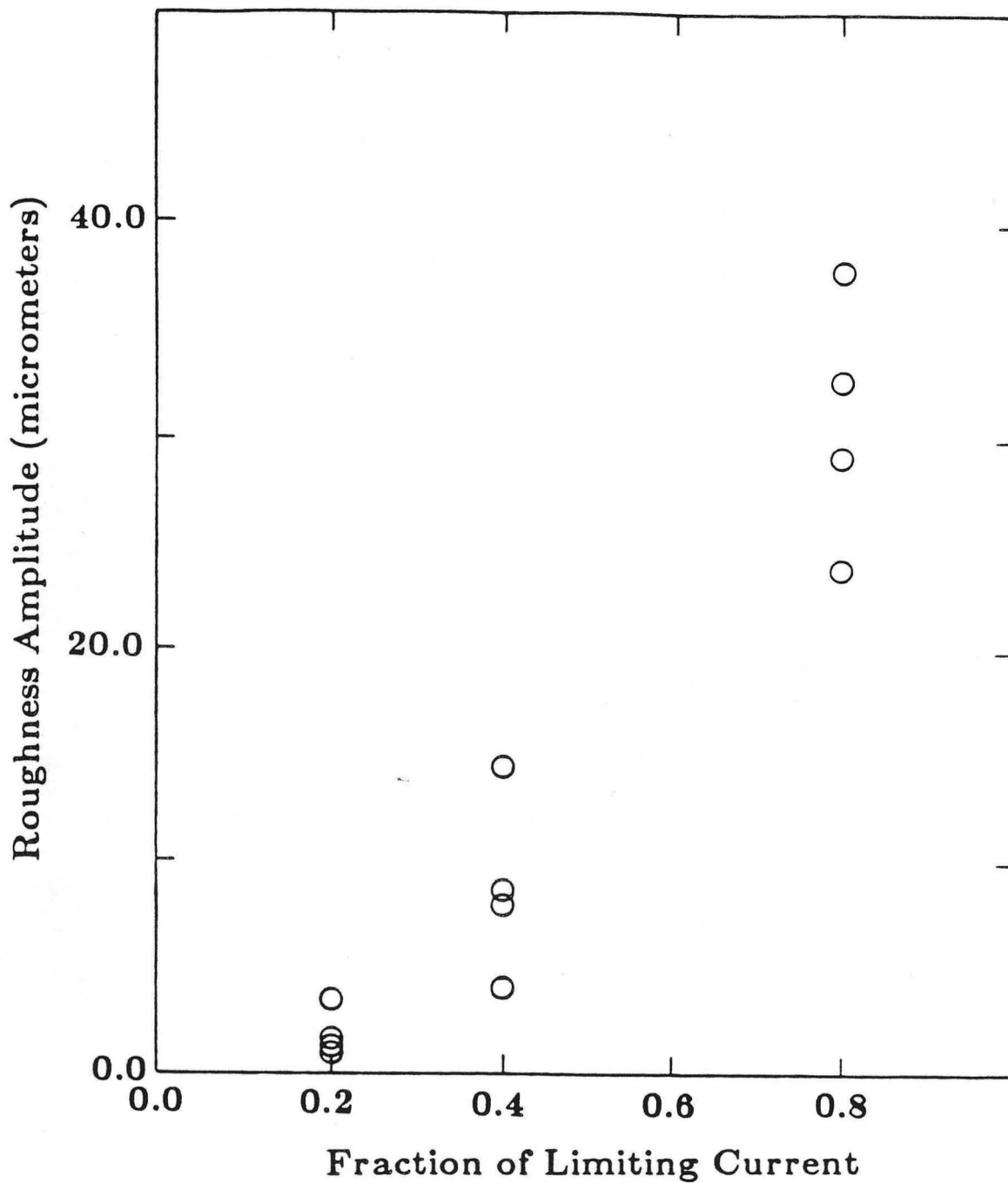
XBL 877-3270

Figure 5-9: Roughness amplitude versus fraction of limiting current for deposits formed at 0.8 A/cm^2 from a 1.0 M CuSO$_4$/1.0 M H$_2$SO$_4$ electrolyte at 50° C. Charge Passed: 500 coulombs/cm^2. The four points shown at each fraction of limiting current were calculated from four profiles taken at different positions on one deposit.
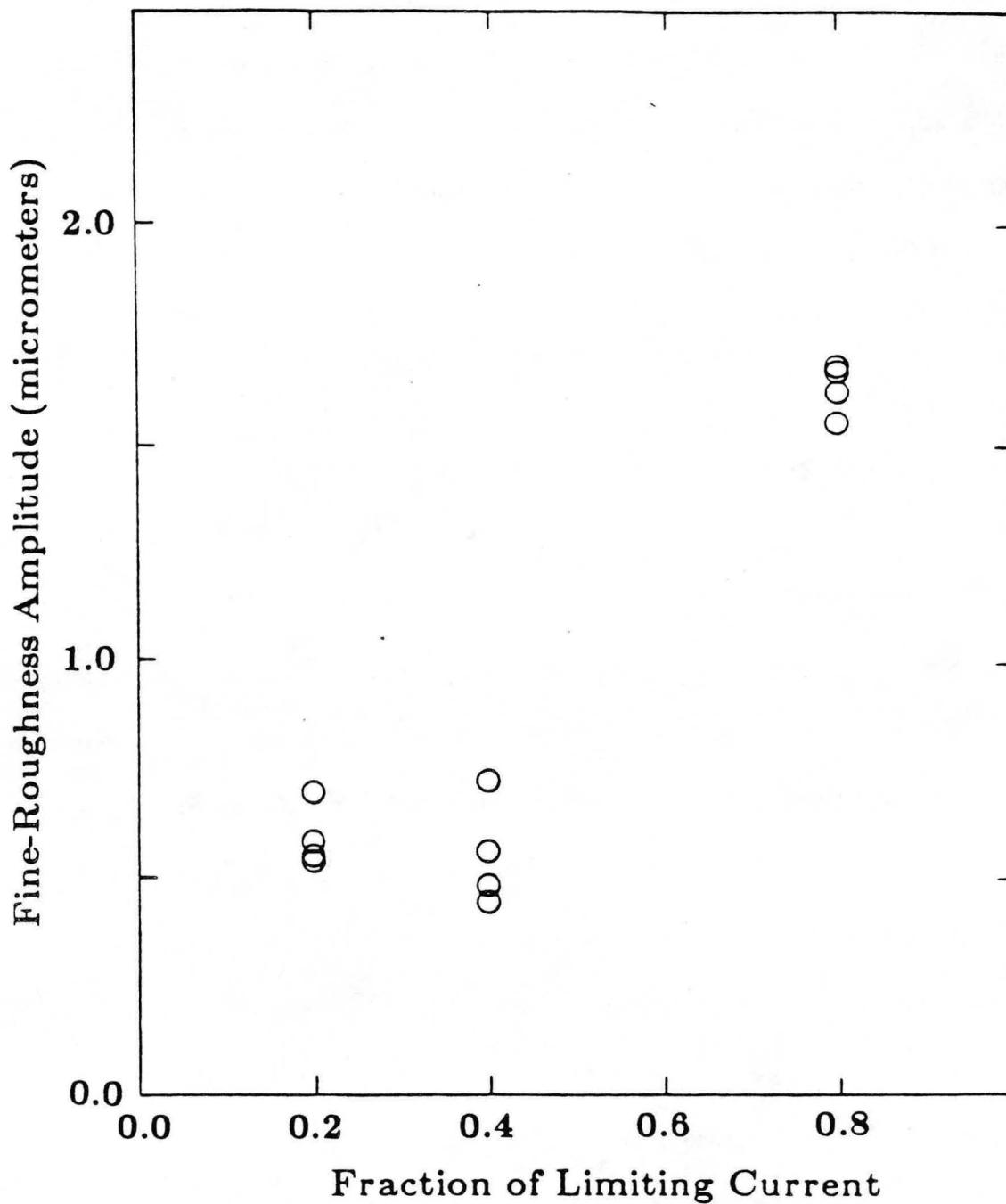
Figure 5-10: Fine-roughness amplitude versus fraction of limiting current for deposits formed at 0.8 A/cm^2 from a 1.0 M CuSO$_4$/1.0 M H$_2$SO$_4$ electrolyte at 50° C. Charge Passed: 500 coulombs/cm^2. The four points shown at each fraction of limiting current were calculated from four profiles taken at different positions on one deposit.

dependence of spatial period of roughness on fraction of limiting current is shown in figure 5-11. There is a large increase in protrusion spacing between 20% and 80% of limiting current. However, because of the contribution of large, widely spaced features, the average spatial period was a maximum for the deposit formed at 40% of limiting current.

5.4.2 Variation of Roughness with Current Density

Roughness amplitude and spatial period decreased with increasing current density for all fractions of limiting current. Fine roughness amplitude was independent of current density at constant fraction of limiting current.

Macrophotographs of deposits formed at 0.8 A/cm^2 and 1.6A/cm^2 and 40% of limiting current to 500, 1000 and 1500 coulombs/cm^2, are shown in figures 5-3 and 5-12 respectively. The deposits formed at higher current density are less rough. This can be seen most clearly from the digital profiles (figures 5-5,5-13).

A series of four deposits formed at 80% of limiting current to 500 coulombs/cm^2 and current densities of 0.8 to 4.0 A/ cm^2 is shown in figure 5-14. There is a clear trend toward smaller, more closely spaced protrusions as the current density is increased, and the deposits are progressively more compact and coherent. In the deposit formed at low current density the protrusions are larger and do not adhere to one another. This deposit is easily crumbled while the deposit formed at 4.0 A/cm^2 is a compact sheet. Etched cross sections of the deposit formed at 0.8 A/cm^2 show that the individual protrusions are separate nodules in loose contact with one another (figure 5-15).

XBL 877-3335

Fraction of Limiting Current
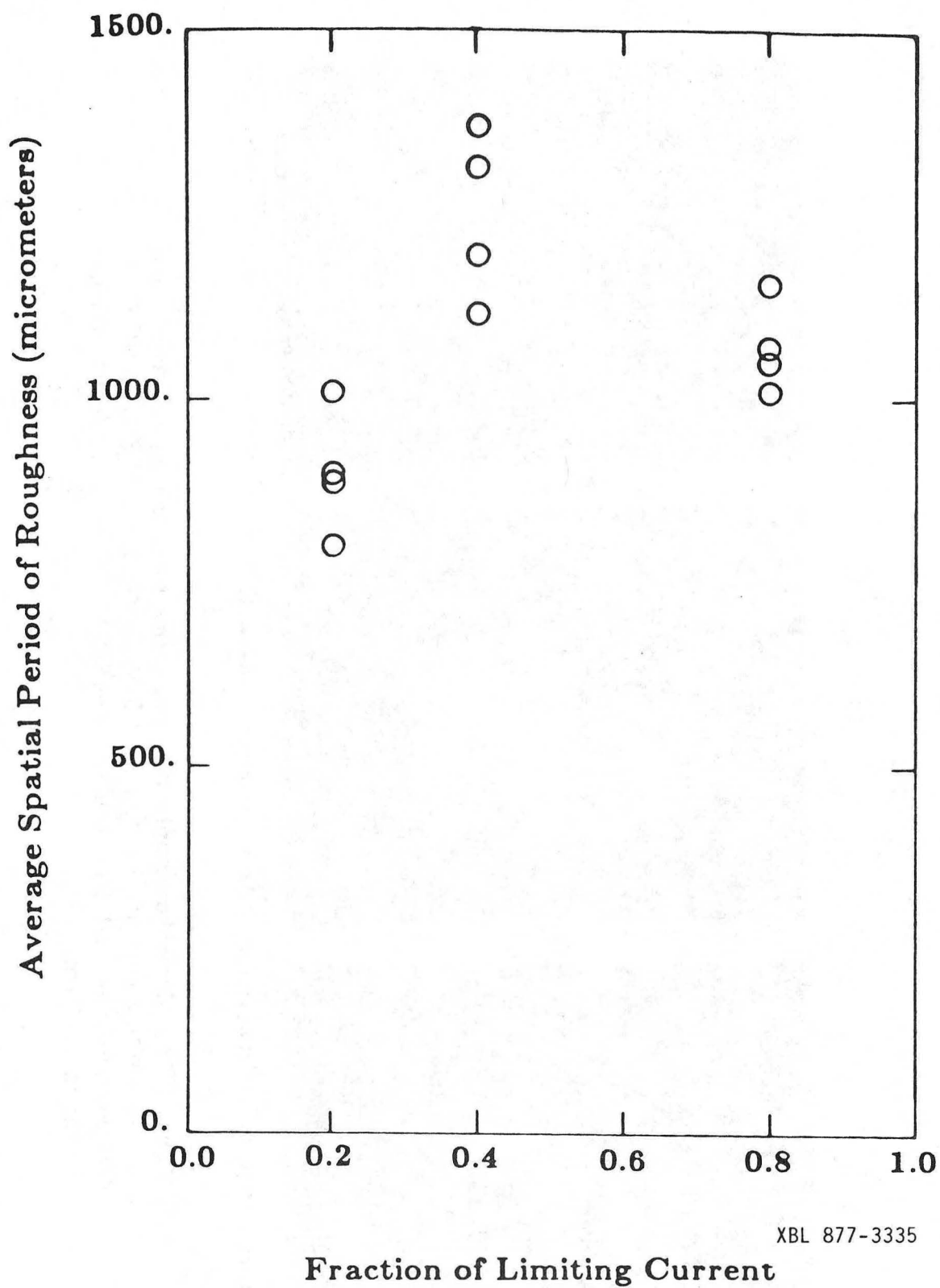
Figure 5-11: Average spatial period of roughness versus fraction of limiting current for deposition from a 1.0 M $CuSO_4$/1.0 M H_2SO_4 electrolyte at 50° C at 0.8 A/cm². Charge Passed: 500 coulombs/cm².

A   B   C
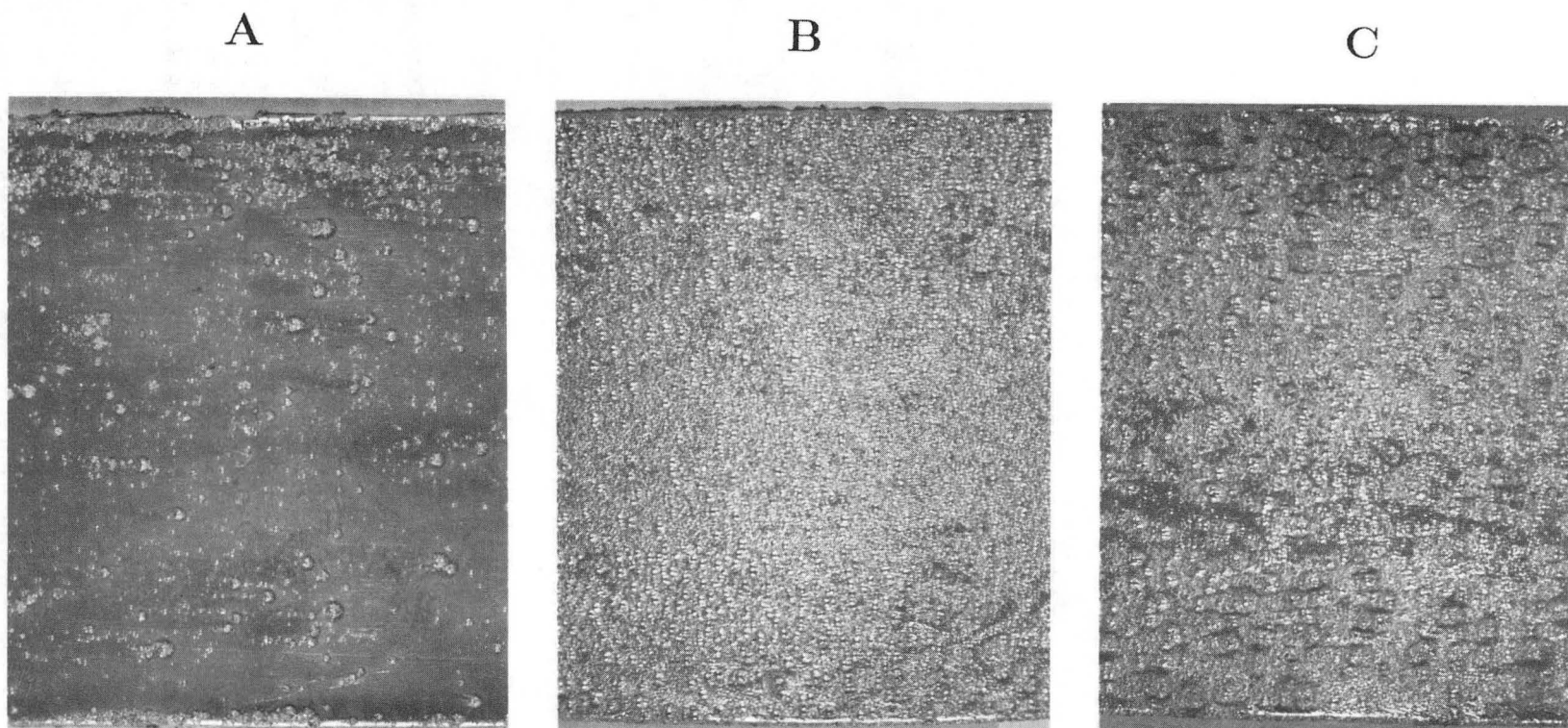
Direction of Cathode Movement ⟶

Figure 5-12: Macrophotographs of electroforms produced at 1.6 A/cm^2 and 40% of limiting current. Electrolyte: 1.0 M $CuSO_4$/1.0 M H_2SO_4 at 50° C. A) 500 coulombs/cm^2. B) 1000 coulombs/cm^2. C) 1500 coulombs/cm^2. Vertical dimension is 1.8 cm.
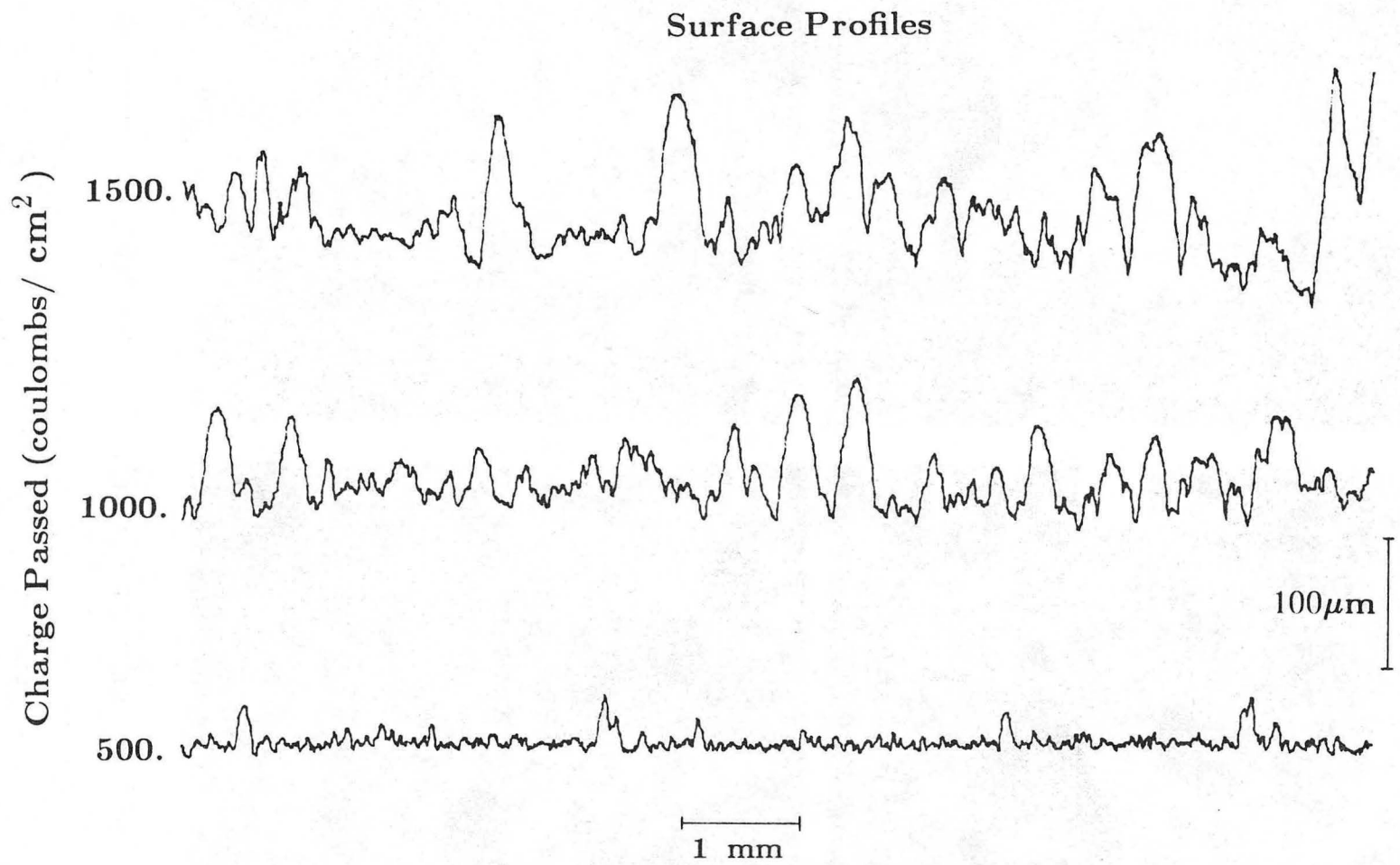
Surface Profiles

Figure 5-13: Surface profiles of electroforms produced at 1.6 A/cm^2 and 40% of limiting current. Electrolyte: 1.0 M CuSO$_4$/1.0 M H$_2$SO$_4$ at 50° C.
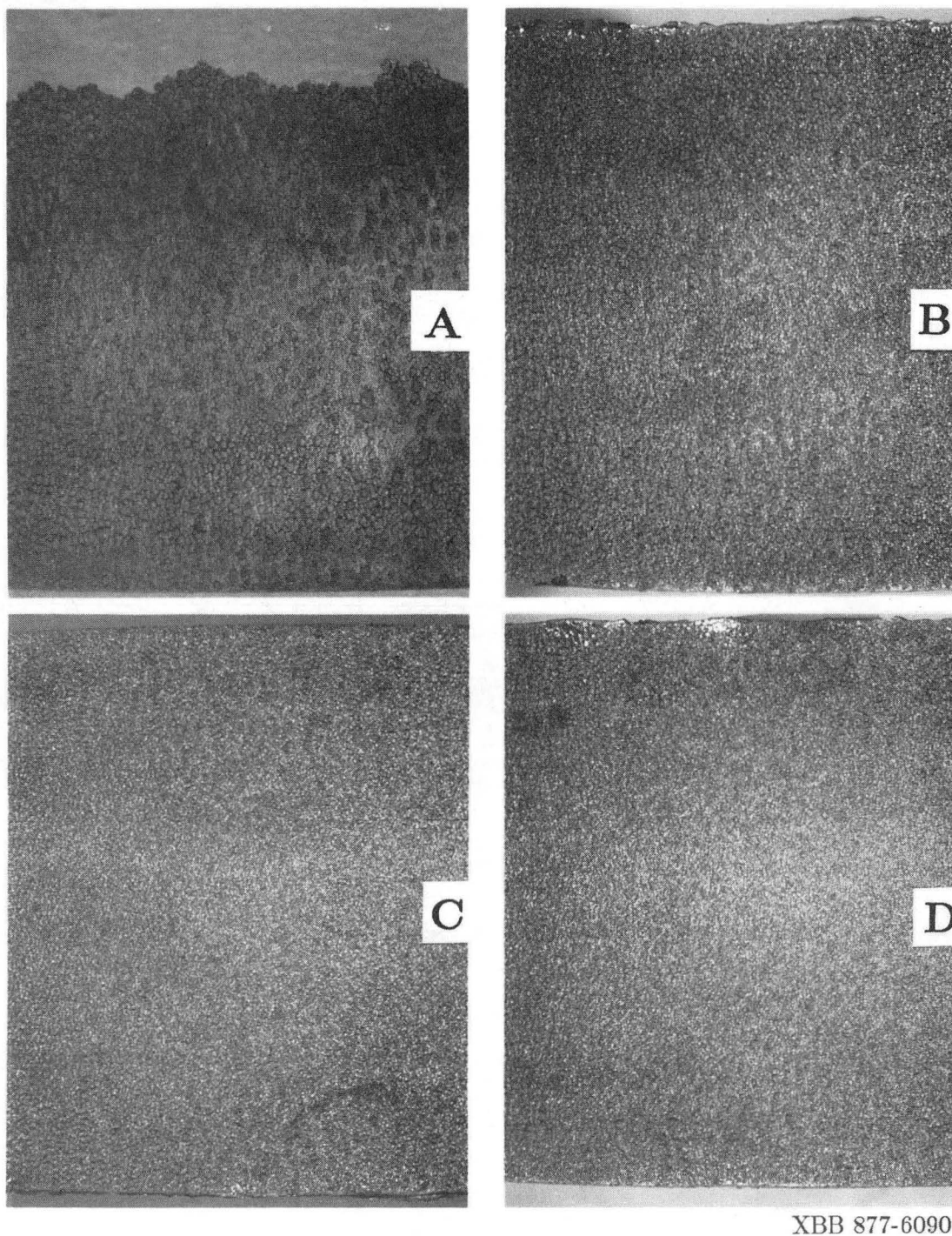
Figure 5-14: Macrophotographs of electroforms produced at 80% of limiting current. Charge Passed: 500 coulombs/cm^2. Electrolyte: 1.0 M CuSO$_4$/1.0 M H$_2$SO$_4$ at 50° C. A) 0.8, B) 1.6, C) 3.2 and D) 4.0 A/cm^2. Vertical dimension is 1.8 cm.
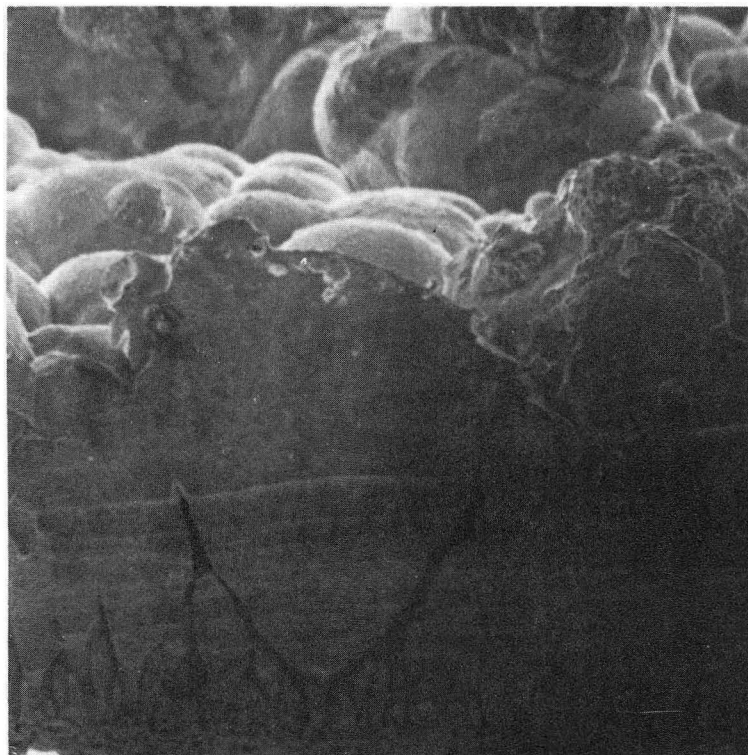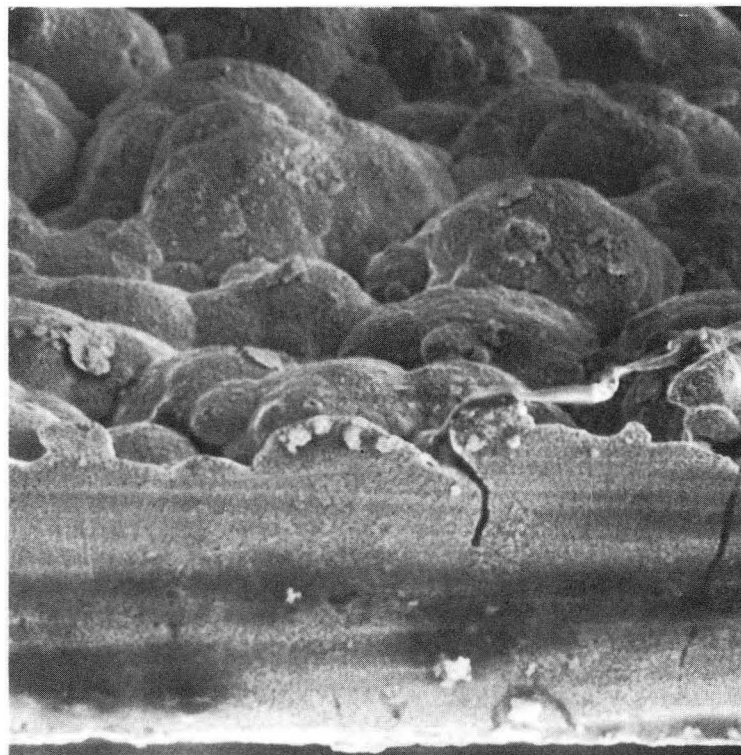
XBB 877-5636

$\overline{40\,\mu\mathrm{m}}$

Figure 5-15: Scanning electron micrographs of etched cross sections of electroforms produced at 80% of limiting current from a 1.0 M $CuSO_4$/1.0 M H_2SO_4 electrolyte at 50° C. Charge Passed: 500 coulombs/cm². A) 0.8 A/cm², B) 4.0 A/cm². Tilt angle: 80 degrees.

The decrease in both amplitude and spatial period of roughness is visible in the profiles (figure 5-16). Plots of the amplitude and spatial period versus current density show a decrease with increasing current density (figures 5-17,5-18). The fine roughness amplitude, however, is independent of current density (5-19). The scale of the fine roughness is about two micrometers, which is slightly smaller than the Nernst layer thickness of three to sixteen micrometers, and it therefore lies entirely within the average mass transfer boundary layer.

5.4.4 Physical properties

Densities, tensile strengths and hardnesses of the deposits are given in table 5-1. Also included are the current efficiencies calculated from the deposit weights. All of the deposits were formed with at least 98% current efficiency. The densities, with two exceptions, were that of non-porous copper to within the measurement error of two percent.

5.4.5 Summary of Experimental Results

The amplitude of surface roughness increases with increasing fraction of limiting current and decreases with increasing current density. The fine-roughness amplitude increases with increasing fraction of limiting current and is independent of current density. The spatial period of roughness increases with increasing fraction of limiting current and decreases with increasing current density. Values of the measured roughness parameters are presented in table 5-2.

Surface Profiles
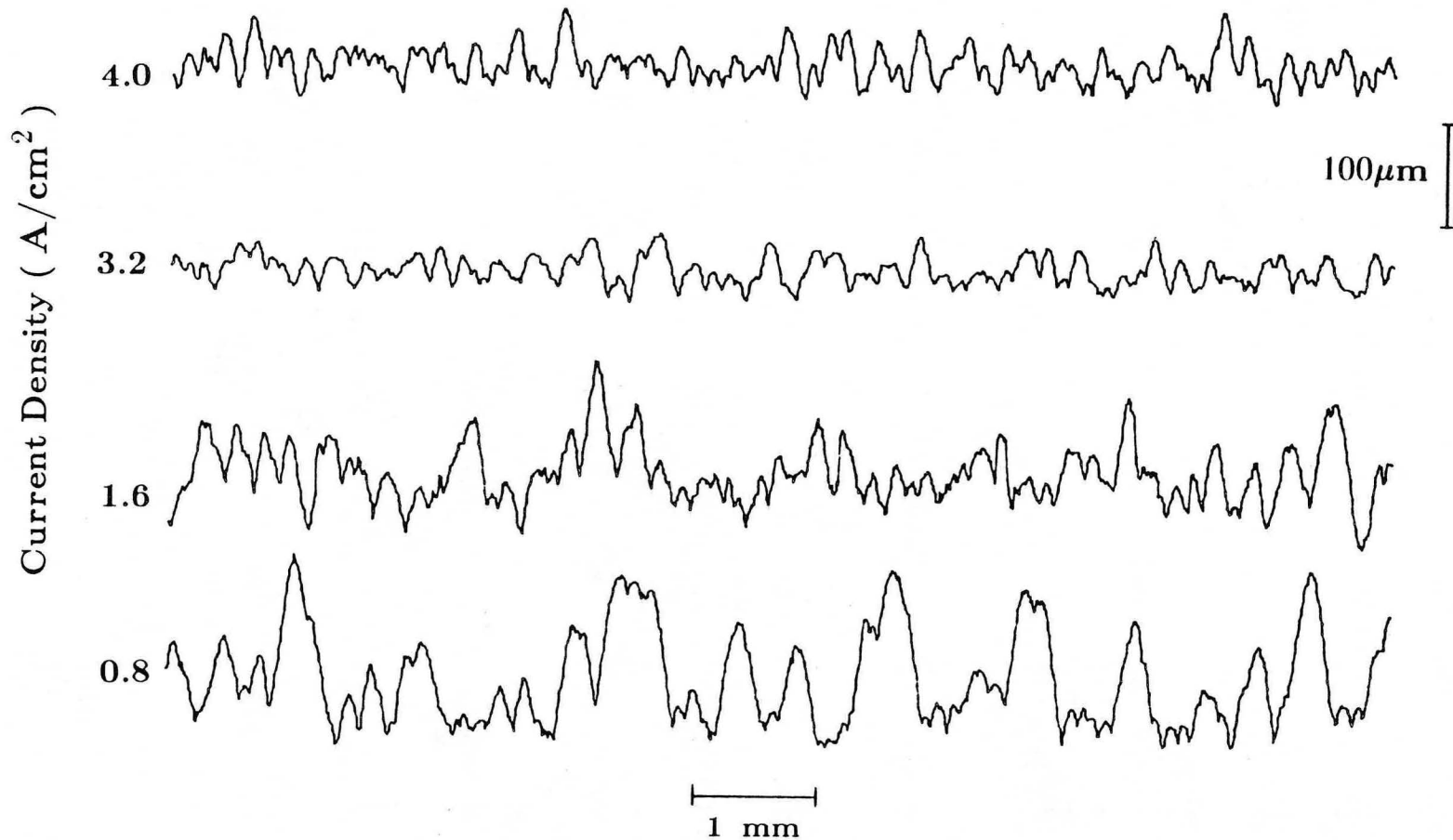
Figure 5-16: Surface profiles of electroforms produced at 80% of limiting current and 0.8, 1.6, 3.2, and 4.0 A/cm^2. Charge Passed: 500 coulombs/cm^2. Electrolyte: 1.0 M $CuSO_4$/1.0 M H_2SO_4 at 50° C.

XBL 877-3266
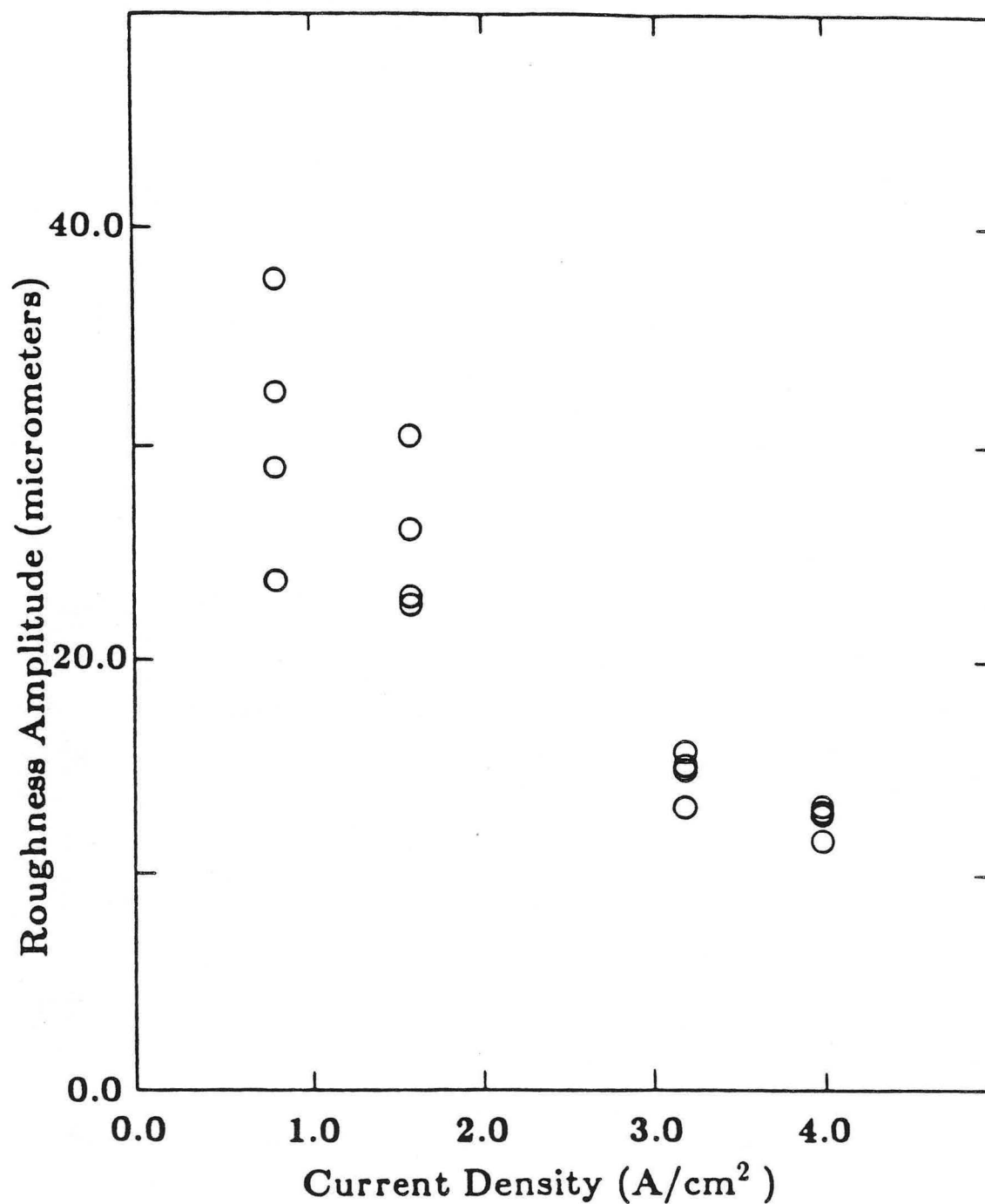
XBL 877-3262

Figure 5-17: Roughness amplitude versus current density for deposits formed at 80% of limiting current from a 1.0M $CuSO_4$/1.0 M H_2SO_4 electrolyte at 50° C. Charge Passed: 500 coulombs/cm^2. The four points shown at each fraction of limiting current were calculated from four profiles taken at different positions on one deposit.
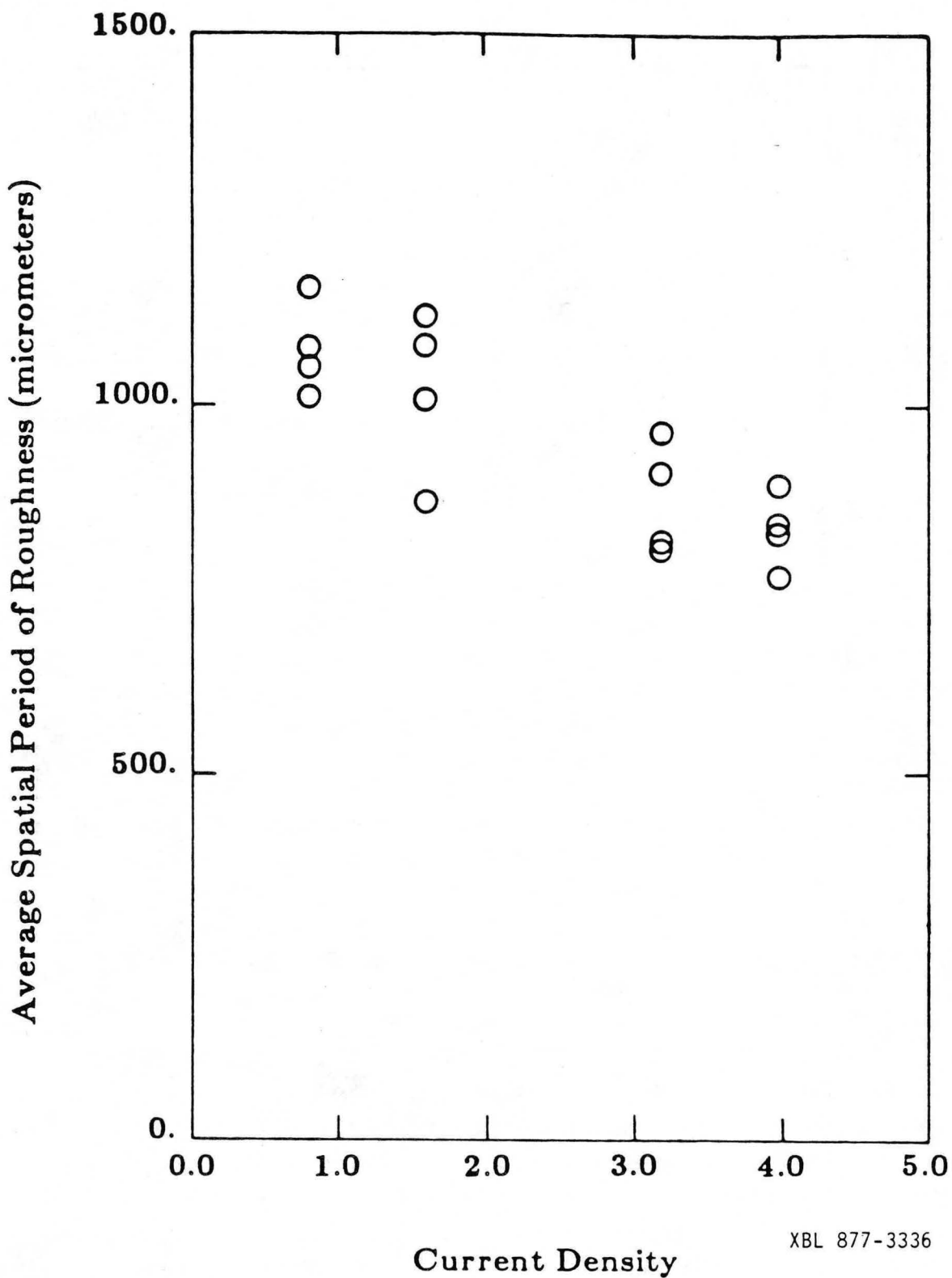
Figure 5-18: Average spatial period of roughness versus current density for deposits formed at 80% of limiting current from a 1.0 M $CuSO_4$/1.0 M H_2SO_4 electrolyte at 50° C. Charge Passed: 500 coulombs/cm^2.

XBL 877-3336
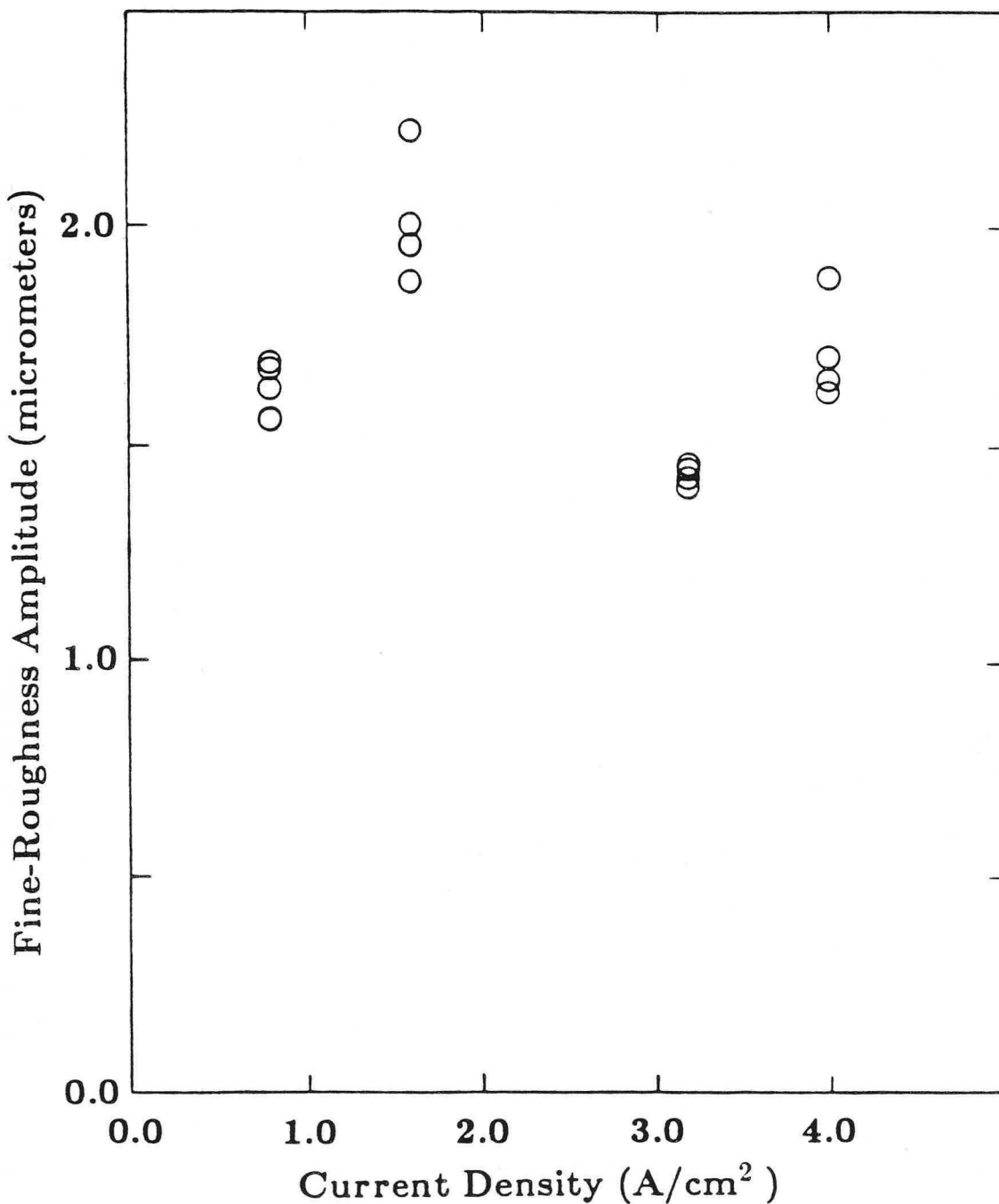
XBL 877-3263

Figure 5-19: Fine-roughness amplitude versus current density for deposits formed at 80% of limiting current from a 1.0 M $CuSO_4$/1.0 M H_2SO_4 electrolyte at 50° C. Charge Passed: 500 coulombs/cm^2. The four points shown at each current density were calculated from four profiles taken at different positions on one deposit.

Table 5-1: Physical properties of copper electrodeposits formed from a 1.0M$CuSO_4$/1.0M H_2SO_4 electrolyte at 50° C.

Current Density (A/cm^2)	Fraction of Limiting Current	Charge Passed (Coul/cm^2)	Vickers Microhardness Number (50g load)	Density (g/cm^3)	Tensile Strength (kg/mm^2)	Current Efficiency (percent)
0.8	0.2	0500.	146	9.27	25.2	103
0.8	0.2	1000.	157	8.91	47.5	100
0.8	0.2	1500.	141	8.62	42.8	100
3.2	0.8	0500.	166	8.83	24.6	101
3.2	0.8	1000.	ooo	0.00	19.4	101
1.6	0.4	0500.	144	8.98	oo.o	100
1.6	0.4	1000.	130	8.99	25.8	101
1.6	0.4	1500.	143	8.95	25.4	100
0.8	0.4	0500.	127	9.01	38.2	100
0.8	0.4	1000.	150	8.90	44.9	101
0.8	0.4	1500.	150	8.78	37.2	101
1.6	0.8	0500.	118	8.81	oo.o	101
0.8	0.8	0500.	169	8.78	oo.o	101
4.0	0.8	0500.	089	8.87	18.4	101

Table 5-2: Surface roughness parameters of copper electrodeposits formed from a 1.0MCuSO$_4$/1.0M H$_2$SO$_4$ electrolyte at 50° C.

Current Density (A/cm^2)	Fraction of Limiting Current	Charge Passed (Coul/cm^2)	Amplitude of Overall Roughness (micrometers)	Amplitude of Fine Roughness (micrometers)	Spatial Period of Roughness (micrometers)
0.8	0.2	0500.	3.54	0.70	1050.
			1.26	0.59	0880.
			1.64	0.56	0800.
			1.19	0.55	0890.
0.8	0.2	1000.	6.66	1.31	0915.
			8.86	1.44	0990.
			5.72	1.08	0880.
			4.96	1.01	0800.
0.8	0.2	1500.	8.08	1.13	0970.
			9.86	1.23	1130.
			13.2	1.24	1150.
			10.6	1.27	0990.
0.8	0.4	0500.	8.03	0.49	1200.
			8.71	0.57	1370.
			4.15	0.45	1120.
			14.5	0.73	1320.
0.8	0.4	1000.	33.4	1.61	1180.
			33.3	1.68	1410.
			39.0	1.56	1190.
			41.8	1.64	1290.
0.8	0.4	1500.	34.7	1.93	1320.
			53.3	2.13	1470.
			36.4	2.12	1150.
			47.7	1.82	1300.
0.8	0.8	0500.	32.8	1.56	1010.
			29.2	1.68	1080.

Table 5-2 (Continued)

Current Density (A/cm²)	Fraction of Limiting Current	Charge Passed (Coul/cm²)	Amplitude of Overall Roughness (micrometers)	Amplitude of Fine Roughness (micrometers)	Spatial Period of Roughness (micrometers)
			37.9	1.63	1160.
			23.9	1.69	1050.
1.6	0.4	0500.	3.99	1.48	1030.
			4.48	1.42	0930.
			6.35	1.31	0990.
			4.47	1.32	0830.
1.6	0.4	1000.	14.4	1.49	1190.
			18.1	1.61	0960.
			13.4	1.56	0890.
			17.1	1.50	0980.
1.6	0.4	1500.	23.6	1.55	1030.
			25.7	1.74	1250.
			42.3	1.59	1420.
			41.4	1.81	1270.
1.6	0.8	0500.	30.7	1.88	1050.
			23.1	2.01	1120.
			22.8	2.22	0870.
			26.3	1.96	1080.
3.2	0.8	0500.	15.1	1.45	0820.
			15.9	1.45	0820.
			15.1	1.43	0930.
			13.2	1.41	0960.
4.0	0.8	0500.	12.8	1.89	0830.
			13.1	1.71	0830.
			13.4	1.66	0900.
			11.9	1.63	0780.

5.5 Discussion

5.5.1 Comparison with Stability Analysis

The stability analysis presented in chapter two correctly predicts the trends in roughness spatial period with both current density and fraction of limiting current. Landau's theory correctly predicts the former but not the latter. The average spatial periods calculated from the three theories for the same conditions of deposition as used in the electroforming experiments are shown in figures 5-20 and 5-21. The values in figures 5-20 and 5-21 were calculated by finding the growth rates for perturbations equal to the same harmonics of the profile lengths that were used to treat the real data. Comparison with the experimental results indicates that while the trends are correctly predicted, the magnitudes of protrusion spacing observed are not in agreement with the predictions of the stabilty theories discussed in chapter 2. Of the three formulations of the stability theory discussed in chapter 2, the theory derived here gives relatively the closest approach.

Disagreement between theory and experiment could arise because the perturbation analysis breaks down for roughness of significant amplitude. In this case an acceleration in the growth rates of larger features would raise the average above that predicted by the perturbation theories. There may also be a lower limit on the spacing of protrusions set by phenomena not considered in the theories. This issue is addressed in sections 5-5-2 and 5.5.3.
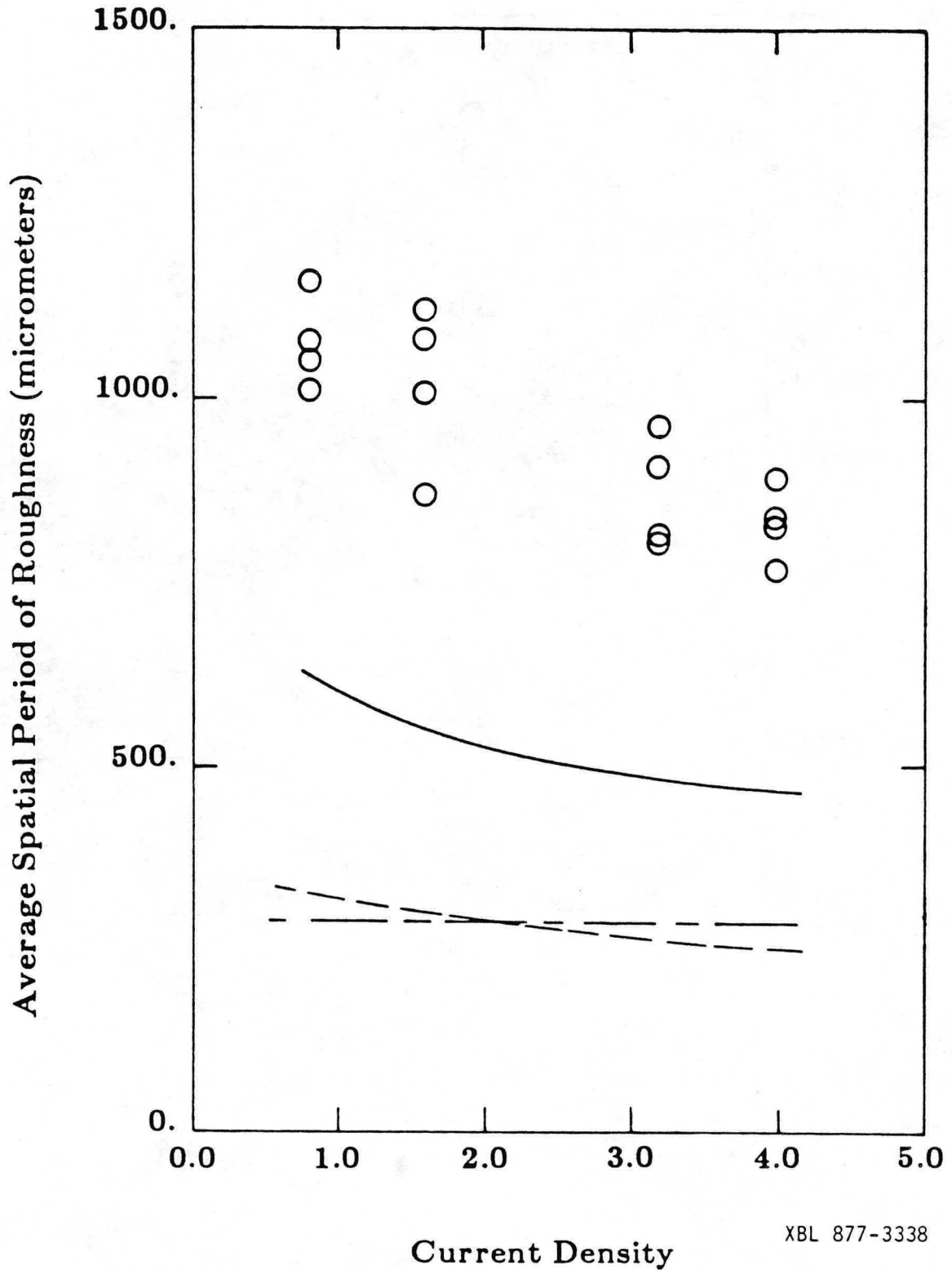
Figure 5-20: Average spatial period of roughness predicted by stability theories versus current density for copper deposition from a 1.0 M CuSO$_4$/1.0 M H$_2$SO$_4$ electrolyte at 50° C and 80% of limiting current. Also shown are the measured values.
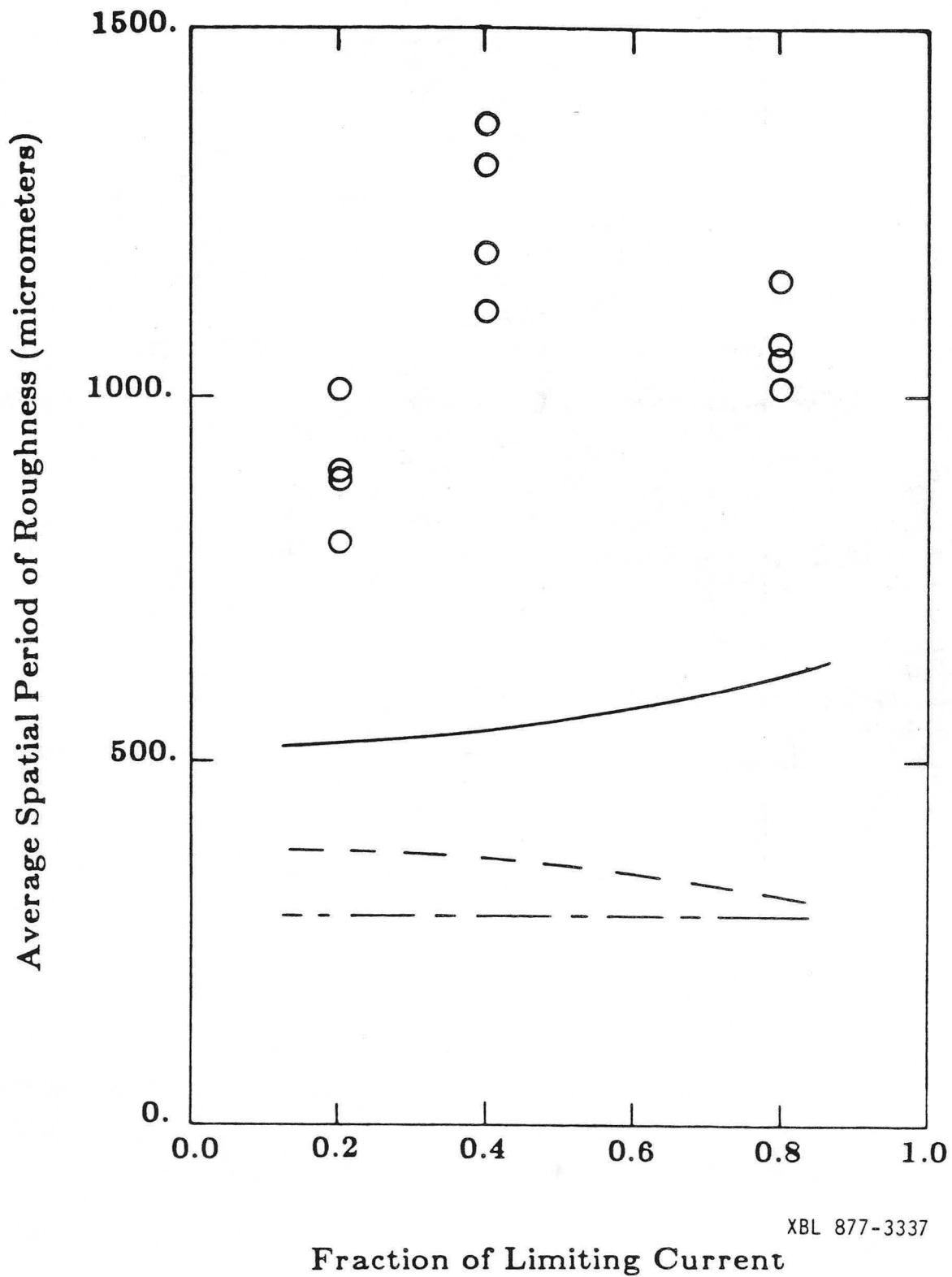
XBL 877-3338

Figure 5-21: Average spatial period of roughness predicted by stability theories versus fraction of limiting current for deposition from a 1.0 M CuSO$_4$/1.0 M H$_2$SO$_4$ electrolyte at 50° C at 0.8 A/cm^2. Also shown are the measured values.

XBL 877-3337

While incorporation of field effects in the stability analysis leads to a correct prediction of the dependence of roughness amplitude on fraction of limiting current, it fails to predict the observed decrease of amplitude with increase in the absolute value of the current density. It should be noted that the stability theories are perturbation techniques designed to predict the protrusion spacing and cannot be rigorously extended to roughness of appreciable amplitude.

5.5.2 Effects of Nucleation

The number density of nucleation should have an important effect on the observed protrusion spacing. It was observed that the smallest features in the deposits formed in this study were individual nodules of a few tens of micrometers in diameter. This scale sets a lower limit on the protrusion spacing that may account for the unexpectedly large average spatial periods observed.

Figures 5-22 and 5-23 present scanning electron micrographs of the surfaces of two deposits formed at 80% of limiting current and 0.8 and 4.0 A/cm^2 respectively. The deposit formed at low current density is much rougher and crumbled when it was removed from the cathode. The micrographs show that this deposit is composed of larger nodules than that formed at high current density, probably as a result of lower number density of nucleation.

For the thick depsoits formed here, there was little change in spatial period with charge passed (figure 5-24), although the etched cross section in figure 5-15 shows evidence of an increase in nodule size with charge passed in the earlier stages of deposition. The spatial period and nodule size evidently approach a

A   B
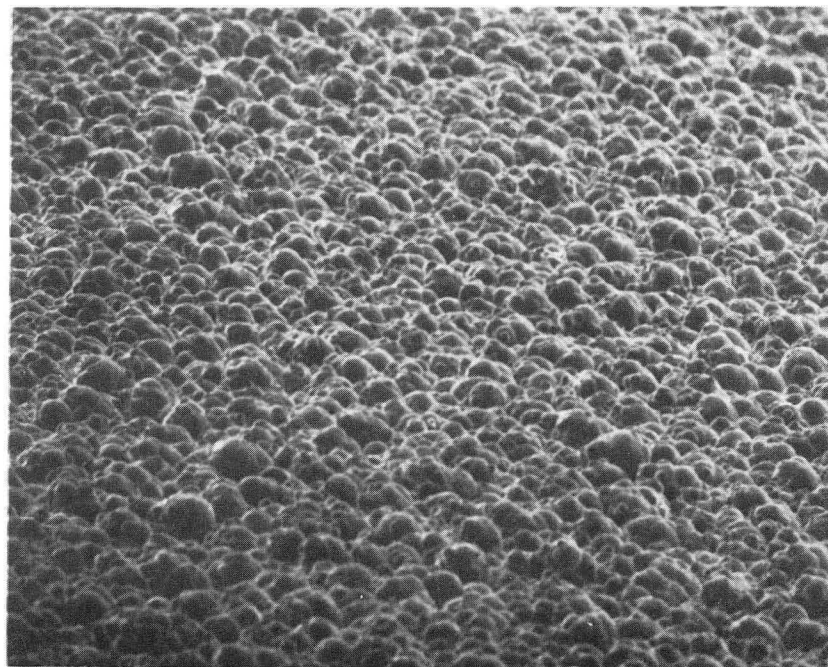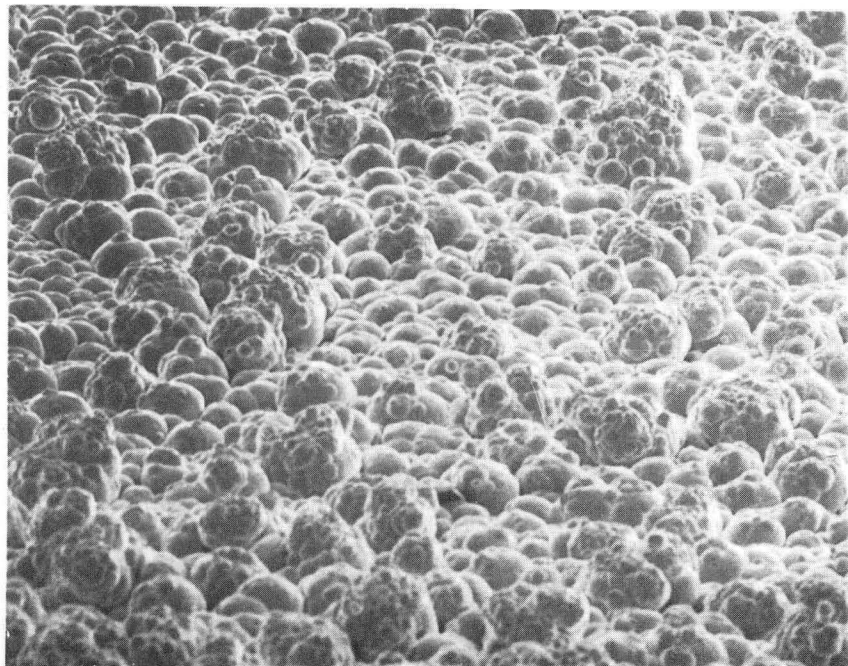
XBB 877-5635

200μm

Figure 5-22: Scanning electron micrographs of surfaces of deposits formed at 80% of limiting current from 1.0 M $CuSO_4$/1.0 M H_2SO_4 at 50° C. Tilt angle: 60 degrees. A) 0.8 A/cm^2. B) 4.0 A/cm^2

A

B
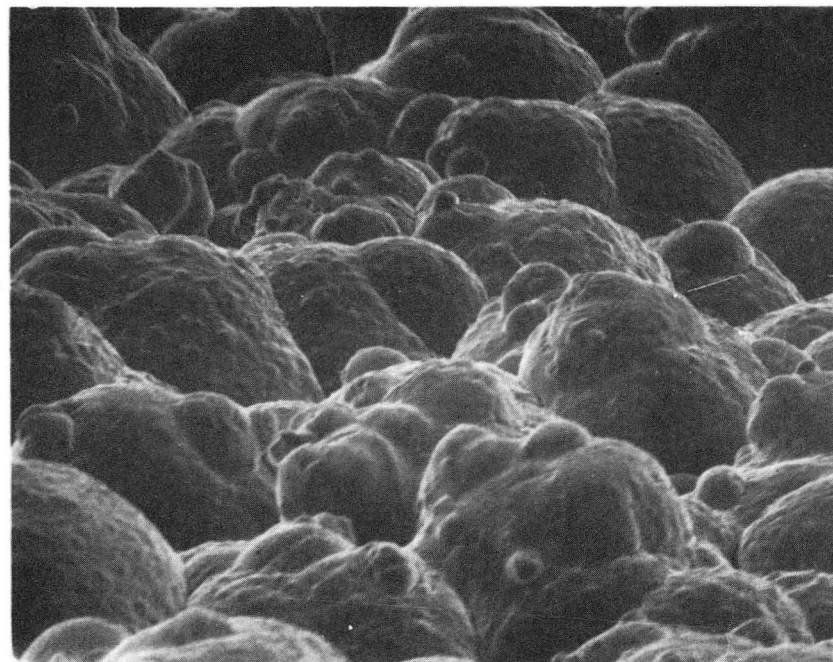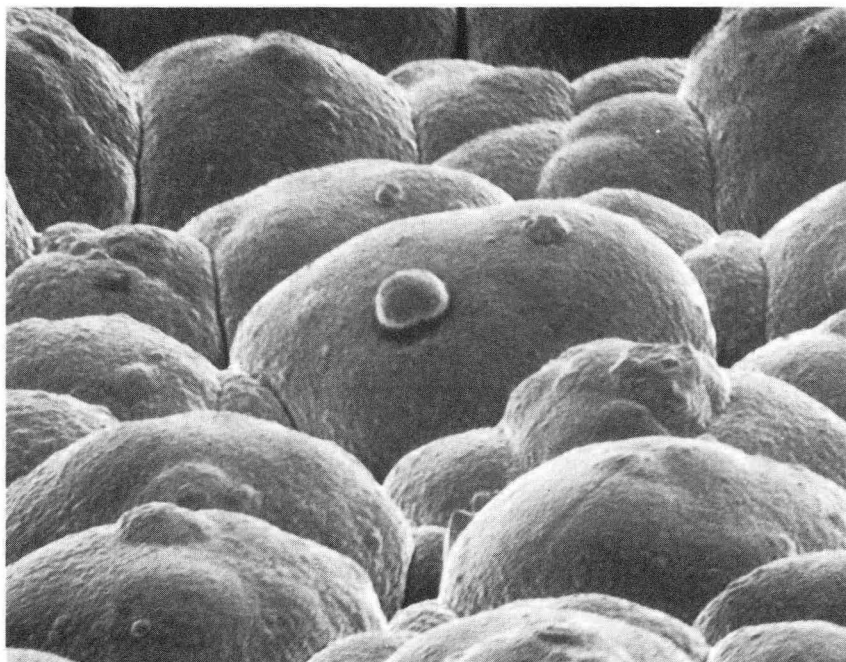
XBB 877-5634

$$20\,\mu\mathrm{m}$$

Figure 5-23: Scanning electron micrographs of surfaces of deposits formed at 80% of limiting current from 1.0 M $CuSO_4$/1.0 M H_2SO_4 at 50° C. Tilt angle: 60 degrees. A) 0.8 A/cm^2. B) 4.0 A/cm^2
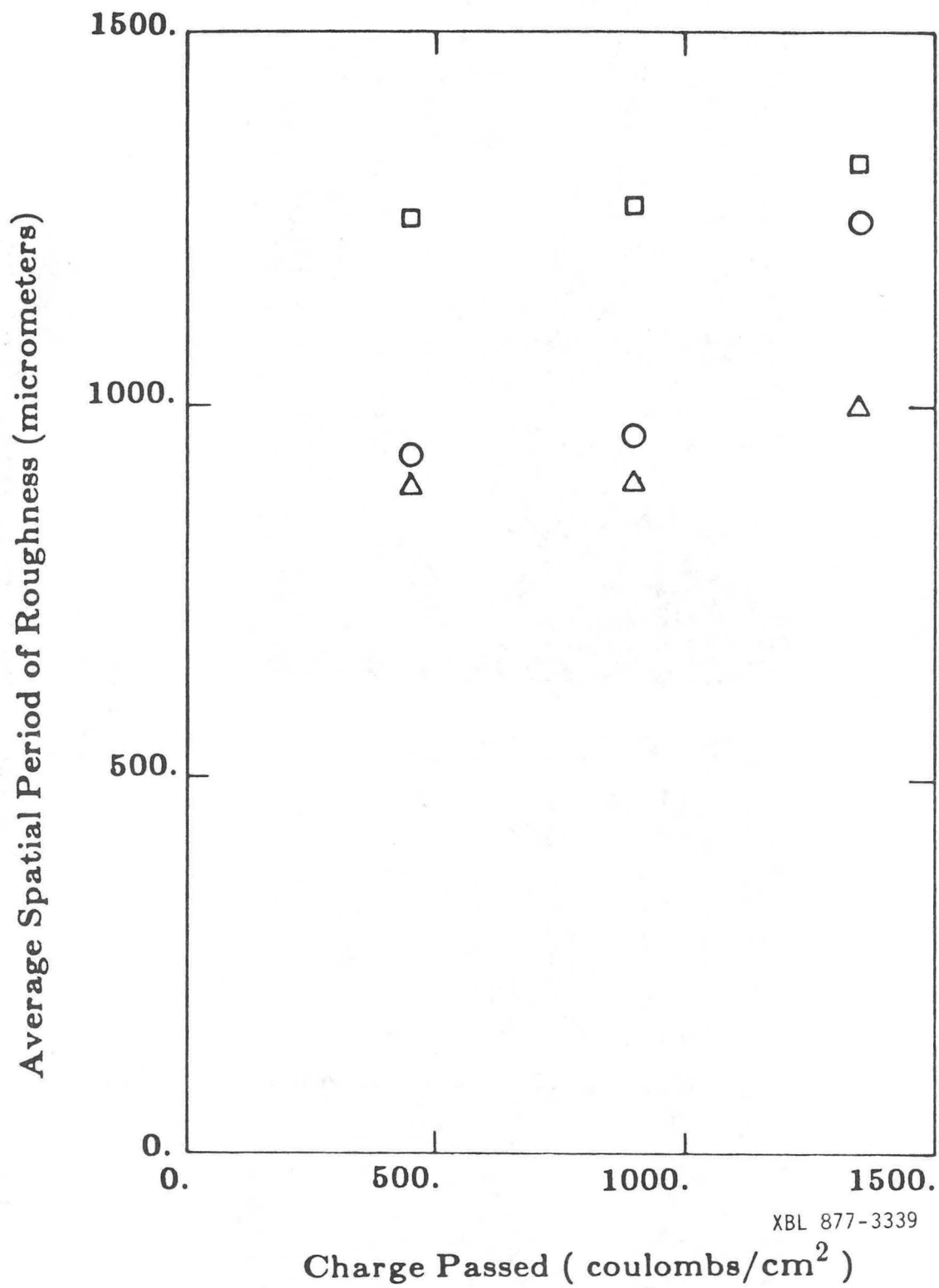
Figure 5-24: Average spatial period of roughness versus charged passed for deposits formed from 1.0 M CuSO$_4$/ 1.0 M H$_2$SO$_4$ at 50° C. A) 0.8 A/cm^2 at 20% of limiting current. B) 1.6 A/cm^2 at 40% of limiting current. C) 0.8 A/cm^2 at 40% of limiting current.

steady state determined by both nucleation and transport.

5.5.3 Effects of Flow

It was shown in chapter two that a thinning of the mass transfer boundary layer can influence the development of roughness. It is expected to decrease the average amplitude and spatial period of roughness as the thinner boundary layer follows the contours of large features. This is a possible interpretation of the decrease in these two measures with increasing current density and constant fraction of limiting current. The variation of current density at constant fraction of limiting current was achieved by adjusting the rate of cathode motion. Higher current densities correspond to thinner mass-transfer boundary layers, and hence finer, lower-amplitude roughness.

This interpretation is strongly supported by the observation that fine roughness, within the mass-transfer boundary layer for all the conditions applied in the experiments, was independent of current density at constant fraction of limiting current. The fine roughness amplitude depended only on the fraction of limiting current, a measure of the approach to mass transport control, while larger features, apparently large, widely spaced nodules, were sensitive to the kinetics of crystallization.

One other effect of flow must be considered. That is the stirring effect of the rough deposits and its influence on the actual limiting current densities during the deposition experiments. The limiting currents were estimated with the assumption of a smooth cathode. The validity of this assumption can be tested

with equation 4-2 for the critical scale of roughness above which the dependence of limiting current on rotation rate changes from the 0.7 power to the first power. For the highest Reynolds numbers used in the deposition experiments, the critical dimension is about 20 micrometers. The amplitude of the roughest deposits is greater than this value. It might therefore be expected that the deposits formed at high current density, and hence high rate of cathode movement, were smoother because they were formed at a lower fraction of limiting current than was assumed. However, the effect of stirring would not appear until much of the final roughness had already developed. The protrusion spacing would be determined in the earlier stages of deposition when the assumption of a smooth cylinder was valid.

Increase in the deposit surface area with deposition also changes the absolute current density if the total current is constant. In this case the current density would be decreased the most for the roughest deposits. Since a decrease in roughness with increasing current was observed, this effect cannot account for the experimental results.

5.5 Conclusion

It has been shown that the stability theories of Aogaki and Landau can be extended to the general case of mixed ohmic, kinetic and transport controlled deposition. The criterion for stability, which is essential for analyzing dendritic growth near the limiting current, is the same for all three theories. For deposition under conditions appropriate for electroforming, however, the theories

diverge in their predictions of protrusion spacing. The theory developed here best predicts the magnitudes and trends in protrusion spacing with conditions of copper deposition at high rates.

A complete interpretation of the development of surface texture in electroforming requires consideration of nucleation and flow phenomena. The number density of nucleation, which is sensitive to the deposition rate, places a lower limit on the protrusion spacing. The high rates of cathode movement employed here generate mass transport boundary layers of a few micrometers in thickness. Ibl's picture of a thin boundary layer following larger features while non-uniformly inhibiting smaller ones has been verified. Separation of the observed roughness into two size regimes by a Fourier transform technique showed that the smaller scale features are influenced only by the conditions of mass transport.

The combined influences of nucleation density, boundary layer thinning and surface stability produce a trend toward finer grained, smoother deposits as the current density is increased at constant fraction of limiting current. The trend toward finer, smoother deposits as the current density increases suggests that high current density may be a partial substitute for the use of electrolyte additives. It is clear that metal deposition can be accelerated far beyond conventional rates using cathode movement to produce intense turbulent convective transport without sacrifice of deposit quality.

Appendix A. Derivation of Stability Equation

First the potential and concentration fields have to be determined for deposition at a constant current on a two dimensional flat surface of infinite extent with consideration of concentration, kinetic and ohmic overpotential. The current distribution for deposition on a low amplitude sinusoidal profile is then found by a perturbation technique. Calculation of the current distribution from the electric field yields the growth rate of the perturbation amplitude.

The equations and boundary conditions are shown in figure 2-5. The variables x,y, and z are the position coordinates on the surface and distance from the surface, respectively. The electric field, ϕ, obeys Laplace's equation everywhere:

$$\nabla^2 \phi = 0 \qquad\qquad (A\text{-}1)$$

Mass transport is assumed to occur by diffusion only and to be confined to a layer of thickness, δ, measured from the average plane of the surface. At $z = \delta$ the concentration equals the bulk value. Within the diffusion layer it obeys Laplace's equation.

$$\nabla^2 c = 0 \qquad\qquad (A\text{-}2)$$

The concentration and electric fields for constant current deposition at a flat surface under these conditions are

$$c^o = c_b[1 - \frac{i_A}{i_L}(1 - \frac{z}{\delta})] \qquad\qquad (A\text{-}3)$$

and

$$\phi^\circ = \frac{RT}{\alpha\, nF}\ln(\frac{i_A}{i_o}) + \frac{RT}{nF}\ln(1 - \frac{i_A}{i_L}) + \frac{i_A}{\kappa}z \qquad (A-4)$$

where i_o is the exchange current density, i_A the current density for the flat surface and i_L the diffusion limited current density.

For a sinusoidal profile of low amplitude the boundary conditions on the electric field are

$$\frac{\partial\phi}{\partial z} = \frac{i_A}{\kappa}, \quad z \rightarrow \infty \qquad (A-5)$$

$$\frac{\partial\phi}{\partial x} = 0, \quad \omega x = \frac{\pi}{2}, \frac{3\pi}{2} \qquad (A-6)$$

$$\frac{\partial\phi}{\partial y} = 0, \quad \omega y = \frac{\pi}{2}, \frac{3\pi}{2}$$

At the surface, the potential includes terms for the kinetic, concentration and capillary overpotentials respectively,

$$\phi\,|_{z=z_s} = \phi_a + \phi_c + \phi_s \qquad (A-7)$$

$$= \frac{RT}{\alpha\, nF}\ln(\frac{i}{i_o}) + \frac{RT}{nF}\ln(1 - \frac{i}{i_L}) + \frac{2\,\nu\,\gamma\,\omega^2}{nF}$$

where

$$z_s = A\,\sin(\omega_x x)\,\sin(\omega_y y) \qquad (A-8)$$

$$2\omega^2 = \omega_x^2 + \omega_y^2$$

Boundary conditions for the concentration are

$$c = c_{b,} \quad z = \delta \qquad (A-9)$$

and

$$\frac{\partial c}{\partial x} = 0, \quad \omega x = \frac{\pi}{2}, \frac{3\pi}{2} \tag{A-10}$$

$$\frac{\partial c}{\partial y} = 0, \quad \omega y = \frac{\pi}{2}, \frac{3\pi}{2}$$

At the surface the gradients of the concentration and electric potential fields must match through the current density.

$$nFD\frac{\partial c}{\partial z}\Big|_{z=z_s} = \kappa\frac{\partial \phi}{\partial z}\Big|_{z=z_s} = i\Big|_{z=z_s} \tag{A-11}$$

The concentration and electric fields take the forms

$$c = c^\circ + c^P A \left[e^{-\sqrt{2}\omega z} - e^{\sqrt{2}\omega z - 2\sqrt{2}\omega \delta}\right] \sin(\omega_x x) \sin(\omega_y y) \tag{A-12}$$

and

$$\phi = \phi^\circ + \phi^P A \left[e^{-\sqrt{2}\omega z}\right] \sin(\omega_x x) \sin(\omega_y y) \tag{A-13}$$

respectively. The expression for ϕ satisfies equation A-1 and the boundary conditions A-5 and A-6. The expression for c satisfies equation A-2 and the boundary conditions A-9 and A-10. Values of the constants ϕ^P and c^P must be found to satisfy the boundary conditions A-7 and A-11.

The expressions for the kinetic and concentration overpotentials are linearized as follows:

$$\phi_a = \phi_a{}^\circ + \frac{\partial \phi_a}{\partial i}\Big|_{i=i_A}(i-i_A) \tag{A-14}$$

$$\phi_c = \phi_c{}^\circ + \frac{\partial \phi_c}{\partial i}\Big|_{i=i_A}(i-i_A) + \frac{\partial \phi_c}{\partial z}\Big|_{z=0}(z_s) \tag{A-15}$$

$\phi_a^{\;\circ}$ and $\phi_c^{\;\circ}$ are, respectively, the kinetic and concentration overpotentials for deposition on a flat surface at current density i_A.

At the sinusoidal surface, the potential, equation A-13, matches the boundary condition A-7.

$$\phi\,|_{z_s} = \phi^\circ\,|_{z_s} + \phi^P A e^{-\sqrt{2}\omega A \sin(\omega_x x)\sin(\omega_y y)}\sin(\omega_x x)\sin(\omega_y y) \qquad \text{(A-16)}$$

$$= \phi_a + \phi_c + \phi_s$$

Substitution of the linearized expressions, A-14 and A-15, gives

$$\phi^P A \left[e^{-\sqrt{2}\omega A \sin(\omega_x x)\sin(\omega_y y)} \right] \sin(\omega_x x)\sin(\omega_y y) = \qquad \text{(A-17)}$$

$$\frac{RT}{\alpha\, nFi_A}(i - i_A) - \frac{RT}{nF}\frac{(i - i_A)}{(i_L - i_A)}$$

$$+ \frac{RTi_A}{nFDc_b(1 - \dfrac{i_A}{i_L})} A\,\sin(\omega_x x)\sin(\omega_y y)$$

$$- \frac{2\,\nu\,\gamma\,\omega^2}{n^2 F^2} A\sin(\omega_x x)\sin(\omega_y y)$$

Subsitution of equation A-11 for i yields

$$\phi^P A \left[e^{-\sqrt{2}\omega A \sin(\omega_x x)\sin(\omega_y y)} \right] \sin(\omega_x x)\sin(\omega_y y) = \qquad \text{(A-18)}$$

$$\frac{RT}{\alpha nFi_A}\kappa\phi^P A \,\omega \left[e^{-\sqrt{2}\omega A \sin(\omega_x x)\sin(\omega_y y)} \right] \sin(\omega_x x)\sin(\omega_y y)$$

$$- \frac{RT}{nF\,(i_L - i_A)}\kappa\phi^P A\omega \left[e^{-\sqrt{2}\omega \sin(\omega_x x)\,\sin(\omega_y y)} \right]\sin(\omega_x x)\sin(\omega_y y)$$

$$+ \ \frac{RTi_A}{nFD \ c_b(1 - \frac{i}{i_A})} A\sin(\omega_x x)\sin(\omega_y y)$$

$$- \ \frac{2 \ \nu \ \gamma \ \omega^2}{n^2 F^2} A\sin(\omega_x x)\sin(\omega_y y)$$

which can be solved for ϕ^P

$$\phi^P \ = \ [e^{\sqrt{2}\omega A\sin(\omega_x x)\sin(\omega_y y)}] \frac{\dfrac{RTi_A}{n^2F^2Dc_b(1 - \frac{i}{i_L})} - \dfrac{2 \ \nu \ \gamma \ \omega^2}{nF}}{1 \ + \ \dfrac{RT}{nF(i_L - i_A)}\kappa\omega + \dfrac{RT}{\alpha nFi_A}\kappa\omega} \qquad \text{(A-19)}$$

The exponential factor approaches unity in the limit of small A and can be neglected. Evaluation of equation A-13 for the potential gradient at the interface yields the current distribution.

$$i \ = \ \kappa \ \sqrt{2} \ \omega \ \phi^P \ A \ \sin(\omega_x x) \ \sin(\omega_y y) \qquad \text{(A-20)}$$

The amplitude growth rate is

$$\frac{\partial \ln A}{\partial t} \ = \ \kappa \ \sqrt{2} \ \omega \ \frac{\nu}{nF}\phi^P \qquad \text{(A-21)}$$

The constant c^P can be found using equation A-18 and the boundary condition A-11:

$$c^P \ = \ \frac{\kappa}{nFD} \frac{1}{(1 \ + \ e^{-2 \ \sqrt{2} \ \omega \ \delta})}\phi^P \qquad \text{(A-22)}$$

Appendix B: Rate of Approach to Steady State

The diffusion equation for an infinite flat surface advancing at a velocity, v, is

$$\frac{\partial^2 c}{\partial z^2} + \frac{v}{D}\frac{\partial c}{\partial z} = \frac{\partial c}{\partial t} \qquad (B\text{-}1)$$

The boundary conditions are

$$c \to c_b, \quad z \to \infty \qquad (B\text{-}2)$$

$$\frac{\partial c}{\partial z} = \frac{i}{nFD}, \quad z = 0$$

$$c = c_b, \quad t = 0$$

The concentration takes the form (163):

$$c = u\, e^{\left(-\frac{v}{2D}z - \frac{v^2}{4D}t\right)} + c_s \qquad (B\text{-}3)$$

where U is a function of z and t, and c_s is the steady state concentration (108).

$$c_s = c_b\left(1 - \frac{i}{i_L}\right) + \frac{i}{nFv}\left(1 - e^{-\frac{v}{D}z}\right) \qquad (B\text{-}4)$$

With substitution of B-3 and B-4, B-1 reduces to

$$\frac{\partial^2 u}{\partial z^2} = \frac{\partial u}{\partial t} \qquad (B\text{-}5)$$

Solution of equation B-1 yields for the concentration

$$c = e^{\left(-\frac{V}{2D}z - \frac{V^2}{4D}t\right)} erfc\left(\frac{z}{\sqrt{4Dt}}\right) + c_s \qquad (B\text{-}6)$$

The transient term decays with a time constant

$$\tau = \frac{2D}{v^2} \tag{B-7}$$

For copper deposition at 1.0 amperes per square centimeter, D is about $0.5 \times 10^{-5} \text{cm}^2/\text{s}$, v is $2.5 \times 10^{-3} \text{cm/s}$ and τ^{-1} is roughly 4.0×10^3 s.

The approach to steady state may also be estimated by comparing the velocity of penetration of the diffusion layer with the rate of advance of the surface. For a steady state to be maintained, these velocities must be equal. The penetration velocity is

$$v_p = 2\sqrt{D/t} \tag{B-8}$$

The rate of surface advance is

$$v = \frac{\nu}{nF} i \tag{B-9}$$

Equating the two velocities and solving for t yields the time elapsed before attainment of the steady state:

$$t = D\left(\frac{inF}{\nu}\right)^2 = 10^4 \text{ s} \tag{B-10}$$

The relaxation time decreases with increasing current density. Calculations using Landau's equation (equation 2-15) for the amplitude growth rate for current densities of a few amperes per square centimeter, showed that neglect of the surface movement term results in a difference of roughly two percent in the average spatial period predicted.

Appendix C. Calculation of Fourier Transforms

Program PFT4

PFT4 calculates the Fourier transform of a surface profile by Romberg integration with repeated interval halving. It is adapted from a program given by Carnahan, Luther and Wilkes (164).

```
        INTEGER IJ ,I, IND, KRPF(7), LACF(7), KS, KT
        REAL Y(2048), SCP, FSNT(512), FCNT(512)
100     FORMAT(8F6.0)
200     FORMAT(F8.2)
300     FORMAT(4E15.5)
400     FORMAT(I5)
500     FORMAT(2(2X,7A2))
        OPEN(UNIT=3,NAME='LST.DAT',TYPE='OLD')
        READ(3,400) IND
```

LST contains a list of file names to be read. IND is the number of files listed.

```
        DO 2 IJ=1,IND
        READ(3,500) KRPF, LACF
```

KRPF is the file containing the surface profile. LACF is the file to receive the transform.

```
        OPEN(UNIT=1,NAME='KRPF',TYPE='OLD')
        OPEN(UNIT=2,NAME='LACF.DAT',TYPE='OLD')
        READ(1,200) SCP
        WRITE(2,200) SCP
```

SCP is the profilometer scale in microinches per division used in collecting the surfce profile. To convert the numbers in the file to micrometers, multiply by $SCP \times 3.38 \times 10^{-4}$.

```
        READ(1,100) (Y(I),I=1,2048)
```

Y is the surface profile.

```
        KS=11
        CALL NVMTRX(Y, KS, SCNM)
```

NVMTRX is a subroutine that flattens the profile by fitting and subtracting out a cubic polynomial. SCNM is $Y_{max} - Y_{min}$.

```
      KT=8
      CALL FTS(KS, KT, Y, FSNT)
      CALL FTC(KS, KT, Y, FCNT)
```

FTS and FTC determine the Fourier sine and cosine series respectively. The profile length is $2^{(KS)}$ *and the series is determined for* $2^{(KT)}$ *harmonics of the profile length.*

```
      WRITE(2,300) (FSNT(I),I=1,2**KT)
      WRITE(2,300) (FCNT(I),I=1,2**KT)
      CLOSE(UNIT=1,DISPOSE='SAVE')
      CLOSE(UNIT=2,DISPOSE='SAVE')
2     CONTINUE
      STOP
      END
```

Subprogram NVMTRX

Program NVMTRX fits and subtracts out a cubic polynomial to flatten a surface profile F(X) by Gauss-Jordan elimination. It is adapted from a program given by Carnahan, Luther and Wilkes (164).

```
      SUBROUTINE NVMTRX(F, KS, SCNM)
      INTEGER I, J, K, J1, LMX
      REAL X, YMAX, YMIN, F(4096)
      DIMENSION A(4,9)
```

Find the maximum and minimum values of F and normalize.

```
      LMX=2**KS
      YMIN= 2000.
      YMAX=-2000.
      DO 5 I=1, LMX
      IF(F(I) .LT. YMIN) YMIN=F(I)
      IF(F(I) .GT. YMAX) YMAX=F(I)
5     CONTINUE
      SCNM=YMAX - YMIN
      DO 13 I=1, LMX
      F(I)=F(I)/SCNM
13    CONTINUE
```

Initialize the matrix A. A represents the system of equations which express the condition of least squares fit between the cubic polynomial and the function F.

```
        DO 1 I=1,4
        DO 2 K=1,9
        A(I,K)=0.0
2       CONTINUE
1       CONTINUE
        DO 3 I=1,LMX
        X=FLOAT(I)*10.0/FLOAT(LMX)
        A(2,1)=A(2,1)+X
        A(3,1)=A(3,1)+X**2
        A(4,1)=A(4,1)+X**3
        A(4,2)=A(4,2)+X**4
        A(4,3)=A(4,3)+X**5
        A(4,4)=A(4,4)+X**6
        A(1,5)=A(1,5)+F(I)
        A(2,5)=A(2,5)+F(I)*X
        A(3,5)=A(3,5)+F(I)*X**2
        A(4,5)=A(4,5)+F(I)*X**3
3       CONTINUE
        A(1,1)=FLOAT(LMX)
        A(1,2)=A(2,1)
        A(2,2)=A(3,1)
        A(3,2)=A(4,1)
        A(1,3)=A(2,2)
        A(2,3)=A(3,2)
        A(3,3)=A(4,2)
        A(1,4)=A(2,3)
        A(2,4)=A(3,3)
        A(3,4)=A(4,3)
        A(1,6)=1.0
        A(2,7)=1.0
        A(3,8)=1.0
        A(4,9)=1.0
```

Invert the matrix A by Gauss Jordan elimination.

```
        DO 4 K=1,4
10      A(K,J)=A(K,J)/A(K,K)
        A(K,K)=1.0
        DO 4 I=1,4
        IF(I .EQ. K .OR. A(I,K) .EQ. 0.) GO TO 4
        DO 7 J=J1,9
7       A(I,J)=A(I,J)-A(I,K)*A(K,J)
        A(I,K)=0.
4       CONTINUE
```

Evaluate the polynomial and subtract it from F.

```
            DO I=1,LMX
            X=FLOAT(I)*10./FLOAT(LMX)
            F(I)=F(I)-A(1,5)-A(2,5)*X-A(3,5)*X**2-A(4,5)*X**3)*SCNM
   8        CONTINUE
            RETURN
            END
```

Program FTS

FTS calculates the Fourier sine transform of the function F. FTC calculates the cosine series by the same procedure. The number of points in the profile is $2^{**}NMAX$. The number of harmonics found is $2^{**}PMAX$. The Fourier coefficients make up the array FSNT.

```
            SUBROUTINE FTS(NMAX,PMAX,F,FSNT)
            INTEGER I,J,K,PMAX,IMAX,J1,NVMJP2,N,JMAX,NMAX,IFR
            DIMENSION T(14,7)
            REAL FSNT(512),XSI(4096),F(4096),XRC,FORJM1
            LMAX+2**NMAX
            JMAX=7
            DO 5 J1=1,2**PMAX
            DO 10 I=1,LMAX
            XSI(I)=F(I)*SIN(FLOAT(J1)*3.14159*FLOAT(I)/FLOAT(LMAX))
   10       CONTINUE
            T(1,1)=(XSI(1)+XSI(LMAX))*FLOAT(LMAX)/2.0
            DO 12 N=1,NMAX
            T(N+1,1)=0.0
            IFR=2**(NMAX-N)
            IMAX=(2**N)-1
            DO 11 I=1,IMAX,2
   11       T(N+1,1)=T(N+1,1)+XSI(I*IFR)
   12       T(N+1,1)=T
            DO 13 J=2,JMAX
   13       T(N,J)=(FORJM1*T(N+1,J-1)-T(N,J-1))/(FORJM1-1.0)
            FSNT(J1)=T(NXMJP2,JMAX)/FLOAT(LMAX)
   5        CONTINUE
            RETURN
            END
```

Appendix D. Calculation of Electrolyte Properties

Diffusivities of cupric ion were calculated with the correlation for rotating disk integral diffusivities determined by Sellman (152).

$$\frac{\mu D}{T} = 2.01 \times 10^{-10} \qquad \text{(D-1)}$$

μ is the dynamic viscosity in cP, D the diffusivity in cm^2/s and T the temperature in degrees K.

Densities (ρ), viscosities (μ) and conductivities (κ) were calculated with correlations determined by Price and Davenport for $CuSO_4/H_2SO_4$ (151).

$$\rho = 1.01856 + 0.00238[Cu] + 0.00054[H_2SO_4] - 0.00059T(C) \qquad \text{(D-2)}$$

ρ is the density in g/cm^3, [Cu] and [H_2SO_4] the copper and H_2SO_4 concentrations in g/dm^3 and T the temperature in degrees C.

$$\kappa = 0.134 - 0.00356[Cu] + 0.00249[H_2SO_4] + 0.00426T(C) \qquad \text{(D-3)}$$

κ is in $ohm^{-1}cm^{-1}$.

$$\mu = 10^{-6}(1592. + 0.0108[H_2SO_4]^2 + 2.373[H_2SO_4] \qquad \text{(D-4)}$$

$$+ 29.93[Cu] + 76.48[Cu]^{1/2}exp\frac{1890.}{T(K)}$$

Appendix E Symbols

A   Profile amplitude (cm)

c   Concentration of cupric ion (M/cm^3)

c_b Bulk concentration

c_i Interfacial concentration

c_s Steady state concentration

c^o Concentration for flat surface

c^p Concentration perturbation magnitude

D   Diffusivity (cm^2/s)

d   RCE diameter (cm)

F   Faraday constant 96480 Coulombs/equivalent

G_c Interfacial concentration gradient

i   Current density (A/cm^2)

i_A Average curent density

i_L Limiting current density ·

i_o Exchange current density

L   Characteristic length (cm)

n   Charge per ion (equivalents/mole)

R   Gas constant 8.314 (Joule/mole-K)

r   Radius of curvature (cm)

Re   Reynolds number $\Omega d^2/\nu$

Re_c Critical Reynolds number for roughness

Sc	Schmidt number (ν/D)
Sh	Sherwood number (id/nFc_bD)
T	Temperature (K)
t	Time (s)
v	Velocity of surface advance (cm/s)
v_p	Penetration velocity (cm/s)
Wa	Wagner number, $\dfrac{\partial\eta_a}{\partial\eta_r}$
Wc	Wagner number, $\dfrac{\partial\eta_c}{\partial\eta_r}$
Wd	Wagner number, $\dfrac{\partial\eta_a}{\partial\eta_c}$
Ws	Dimensionless group, $\dfrac{2\nu\gamma\omega^2}{\delta RT}$
x,y	Position coordinates parallel to average surface
z	Position coordinate normal to average surface
z_s	Value of z at surface
α	Charge transfer coefficient
∇^2	Laplace operator
δ	Nernst diffusion layer thickness
ϵ	Roughness amplitude (cm)
η_a	Activation overpotential
η_c	Concentration overpotential
η_r	Ohmic overpotential
η_s	Capillary overpotential

κ	Conductivity ohm^{-1} cm^{-1}
λ	Spatial period (cm)
μ	Viscosity (centipoise)
ν	Molar volume (cm^3/mole)
ω	Spatial frequency (cm^{-1})
ϕ	Potential (volts)
ϕ_a	Activation overpotential
ϕ_c	Concentration overpotential
ϕ_s	Capillary overpotential
ϕ^o	Potential for flat surface
ϕ^p	Potential perturbation magnitude
τ	Time constant (s^{-1}) for decay of transient
Ω	Rotation rate (radians/s)

References

1) W.H. Safranek, Plating, 53, 1211 (1966)

2) Spiro, "Electroforming", Draper, Teddington (1971)

3) B.Ya. Kaznachi, Zhurnal Vses. Khim. Ob-va im. Mendeleeva, 25, 192 (1980)

4) G.G. Weiler, Angew. Electrochemie, 26, 381 (1972)

5) A.D. Squitero, Met. Finish., 35, 63 (1982); 35, 69 (1982)

6) G.A. DiBari, Plat. & Surf. Finish., 70,32 (1983)

7) S.A. Watson, Plat. & Surf. Finish., 62, 851 (1975)

8) Nickel Topics, August 18, 1982 p. 7

9) P. Baeyens, Plating, 53, 591 (1966)

10) M. Mattia, Plating, 55, 40 (1968)

11) S.J. Beyer, Plating, 56, 60 (1969)

12) Foundry Trade Journal, 155, 54 (1983)

13) W.R. Wearmouth, Met. Finish., 33, 35 (1980)

14) F.A. Watson, D.K. Worn, The Metallurgist and Materials Technologist, June, 1981, p. 310

15) W.R. Wearmouth, K.C. Belt, Trans. Inst. Met. Finish., 52, 114 (1974)

16) W.T. Mcfarlen, Plating, 57, 46 (1970)

17) W.B. Stephenson Jr., Plating, 53, 183 (1966)

18) W.R. Wearmouth, K.C. Belt, Plat. & Surf. Finish., 66,53 (1979)

19) A. Mayer, K. Staudhammer, K.Johnson, Plat. & Surf. Finish., 72,76 (1985)

20) W.S. DeForest, J. Widmont, Plating, 57,479 (1970)

21) W.P. Dugan, Plat. & Surf. Finish., 61,569 (1974)

22) Plat. & Surf. Finish., 62,219 (1975)

23) G.R. Schaer, T.Wada, Plat. & Surf. Finish., 68,52 (1981)

24) T.R. Bates, Plating, 52,673 (1965)

25) Lloyd Lowry, Plat. & Surf. Finish., 58, 199 (1971)

26) Michael Meier, Galvanotechnik, 69, 593 (1978)

27) Jurgen Leudolph, Galvanotechnik, 72,717 (1981)

28) J.L. Jostan, A.F. Bogenschutz, Plating, 56,399 (1969)

29) G.C. Van Tilburg, Plat. & Surf. Finish., 75,78 (1984)

30) D. Withy, Gold Bull., 16,70 (1984)

31) P.C. Hydes, H. Middleton, Gold Bull., 12,90 (1979)

32) G. Desthomas, Aurum, 14,19 (1983)

33) G. Desthomas, Aurum, 15,17 (1983)

34) Prod. Finish., 21(11),32 (1968)

35) S.F. Hardy, J.A. McGeough, R.M. Tulloch, Surf. Tech., 12,39 (1981)

36) S.H.F. Lai, J.A. McGeough, Trans. Inst. Met. Finish., 57,72 (1979)

37) H. Silman, Met. Finish., 67,36 (1969)

38) P.K. Subramanian, W.M. King, Plat. & Surf. Finish., 73,49 (1982)

39) W.H. Safranek, W.C. Schicker, C.L. Faust, J. Electrochem. Soc., 99,153 (1952)

40) F.J. Schmidt, I.J. Hess, Plating, 53,229 (1966)

41) J.W. Dini, J.R. Helms, Met. Finish., 67(8),53 (1969)

42) D. Schlain, F.X. McCawley, G.R. Smith, Platinum Metals Review, 21(2),38

(1977)

43) F.R. Morral, Plating 50,733 (1963)

44) G.W. Mellors, S. Senderoff, Plating, 51,972 (1964)

45) W.A. Wallace, V.P.Greco, Plating, 57,342 (1970)

46) J.C. Withers, E.F. Abrams, Plating, 55,605 (1968)

47) M.T. Giles, Manufacturing Engineering, June, 1982 p. 61

48) Cutting Tool Engineering, 33,19 (1981)

49) C. Ogden, Plat. & Surf. Finish., 73,130 (1986)

50) P. Jayakrishnan, N.V. Parthasaradhy, S.R. Rajagopalan, Plating, 53,1453 (1966)

51) W.P. Dugan, Plating, 61,1019 (1974)

52) O. Tuscher, R. Suchentrunk, Metalloberflache 32,77 (1978)

53) H.T. Wilson, Plating, 58,345 (1971)

54) A.C. Hart, Indust. Finish., 25(299),14 (1973)

55) F.C. Bertucio, Met. Finish. 64,61 (1966)

56) R.N. Hanson, D.G. Dupree, K. Lui, Plating, 55,347 (1968)

57) G.R. Schaer, Plating, 55,130 (1968)

58) P.J. Norris, Eng. Mat. & Des., June, 1981 p. 24

59) R. Suchentrunk, Trans. Inst. Met. Finish., 64,19 (1986)

60) H.R. Johnson, J.W. Dini, Plat. & Surf. Finish., 62,456 (1975)

61) J.W. Dini, H.R. Johnson, Plat. & Surf. Finish. 64,44 (1977)

62) W.K. Kelly, J.W. Dini, C.M. Logan, Plat. & Surf. Finish., 69,54 (1982)

63) R. Suchentrunk, O. Tuscher, Galvanotechnik, 70,1179 (1979)

64) T.R. Croucher, Plating, 55,152 (1968)

65) P. Bailin, Plating, 53,658 (1966)

66) K.J. Stagg, Prod. Finish. 31(9),27 (1978)

67) R.W. Schneck, Plat. & Surf. Finish., 71,39 (1984)

68) D.F. Hakala, D.J. Wirscke, "Electroforming in Videodisk Manufacture", in AES International Symposium on Electroforming/Deposition Forming, March 23-24, 1983, American Electroplaters Society Press, (1983)

69) Finishing Industries, 2(11),40 (1978)

70) Nickel Topics, 31(2),11 (1978)

71) T.C. Franklin, Plating, 58,813 (1971)

72) W.D. Williams, N. Giordano, Rev. Sci. Instrum., 55,410 (1984)

73) J. Young, F. Ogburn, D. Ballard, Met. Finish. 78,27 (1980)

74) W. Horschmeyer, Copper (Geneva), No. 2, p. 13 (1970)

75) N. Ibl, M. Braun Chemie. Ing. Tech., 45,182 (1973)

76) J.Cl. Puippe, R.E. Acosta, R.J. von Gutfeld, J. Electrochem. Soc., 128,2539 (1981)

77) N. Ibl, "Applications of Mass Transfer Theory: The Formation of Powdered Metal Deposits," in "Advances in Electrochemistry and Electrochemical Engineering," P. Delahay and C.W. Tobias, Eds., Interscience Publishers, New York 2 (1962), pp.49-143.

78) David Jeffries Roha, MS Thesis, Department of Chemical Engineering, University of California, Berkeley, Lawrence Berkeley Laboratory LBL-12737, (1981)

79) A.C. Hart, Met. Austral., 11(7),18 (1979)

80) A.C. Hart, Met. Austral., 11(8), 20 (1979)

81) W.H. Safranek, Plat. & Surf. Finish., 69,48 (1982)

82) G. Schaer, P. Krasley, Plat. & Surf. Finish., 66,36 (1979)

83) A. Weymeersch, L. Renard, J.J. Conreur, R. Winand, M. Jorda,C. Pellet, Plat. & Surf. Finish., 73,68 (1986)

84) A. Weymeersch, R. Winand, L. Renard, Plat. & Surf. Finish., 68,56 (1981)

85) D.W. Endicott, G.J. Casey Jr., Plat. & Surf. Finish., 67,58 (1980)

86) W.H. Safranek, Plat. & Surf. Finish., 69,48 (1982)

87) D. Chin, Plat. & Surf. Finish., 64,57 (1977)

88) M.F. El-Shazley,J.L. White, E.W. Brooman, Plat. & Surf. Finish., 74,136 (1987)

89) S. Eisner, Plating, 58,993 (1971)

90) Products Finishing (Cincinnati), 35(11),50 (1971)

91) R. Thangapan, B. Krishnamurthy, S. Sampath, Met. Finish. 69(12),43 (1971)

92) Products Finishing (Cincinnati), 38(4),48 (1974)

93) Degrez, Winand, Electrochim. Acta., 29,365 (1984)

94) O. Kardos, D.G. Foulke, "Applications of Mass Transfer Theory: Electro-deposition on Small-Scale Profiles", "Advances in Electrochemistry and Electro-chemical Engineering", C.W. Tobias and P. Delahay, Eds., Vol. 4, Interscience, NY (1966)

95) R. de Levie, "Electrochemical Response of Porous and Rough Electrodes",

"Advances in Electrochemistry and Electrochemical Engineering", C.W. Tobias, P. Delahay, Eds., Vol. 6, Interscience NY (1969)

96) N. Ibl, Ph. Javet, F. Stahel, Electrochimica Acta, 17,733 (1972)

97) C. Wagner, J. Electrochem. Soc., 101,225 (1954)

98) P. Fedkiw, J. Electrochem. Soc., 127,1304 (1980)

99) G.A. Prentice, C.W. Tobias, J. Electrochem. Soc., 129,316 (1982)

100) J.A. Mcgeough, H. Rasmussen, J. Mech. Eng. Sci., 18,271 (1976)

101) J.A. Mcgeogh, H. Rasmuusen, J. Mech. Eng. Sci., 19,163 (1977)

102) J.A. Mcgeogh, H. Rasmussen, J. Mech. Eng. Sci., 23,114 (1981)

103) R. Aogaki, K. Kitazawa, Y. Kose, K. Fukei, Electrochimica Acta, 25,965 (1980)

104) R. Aogaki, T. Makino, Electrochimica Acta 26,1509 (1981)

105) R. Aogaki, J. Electrochem. Soc., 129,2442 (1982)

106) R. Aogaki, J. Electrochem. Soc. 129,2447 (1982)

107) R. Aogaki, T. Makino, J. Electrochem. Soc. 131,40 (1984)

108) U. Landau in "Zinc Electrodeposition and Dendritic Growth from Zinc Halide Electrolytes", EPRI Report EM-2393, Electric Power Research Institute, Research Reports Center, Box 50490, Palo Alto, CA 94303, (1982)

109) Andrew Kindler, Ph.D. Thesis, University of California, Berkeley, Lawrence Berkeley Laboratory, LBL 12838, (1981)

110) H.J Pick, G.G. Storey, T.B. Vaughn, Electrochim. Acta 2,165 (1960)

111) Ibid

112) A. Damjanovic, Plating, 52,1017 (1965)

113) J.L. Barton, J. O'M. Bockris, Proc. Royal Soc. of London, Ser. A 268,485 (1962)

114) D.R. Hamilton, Electrochim. Acta, 8,731 (1963)

115) J.W. Diggle, A.R. Despic, J. O'M. Bockris, J. Elecrochem. Soc. 116,1503 (1969)

116) Y. Oren, U. Landau, Electrochim. Acta 27,739 (1982)

117) K.I. Popov, L.J.M. Djukic, M.G. Pavlovic, M.D. Maksimovic, J. Appl. Electrochem. 9,527 (1979)

118) K.I. Popov, M.D. Maksimovic, P.T. Lukic, J. Appl. Electrochem. 10,299 (1980)

119) K.I. Popov, M.D. Maksimovic, J.D. Trnjancev, J. Appl. Electrochem. 11,239 (1981)

120) K.I. Popov, M.D. Maksimovic, S.K. Zecevic, M.R. Stojic

121) W.W. Mullins, R.F. Sekerka, J. Appl. Phys. 34,323 (1963)

122) R.F. Sekerka, J. Appl. Phys. 36,264 (1965)

123) S.R. Coriell, S.C. Hardy, J. Appl. Phys. 40,1652 (1969)

124) N. Ibl, Surf. Tech. 10,81 (1980)

125) H.Y. Cheh, J. Electrochem. Soc., 118,551 (1971)

126) A.M. Pesco, H.Y. Cheh, J. Electrochem. Soc. 131,2259 (1984)

127) K. Viswanathan, M.A. Farell Epstein, H.Y. Cheh, J. Electrochem. Soc., 125,1772 (1978)

128) I. Markov, A. Boynov, S.Toschev, Electrochimica Acta, 18,337 (1973)

129) I. Markov, Thin Solid Films, 35,11 (1976)

130) I. Markov, E. Stoycheva, Thin Solid Films, 35,21 (1976)

131) Y. Ogota, K. Yamakawa, S. Yoshizawa, J. Appl. Electrochem. 13,611 (1983)

132) R.C. Alkire, D.B. Reiser, J. Electrochem. Soc. 131,2795 (1984)

133) M. Eisenberg, C.W. Tobias, C.R. Wilke, J. Electrochem. Soc. 101,306 (1954)

134) D.R. Gabe, J. Appl. Electrochem. 4,91 (1974)

135) D.R. Gabe, K.C. Walsh, J. Appl. Electrochem. 14,555 (1984)

136) D.J. Robinson, D.R. Gabe, Trans. Inst. Met. Finish. 48,35 (1970)

137) D.J. Robinson, D.R. Gabe, Trans. Inst. Met. Finish. 49,17 (1971)

138) Y.Kawase, J.J. Ulbrecht, J. Appl. Electrochem. 13,289 (1983)

139) J. Legrand, P. Dumarge, F. Coeuret, Electrochim. Acta 25,669 (1980)

140) F. Coeuret, J. Legrand, J. Appl. Electrochem. 10, 785 (1980)

141) F. Coeuret, J. Legrand, Electrochim. Acta 28,611 (1983)

142) R. Kappesser, I. Cornet, R. Grief, J. Electrochem. Soc. 118,1957 (1971)

143) A.C. Makrides, N. Hackerman, J. Electrochem. Soc. 105,156 (1958)

144) D.R. Gabe, F.C. Walsh, J. Appl. Electrochem. 14,555 (1984)

145) D.R. Gabe, F.C. Walsh, J. Appl. Electrochem. 14,565 (1984)

146) D.R. Gabe, P.A. Makanjuola, J. Appl. Electrochem. 17,370 (1987)

147) Ravoo, Ingenieur, 83,11 (1971)

148) N. Ibl, Schadegg, J. Electrochem. Soc. 114,54 (1967)

149) V.A. Ettel, V.B. Tilak, A.S. Gendron, J. Electrochem. Soc. 121,867 (1974)

150) Selman, J. Electroanalytical Chem., 65, 67 (1975)

151) D.C. Price, W.G. Davenport, Metallurgical Transactions 12B, 639 (1981)

152) J.R. Selman, Ph.D. Thesis, Dept. of Chemical Engineering, University of California, Berkeley, Lawrence Radiation Laboratory, UCRL-20557, (1971)

153) P.K. Andersen, Ph.D. Thesis, Dept. of Chemical Engineering,University of California, Berkeley, (1987)

154) R. Walker, R.C. Benn, Plating, 58,476 (1971)

155) R. Sard, R. Weil, Plating, 56, 157 (1969)

156) V.A. Lamb, D.R. Valentine, Plating, 53, 86 (1966); 52, 1289 (1965)

157) V.A. Lamb, D.R. Valentine, J. Electrochem. Soc., 117, 291c (1970); 117, 341c (1970); 117 381c (1970)

158) R.D. Young, E.C. Teague, "The Measurement and Charaterization of Surface Finish", in "Properties of Electrodeposits: Their Measurement and Significance", R. Sard, H. Leidheiser, F. Ogburn, Electrochemical Society Inc., Pronceton NJ, 1975.

159) D.J. Tidke, N. Ramaswamy, J. Appl. Electrochem., 14,83 (1984)

160) G. Rasigni, F. Vanier, M. Raigni, J.P. Palmari, A. Llebaria, J. Opt. Soc. Am., 73,1235 (1983)

161) S. Paramanand, P. Ramakrishnan, The International Journal of Powder Metallurgy and Powder Technology, 21,111 (1985)

162) J. Newman, "Electrochemical Systems", Prentice Hall, Englewood Cliffs NJ, 1973, pp. 340-352.

163) Francis B. Hidebrand, "Advanced Calculus for Applications", 2nd ed., p. 499, Prentice-Hall, Englewood Cliffs NJ, (1976)

164) Brice Carnahan, H.A. Luther, James O. Wilkes, "Applied Numerical Methods", John Wiley and Sons, New York, 1969. a) p. 92. b) p. 272

LAWRENCE BERKELEY LABORATORY
TECHNICAL INFORMATION DEPARTMENT
UNIVERSITY OF CALIFORNIA
BERKELEY, CALIFORNIA 94720